

Portland State University

PDXScholar

---

Dissertations and Theses

Dissertations and Theses

---

7-2-2008

# A Novel Approach to the Synthesis of Silicon Nanowires

Joo Chick Chan

Portland State University

Follow this and additional works at: [https://pdxscholar.library.pdx.edu/open\\_access\\_etds](https://pdxscholar.library.pdx.edu/open_access_etds)

 Part of the [Chemistry Commons](#)

Let us know how access to this document benefits you.

---

## Recommended Citation

Chan, Joo Chick, "A Novel Approach to the Synthesis of Silicon Nanowires" (2008). *Dissertations and Theses*. Paper 5956.

<https://doi.org/10.15760/etd.7826>

This Dissertation is brought to you for free and open access. It has been accepted for inclusion in Dissertations and Theses by an authorized administrator of PDXScholar. Please contact us if we can make this document more accessible: [pdxscholar@pdx.edu](mailto:pdxscholar@pdx.edu).

A NOVEL APPROACH TO THE SYNTHESIS OF SILICON NANOWIRES

by

JOO CHICK CHAN

A dissertation, submitted in partial fulfillment of the  
requirements for the degree of

DOCTOR OF PHILOSOPHY  
in  
CHEMISTRY

Portland State University  
©2008

## DISSERTATION APPROVAL

The abstract and dissertation of Joo Chick Chan for the Doctor of Philosophy in Chemistry were presented July 2, 2008, and accepted by the dissertation committee and the doctoral program.

### COMMITTEE APPROVALS:

  
Shankar B. Rananavare, Chair

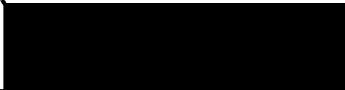
  
Carl C. Wamser

  
Albert S. Benight

  
Andres La Rosa

  
Erik Sanchez  
Representative of the Office of Graduate Studies

### DOCTORAL PROGRAM APPROVAL:

  
Kevin A. Reynolds, Chair  
Department of Chemistry

## ABSTRACT

An abstract of the dissertation of Joo Chick Chan for the Doctor of Philosophy in Chemistry presented July 2, 2008.

Title: A novel approach to the synthesis of silicon nanowires

Contemporary VLS-SiNW synthetic methods employ CVD and laser ablation methods that produce single crystalline SiNW; which can be doped by co-flowing appropriate dopants, such as diborane (p-type) and phosphine (n-type). Not only are these gases toxic (non-green), but also the synthetic methods used are costly requiring elaborate instrumental assembly. This thesis presents a low-cost and “green” method in synthesizing and doping of SiNW in a glass tube. It was found that by selecting the appropriate metal catalyst, precursor reactants, and the reaction conditions both SiNW and carbon nanotube (CNT) can be synthesized on metallic (aluminum and copper), semiconducting (silicon) and insulating substrates (borosilicate and fiber glass). By choosing an appropriate NW growth catalyst (antimony and aluminum) or dopant-containing organic compounds soluble in the silicon precursor (diphenylsilane) SiNW can be readily doped. During these studies, formation of metallurgical junctions between nanowires was observed due to surface adhering growth of SiNWs. Such

junctions are useful for next generation of nanoarchitecture based on grid structure as advocated by Likharev<sup>94</sup>. The methods developed here can address some of the major issues in integrating SiNWs in nanoelectronics related to reducing their contact resistance, improved doping and crafting metallurgical junctions.

To my beloved Dad and Mom  
For your support and encouragement

## **Acknowledgments**

I would like to express my gratitude to Dr. Shankar B. Rananavare, my thesis adviser, for the motivation. This thesis would not have been possible without his guidance and support.

I would like to thank my research group colleagues, Allen Chaparadza, Nabil Mistkawi, James Pattison, Hoang Tran and Beth Manhant, for their support and help in preparation for the seminars and presentations. Additional thanks to James Pattison for his work on iron nanoparticles synthesis.

Special thank to Monica Wright (Chemistry, PSU) for her time and effort in revising this manuscript and Timothy Gutu (Physics, PSU) for collecting the HR TEM images.

Finally, I would like to acknowledge Dr. John Freeouf (Physics, PSU), Dr. ChongMin Wang (PNNL, WA) and Dr. Bruce Arey (PNNL, WA) for the usage of the Zeiss optical microscopy, TEM and SEM, respectively.

## **Table of Contents**

Acknowledgments .....	ii
List of Figures .....	viii
List of Tables .....	xii

## **Chapter 1. Introduction**

<b>1.1. Silicon nanowires electronics .....</b>	<b>1</b>
<b>1.1.1. Contact Resistance .....</b>	<b>4</b>
<b>1.1.2. Doping in SiNWs .....</b>	<b>7</b>
<b>1.1.3. Assembly techniques .....</b>	<b>8</b>
<b>1.2. Overview of synthesis and characterization of SiNWs.....</b>	<b>10</b>
<b>1.2.1. Synthetic methods .....</b>	<b>10</b>
<b>1.2.2. Direct versus indirect bandgap in silicon .....</b>	<b>13</b>
<b>1.3. Outline .....</b>	<b>15</b>
<b>1.4. Instrumentation .....</b>	<b>15</b>
<b>1.4.1. Atomic force microscopy (AFM) .....</b>	<b>15</b>
<b>1.4.2. Scanning electron microscopy (SEM) .....</b>	<b>16</b>
<b>1.4.3. Transmission electron microscopy (TEM) .....</b>	<b>16</b>
<b>1.4.4. Differential scanning calorimetry (DSC) .....</b>	<b>16</b>
<b>1.4.5. Fluorometry .....</b>	<b>16</b>

## **Chapter 2. Supercritical condition synthesis of nanowires using VLS**

### **mechanism**

<b>2.1. Introduction .....</b>	<b>18</b>
--------------------------------	-----------



<b>2.2.</b>	<b>Synthesis of bulk SiNWs using supercritical VLS method .....</b>	<b>18</b>
2.2.1.	Sample preparation .....	19
2.2.2.	Procedure .....	20
2.2.2.1.	Deoxygenation of solvent and Ti reactor .....	20
2.2.2.2.	Leak and pressure test .....	21
2.2.2.3.	Synthesis of bulk SiNW using supercritical VLS method .....	22
2.2.3.	Observations .....	23
 <b>Chapter 3. Rapid synthesis of nanowires using VLS mechanism in enclosed glass vessel</b>		
<b>3.1.</b>	<b>Procedure .....</b>	<b>26</b>
3.1.1.	Deposition of gold catalyst .....	26
3.1.2.	Synthesis of silicon nanowires .....	26
<b>3.2.</b>	<b>Results .....</b>	<b>28</b>
<b>3.3.</b>	<b>Time of reaction, temperature, concentration and pressure dependent studies on the effect of SiNWs synthesis .....</b>	<b>30</b>
3.3.1.	Effect of diphenylsilane to Au ratio on synthesis of SiNWs .....	30
3.3.1.1.	Procedure .....	30
3.3.1.2.	Results .....	31
3.3.2.	Effect of reaction time on synthesis of SiNWs .....	32
3.3.2.1.	Procedure .....	32
3.3.2.2.	Results .....	32
3.3.3.	Duo chamber tube .....	33

3.3.4.	Effect of diol-Au <sup>0</sup> catalyst surface deposition on the synthesis of SiNWs .....	35
3.3.4.1.	Procedure .....	36
3.3.4.2	Results .....	37
3.3.5.	Effect of reaction temperature on synthesis of SiNWs .....	38
3.3.5.1.	Procedure .....	38
3.3.5.2	Results .....	39
3.3.5.3.	Discussion .....	41
A.	Rate of reaction .....	41
A1.	Model 1. Spontaneous decomposition of DPS .....	42
A2.	Model 2. Steady decomposition of DPS .....	43
B.	Model for diameter of Silicon nanowires grown through VLS mechanism .....	48
C.	Mass flow and wetting considerations during the growth of nanowires .....	51
3.4.	Summary of SiNWs diameter from optimization experiments .....	55
3.5.	Synthesis of silicon nanowires on different substrates .....	56
3.5.1.	On silicate glass, aluminized-silicon and copper substrate .....	56
3.5.2.	Results .....	56
3.5.2.1.	SiNWs on Cu .....	56
3.5.2.2.	SiNWs on silicate glass .....	57
3.5.2.3.	SiNWs on aluminium .....	58

3.5.3.	Summary of SiNWs diameter synthesized on different substrates .....	59
3.6.	Bulk synthesis of SiNWs .....	60
3.6.1.	Aluminized silicon template .....	60
3.6.2.	Glass fiber template .....	61
3.6.2.1.	Results .....	62
3.6.3.	Aluminium oxide (alumina) template .....	63
3.6.3.1.	Results .....	64
3.6.4.	Calcium carbonate template .....	65
3.6.5.	Summary of SiNWs diameter on different templates .....	66
3.7.	Synthesis of SiNWs using aluminium as catalyst via closed CVD technique in glass vessel .....	67
3.7.1.	Procedure .....	70
3.7.1.1.	Aluminium as catalyst .....	70
3.7.1.2.	Antimony as catalyst .....	70
3.7.2.	Results .....	71
3.8.	Doping of SiNWs using organometallic precursors .....	72
3.8.1.	Procedure .....	73
3.8.1.1.	Synthesis of p-type SiNW .....	73
3.8.1.2.	Synthesis of n-type SiNW .....	74
3.8.2.	Results .....	74
3.8.3.	Discussion .....	77

<b>3.9.</b>	<b>SiNW junctions .....</b>	<b>79</b>
<b>3.10.</b>	<b>Fluorescence spectroscopy analysis .....</b>	<b>81</b>
<b>3.10.1.</b>	<b>Results .....</b>	<b>82</b>
<b>Chapter 4. Future work</b>		
<b>4.1.</b>	<b>Characterization of dopants in SiNWs and junctions of SiNWs .....</b>	<b>91</b>
<b>4.2.</b>	<b>Synthesis of multiwall carbon nanotubes via glass tube method .....</b>	<b>91</b>
<b>4.3.</b>	<b>Challenges and limitation .....</b>	<b>93</b>
<b>4.4.</b>	<b>Grid assembly of silicon nanowires .....</b>	<b>95</b>
	<b>References .....</b>	<b>97</b>
	<b>Appendix A. Chemical reagents .....</b>	<b>104</b>
	<b>Appendix B. Synthesis and characterization of gold and iron nanoparticles by</b>	
	<b>templating with bolamphiphiles .....</b>	<b>105</b>
	<b>Appendix C. DSC studies of thermal properties of reactant used in SiNW</b>	
	<b>synthesis .....</b>	<b>122</b>
	<b>Appendix D. Construction of supercritical flow reactor system .....</b>	<b>127</b>
	<b>Appendix E. Calibration of furnaces .....</b>	<b>130</b>
	<b>Appendix F. TEM HR lattice plane imaging, selected area diffraction</b>	
	<b>pattern and lattice plane analysis .....</b>	<b>134</b>
	<b>Appendix G. Fluorescence spectroscopy of undoped SiNW, doped SiNW</b>	
	<b>and Si sphere .....</b>	<b>142</b>

## List of Figures

Figure 1. Electron transport through a gate channel .....	6
Figure 2. a) Binary Phase Diagram of Au-Si and b) The VLS mechanism .....	11
Figure 3. Binary phase diagram of Fe-Si .....	12
Figure 4. The energy band diagrams .....	14
Figure 5. A supercritical high temperature and pressure flow reactor system .....	19
Figure 6. Three-neck round-bottom flasks for freeze/thaw vacuum deoxygenation of solvent .....	20
Figure 7. Pressure test of the reactor system with cyclohexane .....	23
Figure 8. Optical images of extracted residual from the Ti reactor after multiple reaction runs .....	24
Figure 9. Illustration of vacuum system for freeze/thaw deoxygenation of glass reaction vessel .....	27
Figure 10. Si nanowires synthesized on silicon substrate in a glass vessel .....	28
Figure 11. SEM image of SiNWs synthesized on silicon substrate .....	28
Figure 12. Optical excitation and emission of Si nanowires on silicon and copper substrates .....	29
Figure 13. SiNWs synthesized with 8.0 $\mu\text{mol}$ s and 16.0 $\mu\text{mol}$ s of DPS .....	31
Figure 14. SEM images of SiNWs synthesized on Si substrate with reaction times of 3 min 20 sec and 7 min 10 sec .....	32
Figure 15. Wire growth direction switching to other $\{111\}$ directions .....	33
Figure 16. Duo chamber glass reaction tube .....	34

Figure 17. Low resolution SEM image of an edge of the catalyst droplet used to synthesize SiNWs .....	35
Figure 18. N <sub>2</sub> pressure spray gun for deposition of catalyst solution .....	36
Figure 19. SEM images of SiNWs synthesized from spray deposition of gold ....	37
Figure 20. TEM image of SiNW synthesized at 500 °C for 1hr .....	38
Figure 21. SEM images of SiNWs synthesized at different temperature .....	40
Figure 22. A model plot of ratio $R_1/R_2$ as a function of temperature .....	45
Figure 23. SEM images of SiNWs synthesized with triphenylsilane at different temperature .....	47
Figure 24. Plot of SiNWs mean diameter with respect to number of moles of DPS .....	50
Figure 25. SEM images of Si nanowires grown on copper substrate .....	56
Figure 26. Low resolution TEM images of Si nanowires grown on copper TEM grid .....	57
Figure 27. SEM images of Si nanowires grown on silicate glass substrate .....	57
Figure 28. SEM images of Si nanowires grown on aluminized substrate .....	58
Figure 29. TEM images of Si nanowires grown on aluminized substrate .....	58
Figure 30. Average diameter of SiNWs on different substrates .....	59
Figure 31. SEM images of partially etched aluminium layer exposing the Underlying oxide .....	61
Figure 32. SEM images of Si nanowires grown on glass fiber substrate .....	62
Figure 33. Plot of etch rate (grams of silicate/sec) versus concentration of	

NH <sub>4</sub> F.HF in H <sub>2</sub> O .....	63
Figure 34. SEM images of SiNWs synthesized on Al <sub>2</sub> O <sub>3</sub> powder .....	64
Figure 35. SEM images of SiNWs on CaCO <sub>3</sub> .....	65
Figure 36. SiNWs diameter synthesized on different templating materials prior to etching .....	66
Figure 37. Binary phase diagram of Ti and Si .....	68
Figure 38. Binary phase diagram of Al-rich region of Al and Si .....	69
Figure 39. SEM images of SiNWs synthesized using Al as catalyst .....	71
Figure 40. TEM images of SiNWs synthesized using Al as catalyst .....	71
Figure 41. SEM images of SiNWs synthesized using Sb as catalyst .....	72
Figure 42. SEM images of boron-doped SiNWs .....	75
Figure 43. HRTEM image and corresponding diffraction pattern of boron- doped SiNW .....	76
Figure 44. SEM image of antimony-doped SiNWs .....	76
Figure 45. SEM image of phosphorus-doped SiNWs .....	77
Figure 46. SEM images of cross junction structure observed with undoped and boron-doped SiNWs .....	79
Figure 47. TEM image of an epitaxial SiNW junction .....	80
Figure 48. TEM image of a non-epitaxial SiNW junction .....	81
Figure 49. UV Photo-illumination of Si nanowires grown on copper, silicon and silicate glass .....	83
Figure 50. Fluorescence spectra of Si sphere on Si substrate (without Au	

catalyst) .....	84
Figure 51. Fluorescence spectra of Si sphere on Si substrate (with Au	
catalyst) .....	84
Figure 52. Fluorescence spectra of Au catalyzed SiNW on Si substrate .....	85
Figure 53. Fluorescence spectra of Al catalyzed SiNWs .....	85
Figure 54. Band energy diagram silicon .....	86
Figure 55. Boxplot of emission energy of undoped SiNWs, doped SiNWs and	
Si spheres, at an excitation wavelength of 250 nm .....	87
Figure 56. SEM images of CNTs synthesis at different temperature .....	92
Figure 57. SEM images of curly carbon rods catalyzed from Ni .....	93
Figure 58. SEM images of carbon particles observed using hexadecane and	
anthracene as carbon precursor .....	94
Figure 59. Cross array directional control growth of SiNWs .....	96



## List of Tables

Table 1. Barrier heights of metal-semiconductors .....	6
Table 2. Comparison of Si NW/Sphere synthesized using TPS versus DPS .....	48
Table 3. SiNWs diameter with respect to number of moles of DPS .....	50
Table 4. Internal pressure of glass tube assuming complete decomposition of the DPS .....	52
Table 5. SiNWs diameter from optimization experiments .....	55
Table 6. Summary of SiNWs diameter synthesized on different substrates .....	59
Table 7. Concentration dependent of etch rate of $\text{NH}_4\text{F.HF}$ on fiber glass .....	62
Table 8. SiNWs diameter synthesized on different templating materials prior to etching .....	66
Table 9. Diameter of doped SiNWs .....	78
Table 10. Summary of emission peaks of undoped SiNW, doped SiNW and Si sphere from fluorescence spectroscopy .....	89

## **Chapter 1. Introduction**

### **1.1. Silicon nanowires electronics**

The use of nanomaterials dates back to early history when the Chinese reportedly used gold nanoparticles to introduce the red color into porcelain, but scientists did not begin to explore the physical characteristics of Au nanoparticles until the middle of the 19<sup>th</sup> century. The stability of Au colloid dispersions was first reported by Faraday<sup>1</sup> in 1857. Technological limitations in the 19<sup>th</sup> century prevented physical visualization of nanomaterials because nanoscale dimensions exist beyond the resolution of the human eye or optical microscope. However, developments in modern technology have provided methods to image and manipulate nanoparticles which led to a bloom in research on micro and nano materials. The invention of scanning tunneling microscopy (STM) in the early 1980s<sup>2</sup> followed by the subsequent development of scanning probe microscopy (SPM), the atomic force microscopy (AFM)<sup>3</sup> a high resolution STM successor, and various electron microscopy metrology techniques such as transmission electron microscopy (TEM) and scanning electron microscopy (SEM), have allowed scientists to probe and characterize many materials at micro and nano levels.

The closing of the 20<sup>th</sup> century ushered in nanotechnology which exploits unique physical and chemical properties of nanomaterials. One of the current heated topics in technology lies on the ever shrinking devices dimension of semiconductor devices. The invention of the first transistor at AT&T Bell Lab in 1947 with centimeter scale has given birth to the latter day high speed microprocessor and a host

of microelectronic devices. The transistor remains at the frontier of research in the modern semiconductor industry. Breakthroughs in silicon processing technologies and science have led the second industrial revolution that has ushered in the modern web-age of mp3 music players, cell phones, and laptop computers. The demand for these devices has spearheaded giant gains in productivity and globalization. Today complementary metal oxide semiconductor (CMOS) transistors have already reached 30 nm channel length which, is only an order of magnitude larger than the size of typical molecules and comparable to the size of self-assembled molecular aggregates such as DNA and mitochondria found in biological systems.

At these nano scale lengths, the laws of macroscopic physics, controlling the electronic properties of large-scale devices, give away to mesoscopic physics. In this size regime where particles can interact in a quantum-mechanically correlated fashion, two of the greatest limitations are apparent in transistor design due to material limitations and device physics<sup>4</sup>. Firstly, the off-currents in MOSFET increases hence their power dissipation increases with reduction in transistor gate length. Secondly, continuous shrinkage in dimension of transistors faces fundamental changes in the materials properties for example, widening of band gap of semiconductors that occurs on the length scale of de Broglie's wavelength<sup>5</sup>.

Both the conventional top-down and bottom-up methods allow fabrication of transistors. However, both methods have their disadvantages. Nanostructure created by lithography, a top-down method, has a tendency of leaving impurities and causing crystallographic damage to material<sup>6</sup> that results in large leakage current. For bottom-

up or self assembly methods, coulomb blockades at electrical contacts are a major problem that can result in device over-heating. The blockade is thought to be caused by electrons tunneling through junctions leading to quantum resistance ( $26\text{ k}\Omega$ ) at the junction<sup>7</sup>. The large built-up potential prevents another electron from tunneling until the charge built-up on the junction is released to the environment. This and other models and mechanism of self-heating<sup>8</sup> or overheating<sup>9</sup> caused by coulomb blockade have also been reported.

High device density and leakage currents result in device overheating as well. Since it is not practical to operate devices at nuclear reactor temperatures, a revolutionary change must take place in the design and fabrication of the next generation of electronic – nanoelectronic devices. The two premier materials that have received intense research activity are carbon nanotubes and silicon nanowires (SiNWs) due to their ability to conduct with little or no resistance.

Single walled  $1.5\text{ nm}$  diameter carbon nanotubes can conduct as much as  $10\text{ }\mu\text{A/nm}^2$  at room temperature, and exhibit a 1-D Luttinger liquid-type behavior implying phase-coherent electron transport. Because of their extraordinary thermal and chemical stability, carbon nanotubes are compatible with the current device processing environments. Researchers<sup>10,11,12</sup> have already demonstrated many superior characteristics of carbon nanotube field effect transistors. Unfortunately, current synthetic methods for nanotubes lead to a wide dispersion in tube size and in their chirality leading to band-gap variation from tube to tube. Unless new methods emerge

for synthesis or separation, the fate of nanotube transistors in nanoelectronic devices will remain uncertain.

Research on silicon nanowires has revealed the ease of doping (n-p type), their coherent electron transport<sup>13</sup>, high mobility, and small-scale device integration<sup>14</sup>. Unlike carbon nanotubes, they have a fixed band gap (for  $d > 5$  nm). Single crystalline nanowires with well-defined growth directions can be grown epitaxially on a silicon surface<sup>15,16</sup>. During their growth, a vapor-liquid-solid (VLS) mechanism prevails that allows control over the diameter and the length of nanowires<sup>17</sup>. Fabrication of nanowire transistors with potential silicon nanowires using a bottom-up method can eliminate crystallographic damage by lithography and acid etching. With high charge mobility, power dissipation and overheating can be minimized. Silicon nanowires are thus a candidate for alternative method in fabrication of semiconductor transistors.

Before SiNWs are to be incorporated into transistor technology, several major issues need to be addressed, they are: contact resistance, doping and controlled alignment of SiNWs as discussed below.

#### **1.1.1. Contact Resistance.**

The issue of contact resistance becomes significant for SiNWs simply because the real contact area becomes smaller as compared to macroscopic contact. A large contact resistance generally impedes electron flows in realistic devices. For example, in modern 50 nm processors, the vias that contact the silicon transistors are approximately  $100 \times 100 \text{ nm}^2$  (or  $10^{-10} \text{ cm}^2$ ). For a material with  $l \cdot \rho \approx 10^{-6} \text{ ohm-cm}^2$ , translates to an equivalent of a 10 kohms resistor for electron flowing from metal into

semiconductor and another 10 kohm equivalent resistor for flowing out. A low contact resistance requires  $l\rho \approx 10^{-7}$  ohm-cm<sup>2</sup> or lower to prevent resistive overheating of devices.

When the metal makes contact with the semiconductor or insulator (MOS) a potential barrier between the junctions prevents majority of charge carrier to flow across the two materials. Only a small portion of charge carriers have sufficient kinetic energy to overcome the barrier and pass into the other material. Two possible types of contact between metal-semiconductor junctions are Schottky and ohmic contacts. When voltage bias is applied across the junction, the barrier thickness can be reduced due to interfacial band bending on the semiconductor side, but not the metal side. As a result tunneling through the barrier is facilitated. This imparts a rectifying characteristic for conduction through the junction known as the Schottky barrier or rectifying contact. Schottky contacts are generally ideal for making diodes. However, for electrical transport through semiconductor devices an ohmic contact is needed for both bias (positive and negative) polarities. In order to have a good ohmic contact, a material with low barrier height or matching Fermi levels is needed. Many good ohmic contacts have been achieved by annealing the metal and semiconductor point of contact to inset<sup>18</sup> or form an alloy that lowers the energy barrier. The calculated<sup>19</sup> barrier heights of various metal-semiconductors are tabulated in Table 1.

Semiconductor	n-Silicon	p-Silicon	n-GaAs	p-GaAs	n-Ge	p-Ge	n-InP	p-InP
Metal								
Aluminium	0.20	0.92	0.18	1.24	1.07	-0.409	-0.2	1.54
Gold	0.25	0.87	0.23	1.19	1.12	-0.459	-0.15	1.49
Copper	0.35	0.77	0.33	1.09	1.22	-0.559	-0.05	1.39
Silver	0.25	0.87	0.23	1.19	1.12	-0.459	-0.15	1.49
Platinum	1.27	-0.15	1.25	0.17	2.14	-1.479	0.87	0.47
Tungsten	0.45	0.67	0.43	0.99	1.32	-0.659	0.05	1.29
Polysilicon								
(n-doped; $10^{15}/\text{cm}^3$ )	0.26	0.86	0.24	1.18	1.13	-0.47	-0.14	1.48
(p-doped; $10^{15}/\text{cm}^3$ )	0.86	0.26	0.84	0.58	1.73	-1.07	0.46	0.88

Table 1. Barrier heights of metal-semiconductors.

In addition to the above classical/semiclassical considerations, there exists additional contact resistance, so called quantum resistance when an electron from a 3-D/2-D is moved in 1-D contact. In 1957 while working at IBM, Landauer<sup>20,5</sup>, examined the fundamental limit on conductance. This limit can be considered with a simplified picture of electron transport through a 1 dimensional channel connected by two 3-D electron reservoirs at chemical potential  $\mu_1$  and  $\mu_2$ ,

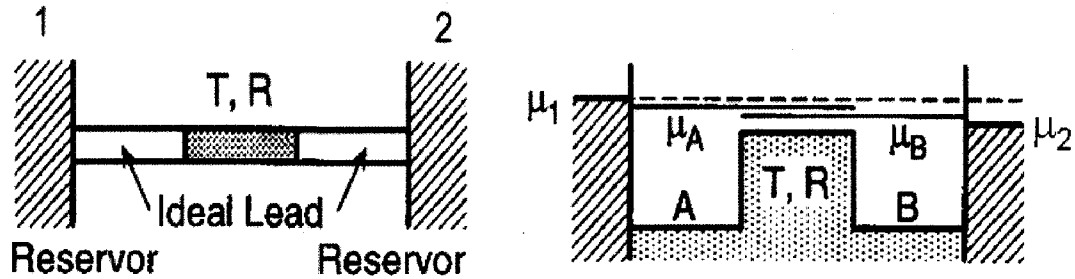


Figure 1. Electron transport through a gate channel

The Fermi velocity and density of states of the electron are denoted by  $v$  and  $dn/dE$  respectively. The current flows from 1-2:

$$I = e.v.\frac{\partial n}{\partial E}T(\mu_1 - \mu_2) \quad (1.1)$$

Where  $T$  is the transmission probability. Using the solution to the particle in a box it can be shown that:

$$\frac{\partial n}{\partial E} = \frac{l}{2h\nu} \quad (1.2)$$

Since the difference in chemical potentials  $\Delta\mu$  can be related to the applied electrical potential difference, i.e.,

$$\Delta\mu = eV \quad (1.3)$$

Thus the basic conductance of a single electron device is:

$$G = \frac{2e^2}{h} \approx (12k\Omega)^{-1} \quad (1.4)$$

This phenomenon becomes more significant at the nanoscale because the contact areas are small. For bulk contacts the quantum effects are insignificant due to the combination of parallel resistors.

Contacts between metal-insulator are generally Schottky contacts. The barrier height for an Al gate and Ag gate on a thin film of SiO<sub>2</sub> are 3.25 eV and 4.25 eV, respectively, and independent on thickness of SiO<sub>2</sub> film<sup>21</sup>. Synthesis of SiNWs on different substrates, insulator, semiconductor and metal, can allow for a more direct contact quantification.

### 1.1.2. Doping in SiNWs.

Doping of bulk semiconductor substrate via diffusion or ion implantation are well established processes. Slight fluctuation in dopant level is easily tolerated in macroscale. However, successful doping on a nanoscale requires overcoming several challenges. Fluctuation in the distribution of dopant atoms in SiNW has very low tolerance because it can result in a totally different functionality in a device. For



example, with a dopant concentration of  $10^{18}/\text{cm}^3$ , there would be one dopant atom in every  $10 \times 10 \times 10 \text{ nm}^3$  volume in a device. Control of the location of dopant atoms is another challenge at the nanoscale. SiNWs have a higher surface area to volume ratio, therefore, dopant atoms can have potential preference on the surface rather than in center of the SiNW. Dopant atoms on the surface will result in different functionality than in the center.

Various post-growth and simultaneous-growth doping methods and materials have been reported, i.e., vapor doping of SiNW with bismuth<sup>22</sup> by annealing in a furnace at  $1000^\circ\text{C}$ ; thermal diffusion doping of ZnTe NW with copper<sup>23</sup> by annealing at  $400^\circ\text{C}$ ; boron-doped and phosphorus-doped<sup>24</sup> SiNW via laser ablation; etc. Additionally, the study of p-doped silicon nanowires using ultra-high vacuum (UHV) STM (room temperature) has been reported<sup>25</sup>. Rectangular and uniformly distributed domains on the silicon nanowires of several nanometers in size were observed under UHV STM which was suspected to be associated with the p-type dopant. UHV STM analysis will be an appropriate method for monitoring the uniformity of distribution of the dopant in the silicon nanowire.

### **1.1.3. *Assembly techniques.***

Due to the nanoscale of SiNWs physical means of assembly or fabrication are not practical. Ingenious methods of SiNWs assembly and device fabrication have been invented that involve either directed or assisted SiNWs growth or assembly. Two popular fabrication methods are post synthesis nanowire assembly and orientation control of nanowires.

Electrically directed assembly or dielectrophoresis has been used to manipulate a variety of nanoscale materials such as SiNWs<sup>26</sup>, nickel silicide NWs<sup>27</sup> etc. Dielectrophoretic forces rely on the high electrical field across two small radius of curvature electrode assemblies separated by an extremely narrow gap ( $\sim 3\text{-}5\text{ }\mu\text{m}$ ) by applying an ac voltage. The nanowires, suspended in a fluidic medium, align or orient across the electrodes gap as a result of the electrophoretic force.

Hierarchical assemblies of SiNWs have been developed by Lieber et. al.<sup>28</sup> by flowing a solution of suspended SiNWs across a Poly(dimethoxysiloxane) (PDMS) flow cell consisting of multi-arrays of directional specific fluidic channels (channels widths ranging from 50 to 500  $\mu\text{m}$  and lengths from 6 to 20 mm). Parallel and cross arrays of SiNWs were achieved. Nanoscale electronics components such as p-n diodes formed from p-type and n-type SiNWs<sup>29,30</sup> and high performance SiNW FET<sup>31,32</sup> were fabricated using the fluidic channel method.

Another hierarchical SiNWs assembly approach was also developed by Lieber et. al.<sup>33,34</sup> that was implemented using a Langmuir-Blodgett trough to organize nanowires in a unidirectional alignment and laying them over photolithographically defined interconnects.

Orientation control growth techniques have been developed but have not yet received any wide-spread recognition. Homma et. al.<sup>35,36,37,38</sup> has developed an array step-band networks technique on Si substrate resulting in controlled alignment of island Au particles. Since SiNWs grow only where the Au particles are located, this method allows precise control of SiNWs location. However, the SiNWs synthesized

were perpendicular to the surface and the majority of NWs fabricated devices require NW's parallel to the surface.

Parallel and controlled growth of SiNWs has been developed by Sharma et. al.<sup>39,40,41,42</sup> demonstrating a single-crystal silicon nanowire bridges grown between two vertical silicon posts. A gold catalyst was angle-deposited on one side of the vertical wall of the silicon post. Upon carrying out the metal-catalyzed chemical vapor deposition<sup>43</sup> (CVD), a silicon nanowire bridge was observed between two Si posts spaced  $<12\mu\text{m}$  apart.

Surface parallel growth of SiNWs will be examined in this work and a model of the growth will be discussed.

## **1.2. Overview of synthesis and characterization of SiNWs**

### **1.2.1. Synthetic methods**

In 1964 the first single crystal whiskers (metal whiskers) were synthesized at Bell Telephone Laboratories by Wagner and Ellis<sup>44</sup> leading to many important present day techniques for synthesis of micron to nano scale metallic and semiconductor wires. The vapor-liquid-solid (VLS) mechanism proposed by Wagner and Ellis is included in two important techniques for synthesis of SiNWs, which, are CVD and laser ablation, both of which requires a catalyst.

Reaction temperature, reagent concentration, and an appropriate metal catalyst, reaction for synthesis of SiNWs can be determined by the binary phase diagram of the chosen metal-Si pair. Two popular metal catalysts frequently used are gold and iron.

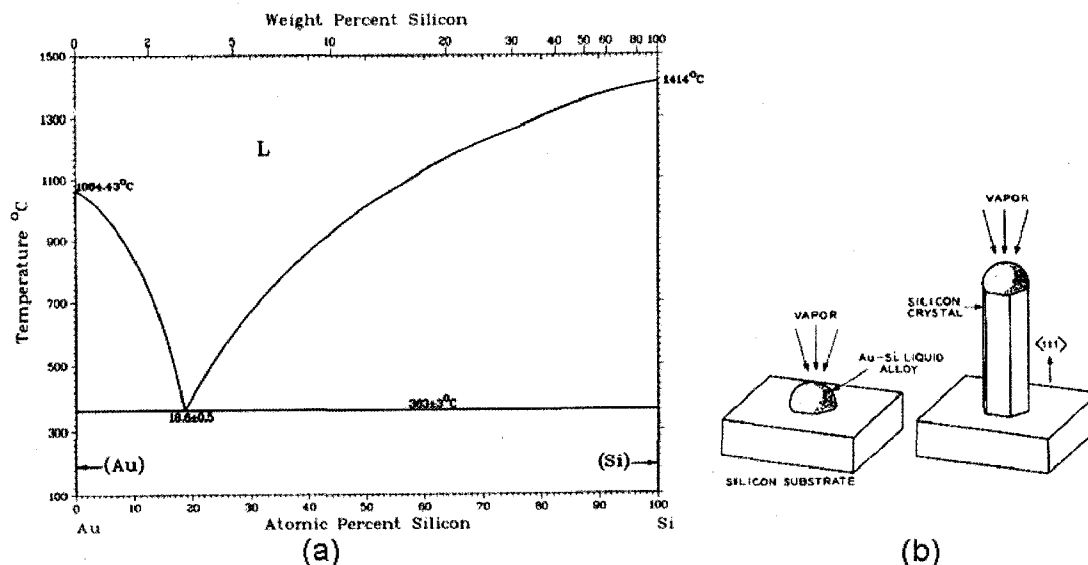


Figure 2. a) Binary Phase Diagram of Au-Si<sup>45</sup> and b) The VLS mechanism<sup>44</sup>.

The silicon and gold phase diagram in Figure 2a shows a eutectic point of 363 °C at 81.4% Au:18.6% Si by atomic percentage. This sets the minimum reaction temperature and concentration. When the liquid alloy supersaturates, additional Si atoms diffusing into the liquid alloy get extruded as a single crystal wire. As more and more diffusing Si atoms bond to the liquid/solid interface, a propagating crystalline wire is formed. This is the VLS mechanism proposed by Wagner and Ellis<sup>44</sup>.

In the CVD technique, Au nanoparticles are pre-deposited on to a Si substrate. The substrate is heated to 400-600 °C in a gas flow controlled chamber at a reduced pressure. A silane gas mixed with He is introduced into the system at a controlled flow rate. Silane gas decomposes upon contact with the heated substrate and synthesis of SiNWs via VLS mechanism take place.

In the laser ablation<sup>46</sup> technique, a laser is used to ablate a  $\text{Si}_{1-x}\text{Fe}_x$  target at a temperature  $>1200$  °C in an evacuated quartz oven. The ablated Si and Fe vapor undergoes VLS mechanism to produce SiNWs.

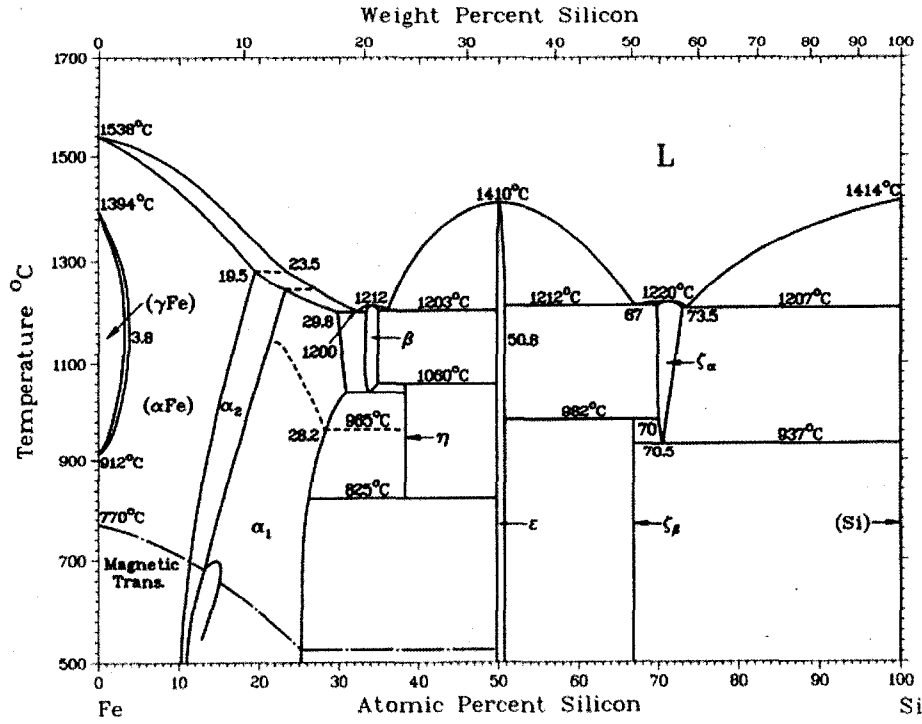


Figure 3. Binary phase diagram of Fe-Si<sup>47</sup>

Another synthetic technique, which does not require a catalyst, is oxide-assisted growth<sup>48</sup> (OAG) of SiNWs. This method does not follow the VLS mechanism. The resultant SiNWs are metal free. SiNWs are obtained from thermal evaporation (1130 to 1400 °C) of either a mixture of silicon dioxide and silicon powders or a pure silicon monoxide powder. During heating SiO<sub>2</sub> and Si mixture can generate SiO. By heating SiO, Si precipitation is observed.



It has been proposed that the vapor phase consists mainly of silicon suboxides, Si<sub>n</sub>O<sub>m</sub> (n,m=1-8) clusters, which have unique bonding preferences<sup>49</sup>. Silicon suboxides clusters prefer to form Si-Si bonds with other clusters, while oxygen-rich silicon oxide

clusters prefer to form Si-O bond with other clusters<sup>50</sup>. Initially silicon suboxide cluster nucleates on a cold finger Si substrate and subsequently grows by assimilating approaching clusters from the vapor. Oxygen in the silicon suboxide forms a sheath oxide on SiNWs. It has been speculated that the tip of the SiO has a high internal pressure due to its small radius of curvature, thus it remains a liquid and has high sticking probability for incoming clusters. 1-D propagation growth is more prominent.

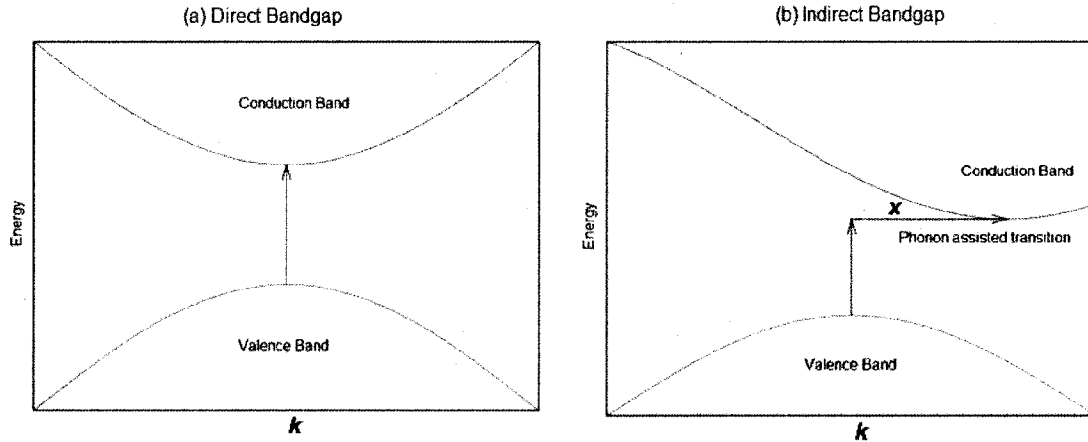
### **1.2.2. Direct versus indirect bandgap in silicon**

Semiconductor materials are classified by bandgap type as either direct or indirect. When the minimum of the conduction band lies directly above the maximum of the valence band in momentum space, this is known as a direct bandgap (Figure 4a). By determining the wavelength of the emitted radiation, when an electron from the conduction band recombines with the hole in the valence band, one can determine the bandgap energy. In Figure 4b the minimum of the conduction band is shifted by some k-vector in momentum space away from the valence band, this is known as an indirect bandgap. Here the direct recombination of an electron from the conduction with a hole in the valence band is generally not favorable. Materials such as GaAs and InP are reported to have a direct bandgap. Silicon, in general, has an indirect bandgap (1.1 eV) (see section 3.10.1, Figure 54). As the dimension of the crystalline Si decreases (<5 nm) the bandgap increases. It has been reported that at nano dimension Si becomes a direct bandgap<sup>51,52</sup> (~2 eV) due to quantum confinement.

Photoluminescence (PL) spectroscopy is used to measure the emission due to radiative recombination of electrons and hole from conduction and valence bands.

Indirect bandgap semiconductors exhibit very weak PL (Figure 4d), whereas direct bandgap semiconductors exhibit intense PL (Figure 4c). As the diameter of SiNWs encased in the porous silica matrix decrease, high intensity PL is observed from 2.5-4.5 eV<sup>53</sup> range.

### Optical Absorption



### Photoluminescence

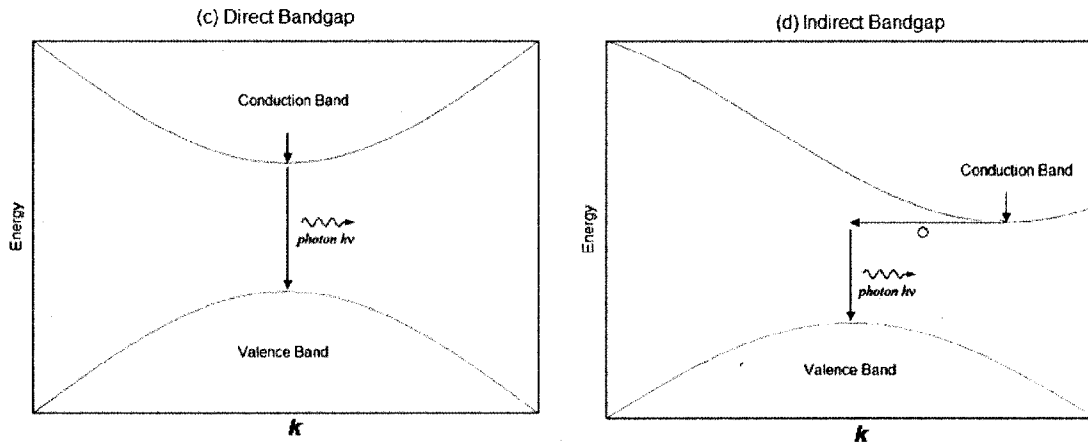


Figure 4. Energy Band Diagrams: Optical absorption (a,b) and photoluminescence (c,d) for direct bandgap (a,c) and indirect bandgap (b,d) semiconductors. [Plot (b) shows that optical absorption can occur with the assistance of either phonon or photon (X). For indirect bandgap (d), phonon emission is mandatory (o) for conservation of momentum]

### **1.3. Outline**

The purpose of this thesis is to further develop SiNW synthesis methods. Chapter 2 presents a supercritical high pressure and temperature synthesis of SiNWs. In chapter 3 a new SiNW synthetic method employing an enclosed glass tube is presented along with preliminary optimization of synthesis conditions. Bulk synthesis and doping of the SiNWs are also discussed. Finally, the last chapter outlines future work.

The preliminary results of the synthesis of the metal nanoparticle catalyst are presented in Appendix B. The differential scanning calorimetry (DSC) studies of melting and decomposition thermodynamics of the reagents are presented in Appendix C. The construction of the supercritical flow reactor system used in the initial attempt to synthesize SiNWs is presented in Appendix D. Calibration of all the furnaces used in the synthesis of SiNWs are presented in Appendix E. Additional microscopy (TEM) and spectroscopy (fluorescence) data are presented in Appendix F and G, respectively.

### **1.4. Instrumentation**

#### **1.4.1. Atomic force microscopy (AFM)**

The AFM (DI 3000) was used to perform 3-D analysis and characterization of the Au and Fe nanoparticles. The AFM was also set-up for magnetic force microscopy (MFM) imaging. A magnetized chromium coated silicon MFM tip (with resonant frequency between 50–100 kHz) was used. Imaging was carried out with “Tapping Mode” coupled with “Interleave mode”. The height and frequency modulation



detection of the iron particles with interleave mode (30 nm lift height) was obtained. The input feedback frequency was maintained at 73.3 kHz.

#### **1.4.2. Scanning electron microscopy (SEM)**

An FEI Siron XL30 model SEM was used for electron microscopy imaging. Imaging was performed at an accelerating voltage of 5 kV and beam current of ~300  $\mu$ A.

#### **1.4.3. Transmission electron microscopy (TEM)**

TEM was used for bright field, dark field, selected area diffraction, EDX analysis and high resolution lattice plane imaging. The TEM microscopes used were FEI Technai F-20 TEM (PSU electron microscopy center) and JEOL 2010 TEM (Pacific Northwest National Laboratory). Imaging was performed at an accelerating voltage of 200 kV. A column vacuum of less than 0.10  $\mu$ torr was achieved.

#### **1.4.4. Differential scanning calorimetry (DSC)**

The DSC unit consist of a low temperature cell (Mettler DSC 30) controlled by a TA processor (Mettler TC 10A). Data were collected via an 8-bit A/D card interface with LabView on a Window 98 PC. DSC was used method to determine the phase transition temperature and thermal decomposition temperature of the reagents.

#### **1.4.5. Fluorometry**

Fluorescence studies were performed on a PTI (Photon Technology International) fluorometer. The solution holder was swapped out with a solid substrate holder. The sample holder was adjusted to 70° normal from the incident beam. The slitwidth from the source to the sample to the detector were all set to equal width to

give the optimal signal. Slitwidth was set between 2-4 nm. A sample with SiNWs deposited was first scanned at different excitation wavelength, then at a fixed emission wavelength, to determine the optimal excitation wavelength.

## **Chapter 2. Supercritical condition synthesis of nanowires using VLS mechanism**

### **2.1. Introduction**

Kroger et al. have reported bulk synthesis of SiNWs in high-pressure super fluid reactors<sup>54</sup>. The synthesis made use of VLS mechanism in supercritical condition, which involved extremely high pressure (200-250 bar) and high temperature (450-500 °C). Supercritical conditions presumably increased the diffusivity of silicon atoms into gold droplets. The resultant wires had thin and narrow diameter distribution.

For this work, the initial approach for SiNWs synthesis used this supercritical fluid method in a high pressure and temperature flow reactor. The titanium (Grade 5) reactor used had a nominal capacity of 5 mL and was designed to handle pressure up to 6000 psi and temperature of 600 °C.

To better understand the reaction conditions, DSC was used to examine the thermal stability of the reagents, including the vaporization and decomposition temperatures of diphenylsilane (DPS); melting point of Au-Si alloy. The DSC studies are presented in Appendix C.

### **2.2. Synthesis of bulk SiNWs using supercritical VLS method**

The supercritical flow reactor system is illustrated in Figure 5. Details of construction for the supercritical system are presented in Appendix D.

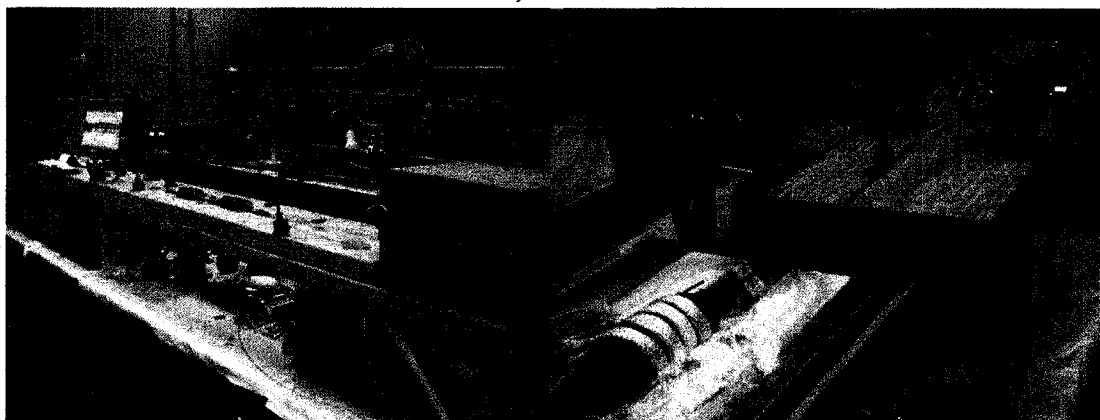
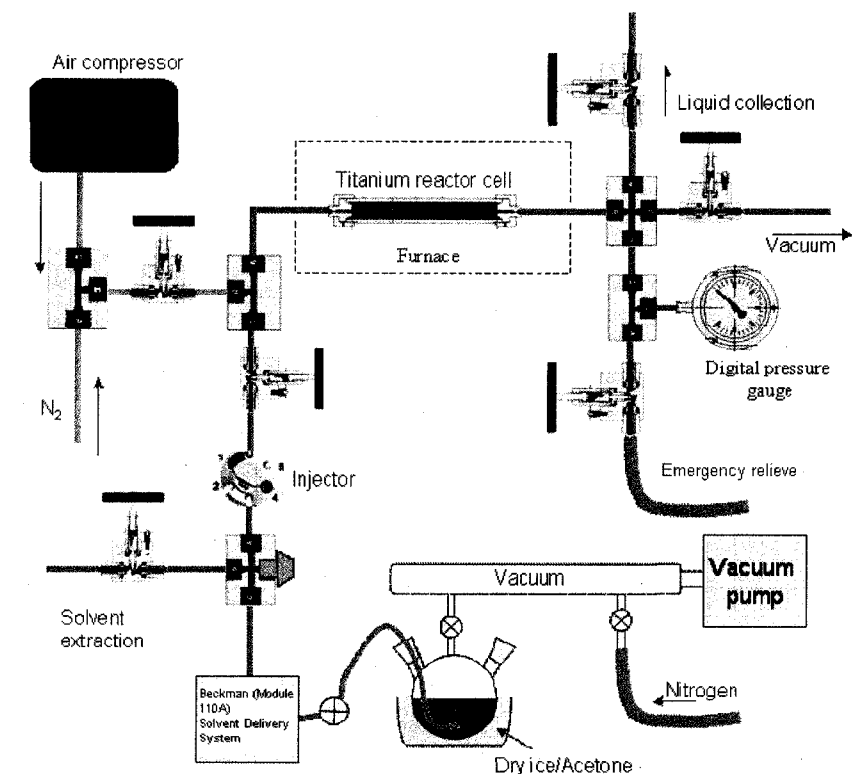


Figure 5. A supercritical high temperature and pressure flow reactor system.

### 2.2.1. Sample preparation

A 842  $\mu\text{M}$  diol- $\text{Au}^0$  nanoparticles solution was synthesized as described in method presented in Appendix A.

A loading sample solution was prepared by combining diol- $\text{Au}^0$  nanoparticles solution with diphenylsilane (DPS). Diol- $\text{Au}^0$ , DPS and cyclohexane solution were

relatively immiscible. This made it difficult for cyclohexane to transfer the precursor into the Ti reactor. To solubilize the solutions isopropyl alcohol (IPA) was first pipetted into diol-Au<sup>0</sup> solution gradually until the mixture becomes miscible. 80  $\mu$ L of the diol-Au<sup>0</sup>/IPA solution was pipetted into a clean vial followed by addition of 60  $\mu$ L of DPS. More IPA was added until all components became miscible.

## **2.2.2. Procedure**

### **2.2.2.1. Deoxygenation of solvent and Ti reactor**

The cyclohexane solvent was first deoxygenated by the freeze/thaw vacuum process. The cyclohexane solvent was loaded 1/3 full into a 500-mL three-neck round-bottom flask (with angled necks). The middle neck outlet was attached to the vacuum line, and one angled neck was fabricated for high pressure liquid chromatography (HPLC) solvent delivery inlet as illustrated in Figure 6 and air-tight sealed using epoxy. The third neck was used for loading of solvent and plugged with a silicone greased ground-glass stopper.



Figure 6. Three-neck round-bottom flasks for freeze/thaw vacuum deoxygenation of solvent.

The vacuum 2-way valve to the middle neck of the flask was first isolated. The flask was submerged into a small basin filled with dry ice and acetone mix (approximately -

78 °C) to freeze the cyclohexane. The vacuum was turned on to evacuate the vacuum tube. 150 micron (or millitorr) was achieved in the system. Once the cyclohexane was frozen the 2-way valve was opened to vacuum to evacuate the flask. The flask was left under a vacuum for 5 minutes before isolating it from the vacuum line. The round-bottom flask was removed from dry ice/acetone and the frozen cyclohexane was left to thaw. Upon thawing, oxygen bubbled out of cyclohexane into the vacuum. Cyclohexane was then frozen again in acetone/dry ice. The deoxygenation cycle was repeated 2 more times, until no bubbles were observed during the thawing process. Once deoxygenation process was completed the flask was repressurized to atmospheric pressure by bleeding in nitrogen, this allowed the solvent can be drawn into the HPLC pump with ease.

The titanium reactor and the entire delivery line were degassed by purging with nitrogen from the gas inlet port for 2-3 minutes. The system was evacuated for ~20-25 minutes using a port at the end of the reactor. The system was then switched back to nitrogen purge. The cycle was repeated 3 times.

#### **2.2.2.2. Leak and pressure test**

Before each reaction, a pressure test was performed on the system to ensure no the high pressure system was leak free. The Ti reactor was pre-heated to 130 °C with heating tape prior to injection of cyclohexane at a flow rate of 1 mL/min with the HPLC pump. A total of 5.7 mL of cyclohexane was injected and the temperature was gradually increased while pressure was monitored. The pressure with respect to temperature of the heating and cooling cycles were measured for 2 complete cycles,

with first cycle heated to 330 °C and cooled to 120 °C, and second cycle heated to 450 °C before cooling again. The consistency of the final pressure of the system at the end of every cooling phase, indicated that the system was not leaking. Evidence of premature decomposition of the cyclohexane would also be observed at this stage. Any decomposition (combustion) of cyclohexane at elevated temperature would result in a higher final pressure upon cooling to 120 °C due to either anaerobic cracking of cyclohexane to smaller fragment molecules or combustion of cyclohexane to CO<sub>2</sub> or water. Both would result in a higher resultant pressure. The above experimental steps were necessary to eliminate solvent degradation during high temperature and pressure reaction conditions.

#### **2.2.2.3. Synthesis of bulk SiNW using supercritical VLS method**

The reactor was preheated to 350 °C before pumping cyclohexane into the system. Cyclohexane was delivered at a rate of 1 mL/min for 130 sec into the Ti reactor and temperature was increased upon pressure stabilization. Once temperature reached 400 °C, 400 µL of the loading reactant (diol-Au<sup>0</sup>/DPS/IPA/cyclohexane) was injected into the sample injector (200 µL loop) at two different intervals. The Ti reactor pressure reached 2700-2800 psi. Temperature was stabilized at 410 °C and reaction was carried out for 10 min. During the reaction period, pressure would often increase to as high as 2900-3400 psi. After ten minutes of reaction time, the reactor was immediately cooled with an air fan to quench the reaction. Once cooled, the solution product was collected sequentially at the extraction port with fresh

cyclohexane washes. The overall process took about 2-3 hours. Experiments were also carried out at temperatures as high as 500 °C.

### 2.2.3. Observations

Initial trials were carried out without deoxygenation of cyclohexane which results in heavy thermal decomposition of the solvent and thick carbon residue in the reactor. The resultant solution collected was reddish brown in color. IR/NMR studies showed formation of cyclohexanol as a major product. With the freeze/thaw deoxygenation procedure no decomposition was observed. This was further supported in the pressure test at elevated temperature for two consecutive cycles over a two day period, as illustrated in the Figure 7.

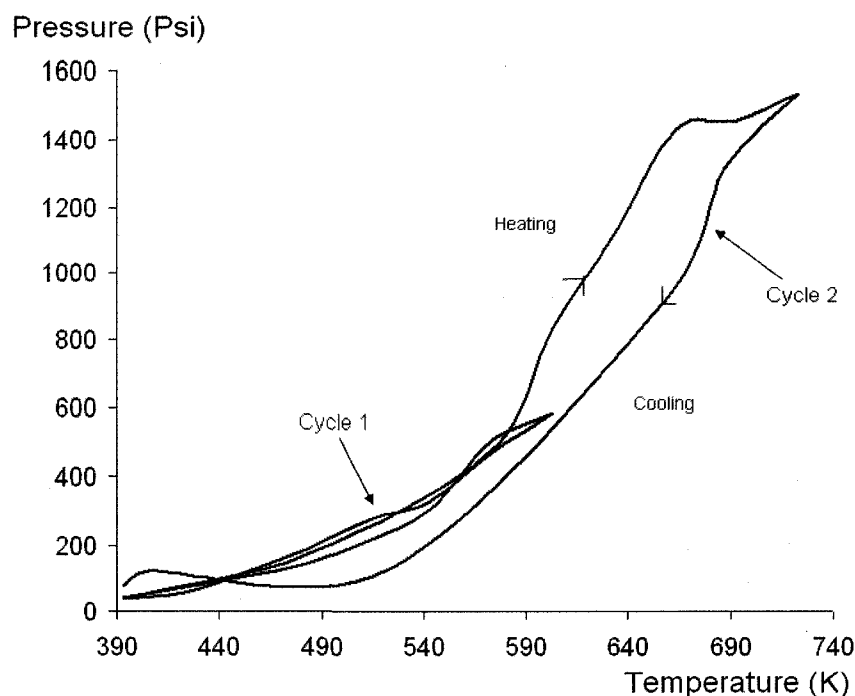


Figure 7. Pressure test of the reactor system with cyclohexane.

Due to high temperature and extreme pressures (>220 atmospheres), a general problem of carbonization<sup>55</sup> and fusion of Si-gold alloy particle in supercritical



cyclohexane solvent was noted, resulting in wide micron size range diameter of silicon wires and carbon deposits.



Figure 8. Optical images of extracted residual from the Ti reactor after multiple reaction runs.

Extraction of the wires was difficult possibly because they tended to get trapped on the Ti reactor walls and excessive flushing with fresh solvent did not facilitate the extraction. Sharma et. al.<sup>56</sup> have reported Ti can catalyze growth of SiNWs at 670 °C, thus the Ti reactor can potentially acts as a Si scavenger. In either case, the volume of nanowires generated was extremely small. Due to these short comings of the supercritical method, new synthesis of SiNWs using low pressure VLS mechanism was developed.

### **Chapter 3. Synthesis of nanowires using VLS mechanism in enclosed glass vessel**

The supercritical high pressure and temperature method failed to produce a decent yield. The two main reasons were due to the decomposition of cyclohexane and extreme high pressure. A new method of synthesis was developed that eliminated the used of supercritical conditions and was based on closed CVD reactor concept<sup>57</sup>.

The tradition flow CVD reactors allow exquisite control over reaction conditions such as pressure, temperature, reagent concentration and flow rate. In a typical CVD reactor, nanoparticles of metallic Catalyst (Au, Fe, Al<sup>58</sup>, Ga<sup>59</sup>, Ti<sup>60</sup>, etc.) are predeposited on to a silicon substrate that is rapidly heated to a temperature above the eutectic of the Si/metal catalyst, under  $10^{-6}$  to  $10^{-2}$  Torr of vacuum. Once the desired temperature is achieved, silane gas and dopants (common dopants include toxic gases such as diborane or phosphine for p- or n-type doping) are injected via mass flow regulators to control the vapor pressure to a point whereby only VLS mechanism dominates producing resultant SiNWs. The overall cost of material used in constructing and maintaining the CVD reactor is a large obstacle. Furthermore, the hazard in handling toxic gases is a huge challenge in synthesis of doped-SiNWs. An inexpensive and green method in synthesis is described.

In what follows, a new low pressure SiNW synthetic method in a sealed glass tube will be presented. The growth of silicon wires on silicon, silicate glass, aluminium and copper surface will be demonstrated. The results revealed that different

substrates tend to produce SiNWs with different diameters with length greater than 40  $\mu\text{ms}$ .

### **3.1. Procedure**

#### **3.1.1. Deposition of gold catalyst**

28  $\mu\text{M}$  diol-Au<sup>o</sup> nanoparticles solution in DMF (refer to Appendix B.5 for synthesis) was used as catalyst for the study. Silicon substrate of dimension  $\square 0.5 \times 1.1 \text{ cm}^2$  was cleaned by sonicating in acetone for 15 minutes. 4  $\mu\text{L}$  of the 28  $\mu\text{M}$  diol-Au (in DMF) solution was pipetted on to the silicon substrate. The substrate was heated to approximately 180 °C to dry off the DMF. A reaction glass tube vessel was fabricated by torch sealing a 0.8 cm (O.D.) and 0.6 cm (I.D.) borosilicate glass tube at one end. The length of the tube was approximately 15 cm long.

#### **3.1.2. Synthesis of silicon nanowires**

20  $\mu\text{L}$  of diphenylsilane (DPS) (108  $\mu\text{mol}$ ) stock solution was carefully injected into the glass tube, ensuring that DPS reaches the bottom of the tube without contacting the side wall. The silicon substrate with gold deposits was inserted into the glass tube. The glass tube was thinned or narrowed down to a neck of about 9 cm from the end/base of the tube with a propane torch for ease of sealing (as inset in Figure 9). The reaction tube was deoxygenated by a freeze-thaw vacuum process as illustrated in Figure 9.

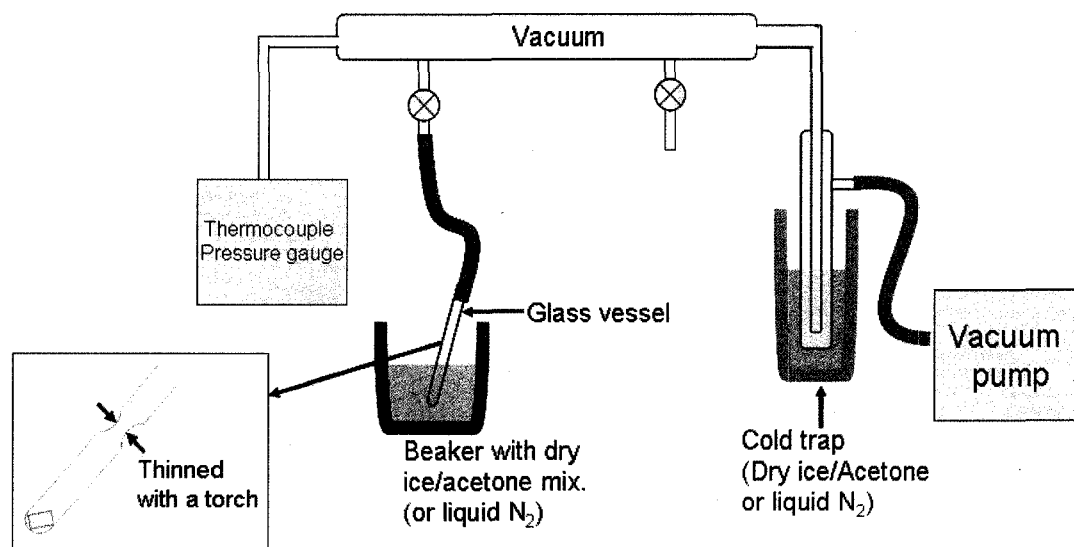


Figure 9. Illustration of vacuum system for freeze/thaw deoxygenation of the glass reaction vessel. [insert: glass tube thinned at the neck with a torch.]

The open end of the reaction vessel was attached to a vacuum line connected to a mechanical vacuum pump (Welch Vacuum, Model no. 1402B-01). The DPS in the reaction tube was first frozen by submerging the bottom of the tube in acetone/dry ice mix or liquid N<sub>2</sub>. Freezing of the DPS was to prevent it from evaporating away while under vacuum. Once the DPS was frozen the tube was evacuated to vacuum for 5 minutes, while the tube was still in acetone/dry ice. After 5 minutes the vacuum line to the tube was isolated and the DPS was thawed by removing from acetone/dry ice or liquid N<sub>2</sub>. During thawing, oxygen was bubbled out of DPS into the vacuum. DPS was then frozen again in acetone/dry ice or liquid N<sub>2</sub>. The tube was evacuated in vacuum for another 5 minutes ( $P \sim 100$  mTorr). The tube was then torch sealed with a propane torch at the neck of the tube. The completed reaction glass vessel has a length of approximately 9 cm; reactor volume ( $\pi \times 0.6^2 \times 9 \text{ cm}^3 \approx 10 \text{ cm}^3$ ).

The reaction vessel was placed in a furnace (Thermolyne 47900) and gradually heated to 450 °C, at a heating rate of 3.75 °C/min. Once the temperature reached 450 °C the reaction vessel was maintained at this reaction temperature for 1 hour; afterwards the vessel was cooled to room temperature.

The following preliminary characterization/analysis was performed on the samples: 1.) SEM; 2.) AFM; 3.) Photoluminescence; and 4.) optical excitation and emission.

### 3.2. Results



Figure 10. Si nanowires synthesized on a silicon substrate in a glass vessel.

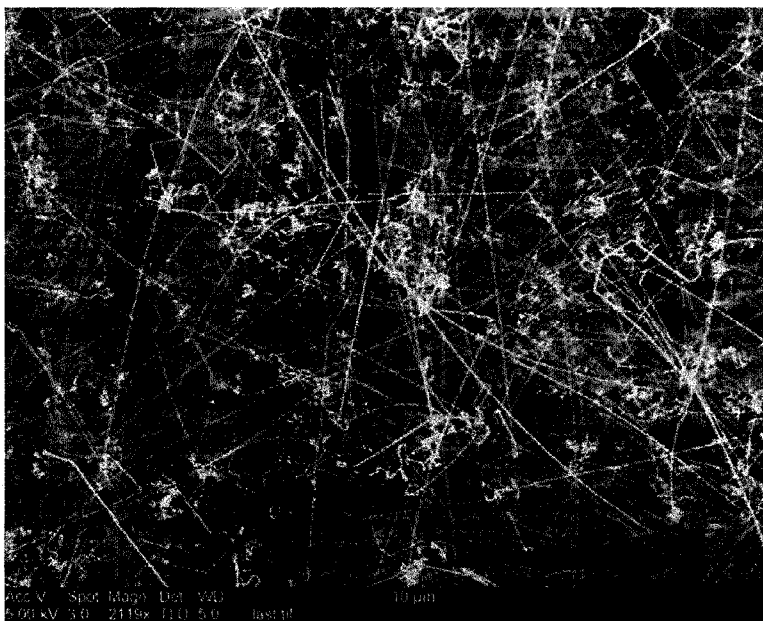


Figure 11. SEM image of SiNWs synthesized on a silicon substrate (DPS=108  $\mu$ mol; reaction temperature of 450 °C and time of 1 hr 43 min).



Figure 12. Optical excitation and emission of Si nanowires on silicon and copper substrates (images collected on Zeiss optical microscope with filter set 9 and 15).

After the reaction the internal wall of the glass tube were coated with some yellowish deposits (Figure 10). The SiNWs synthesized have diameter  $\sim 60$  nm and length  $>40$   $\mu\text{m}$ . A combination of straight wires and bundle of bent wires that seem to be directionless were observed in the SEM images in Figure 11. It has been reported that the bends in the wires were due to growth defects in the lattice of the crystals. Further experiments to improve and optimize the reaction conditions were carried out in order to eliminate crystal defects.

The sample was placed under a Zeiss optical microscope equipped with wavelength filters. When the sample was excited with an arc lamp, emission was observed and the optical images were captured as illustrated in Figure 12. Filter set 9 has excitation range from 450-500 nm and emission range from 510-800 nm. Filter set 12 has excitation range from 540-500 nm and emission range from 580-750 nm.

Further excitation-emission spectroscopy characterizations were performed in later experiments, using a fluorometer.

### **3.3. Time of reaction, temperature, concentration and pressure dependent studies on the effect of SiNWs synthesis**

The Thermolyne 47900 furnace suffers a great loss in temperature during sample loading and the actual core temperature was not calibrated. The furnace was replaced with the Lindberg tube furnace (1¾ inch diameter and 14 inches long heating core). A 14 inch long and ¾ inch diameter copper pipe tubing with one end capped was inserted into the Lindberg furnace to hold the glass tube. The core temperature of the copper pipe was calibrated. (Appendix E)

In order to attain reproducibility in results and controllability in the system, optimization in both the synthesis procedure and reaction conditions have to be performed. Synthesis procedure and conditions such as reaction time, reaction temperature, reagent concentrations and pressure of the system, affect the resultant size and shapes SiNWs.

#### **3.3.1. Effect of diphenylsilane to Au ratio on synthesis of SiNWs**

##### **3.3.1.1. Procedure**

The DPS concentration was varied: 4.8, 8.0, and 16.0 µmols. Reaction condition was as follow:  $1.7 \times 10^{-10}$  mols Diol-Au<sup>0</sup> nanoparticles (in DMF); reaction temperature at 450 °C and reaction time at 25 min.

### 3.3.1.2. Results

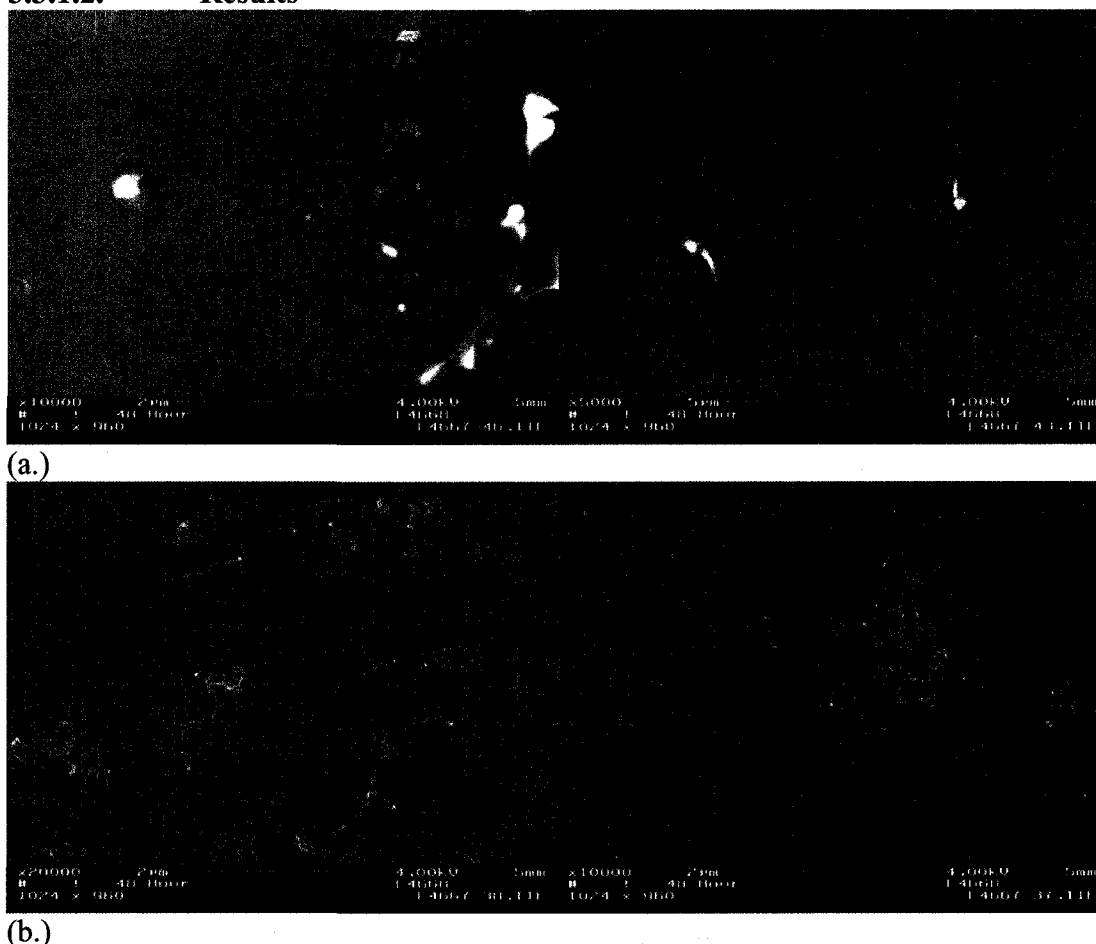


Figure 13. SiNWs synthesized with a.) 8.0  $\mu\text{mols}$  and b.) 16.0  $\mu\text{mols}$  of DPS (with reaction time and temperature held constant at 25 min and 450  $^{\circ}\text{C}$ ).

No SiNWs were observed for DPS concentrations less than 8.0  $\mu\text{mols}$ . The lengths of the SiNWs were  $5.4 \pm 0.5 \mu\text{m}$  for 8.0  $\mu\text{mols}$  DPS and  $0.69 \pm 0.18 \mu\text{m}$  for 16.0  $\mu\text{mols}$  DPS. The diameters of the SiNWs were  $127 \pm 38 \text{ nm}$  and  $41 \pm 8 \text{ nm}$ , corresponding to 8.0  $\mu\text{mols}$  and 16.0  $\mu\text{mols}$  of DPS used, respectively. Due to the large dead volume in the reaction tube, loss of DPS by Si precursor nucleating at the inner tube wall could affect the amount of Si reaching the Au on the substrate.

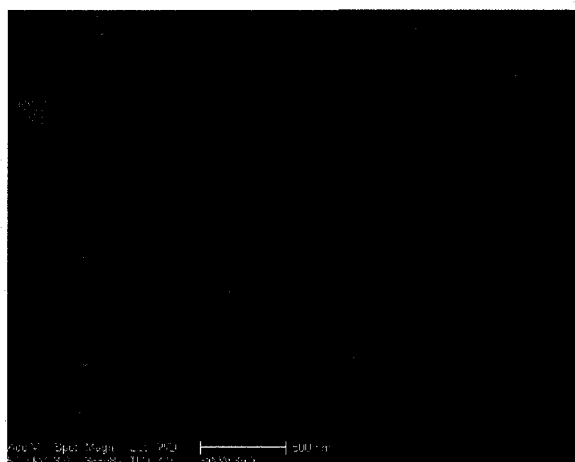


### 3.3.2. Effect of reaction time on synthesis of SiNWs

#### 3.3.2.1. Procedure

Different reaction times were studied: 1.) 3 min 20 sec; 2.) 5 min 30 sec; and 3.) 7 min 10 sec. Reaction conditions are as follow: mole ratio Au:DPS = 1 : 9.6( $10^5$ ) and reaction temperature of 450 °C.

#### 3.3.2.2. Results



(a.)



(b.)

Figure 14. SEM images of SiNWs synthesized on Si substrate with reaction times of a.) 3 min 20 sec and b.) 7 min 10 sec.

No SiNWs were observed for reaction time of less than 6 minutes. From this experiment there seemed to be a time and temperature lag for the substrate to reach the

desired temperature. This information can be used as a correction factor later in designing a more optimal and reliable system.

From the early works of Westwater et. al.<sup>61</sup>, growth of SiNWs via VLS mechanism with Au as catalyst can begin at a temperature as low as 320 °C at 1.0 Torr silane partial pressure. SiNWs growth from such conditions were thin (10-25 nm) and appeared to twist and turn frequently with random directional growth. As temperature increased the number of kinks and bends decreased (also observed with decrease in silane partial pressure studies) resulting in straight NWs. These characteristics were also observed in the current studies.

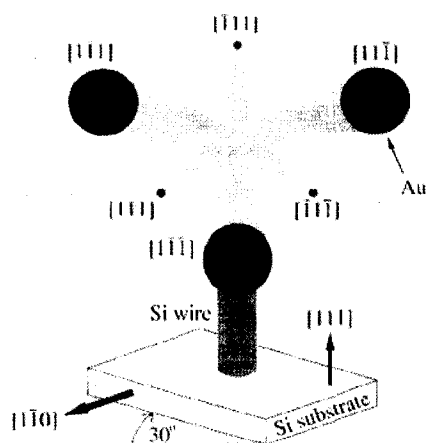


Figure 15. Wire growth direction switching to other  $\{111\}$  directions<sup>61</sup>.

In attempt to eliminate the thinner-bent wires formed during initial temperature lag, the system was redesigned. A dual chamber tube was fabricated.

### 3.3.3. Dual chamber tube

The glass reaction tube (0.8 cm O.D. x 0.6 cm I.D. x 18 cm long) was sectioned to two chambers. DPS was first pipetted in to the glass tube carefully ensuring the solution reaches the bottom of the tube and not on the sidewalls. The tube

was then thinned to a neck with a propane torch at approximately 5 cm from the bottom of the tube. The Au coated substrate was then inserted into the tube. The thinned neck prevents the substrate from reaching the DPS. The top of the tube was thinned to a neck with a propane torch approximately 13 cm from the bottom of the tube for ease of sealing (Figure 16).

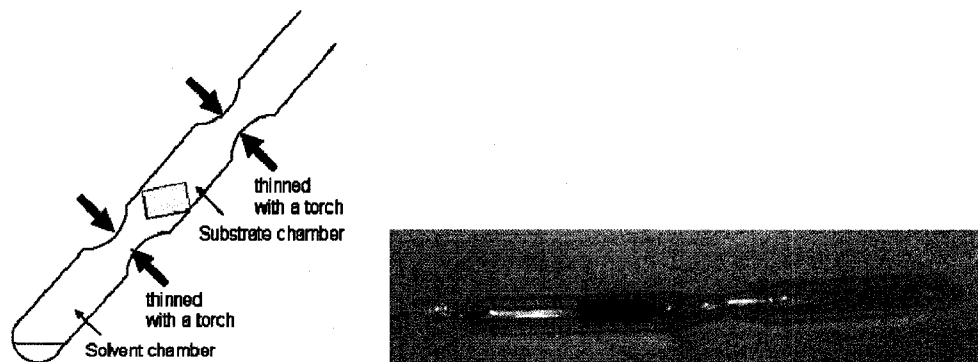


Figure 16. Duo chamber glass reaction tube.

DPS was de-oxygenated via freeze/thaw vacuum technique and finally evacuated and sealed with a propane torch.

The Lindberg furnace was replaced with a lab built glass furnace that had a higher thermal stability and controllability. Temperature calibrations were performed on the glass furnace (Appendix E). From the calibration, it took 130 seconds for a glass tube to reach a preheated furnace temperature of 500 °C.

During synthesis, to ensure the substrate reaches the desired temperature before the reaction, only the substrate chamber end was inserted into the core which was preheated to the desired temperature. The DPS chamber was left out of the heated region. The tube was maintained at that location for a minimum of 5 minutes before being fully inserted into the heated region, this process ensured that the substrate was

at the desired reaction temperature before DPS decomposition commenced. Further experiments were carried out using the dual chamber method.

#### 3.3.4. Effect of diol-Au<sup>0</sup> catalyst surface deposition on the synthesis of SiNWs

Diol-Au<sup>0</sup> nanoparticles solution deposition on substrate generally involves pipetting a measurable volume on to the substrate. The subsequent step involves evaporation of DMF by heating. Evaporation generally results in uneven deposition/dispersion of Au nanoparticles on substrate. Evaporation occurs more rapidly at the outer edge (ring) of the droplets, due to high surface energy, and recedes in to the centre of the drop. Regions of high and low concentration of Au<sup>0</sup> are observed. Gold has high mobility<sup>62,63</sup> at elevated temperature. Thus, eutectic liquid particles could fuse in the high concentration Au<sup>0</sup> region producing SiNWs with larger diameter. A bimodal distribution in diameter was also observed in certain studies, might arise from SiNW initiated in the densely versus sparsely populated regions of nanoparticle catalyst.

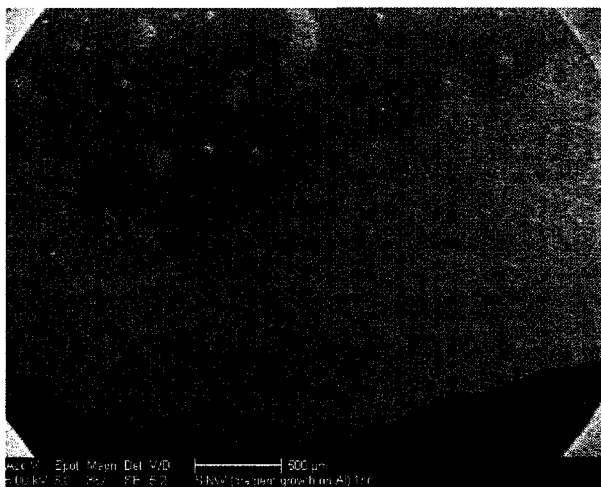


Figure 17. Low resolution SEM image of an edge of the catalyst droplet used to synthesize SiNWs. (The outer edge has high density of SiNWs and core has lower density)

A spray deposition method was developed to deposit gold. A N<sub>2</sub> pressurized paint spray gun was attached to a lab built manual adjust z- and y- stage (Figure 18). The diol-Au<sup>0</sup> solution was sprayed on to the Si substrate with 5 psi of N<sub>2</sub> and from a controllable y-distance from the nozzle. The substrate was heated to evaporate off DMF.



Figure 18. N<sub>2</sub> pressure spray gun for deposition of catalyst solution

#### **3.3.4.1. Procedure**

7  $\mu$ L of DPS was used. The spray deposited gold substrates were inserted into the glass tubes. The reaction was carried out at 500 °C and at two different lengths of time; 1 hr and 1.5 hrs. Figure 19 shows the images from SEM analysis that was performed on the resulting samples.

### 3.3.4.2. Results

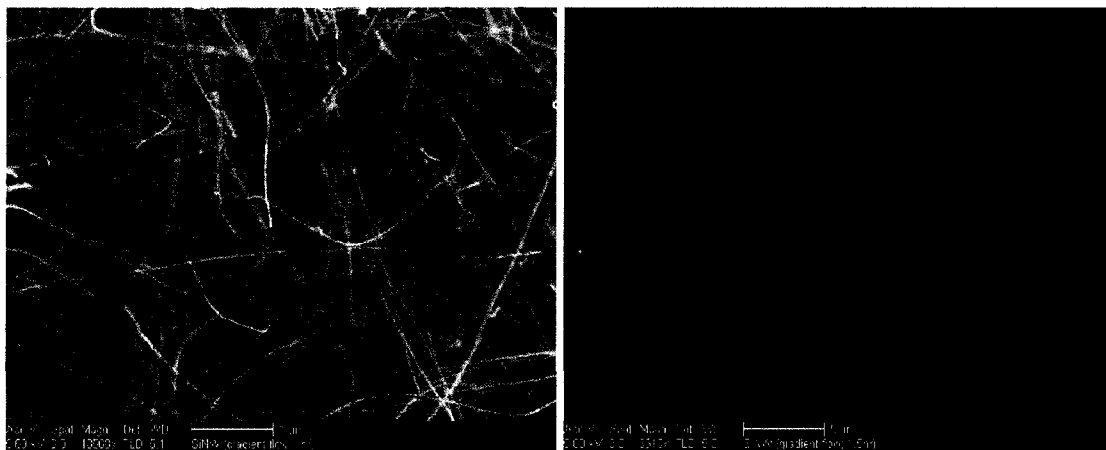


Figure 19. SEM images of SiNWs synthesized from spray deposition of gold; a.) reaction time of 1hr (left); and b.) reaction time of 1.5 hrs (right).

The SiNWs were straight and thin with a uniform diameter of  $23.2 \pm 5.7 \text{ nm}$ . Growth of SiNWs was parallel to the surface of the substrate. Small quantities of SiNWs still exhibited kinks and bents. From the TEM image illustrated in Figure 20, the SiNW is single crystalline with growth direction along the  $[1,1,0]$  plane (refer to Appendix F for lattice plane determination). This is consistent with reports that SiNWs less than 20 nm exhibit growth in the  $[1,1,0]$ <sup>64,65</sup> direction, and larger wires in the  $[1,1,1]$  direction (refer to Appendix F, Figure F6). The SiNWs have a sheath of oxide surrounding the crystalline core (approximately 13 nm), which presumably develops upon exposure to air.

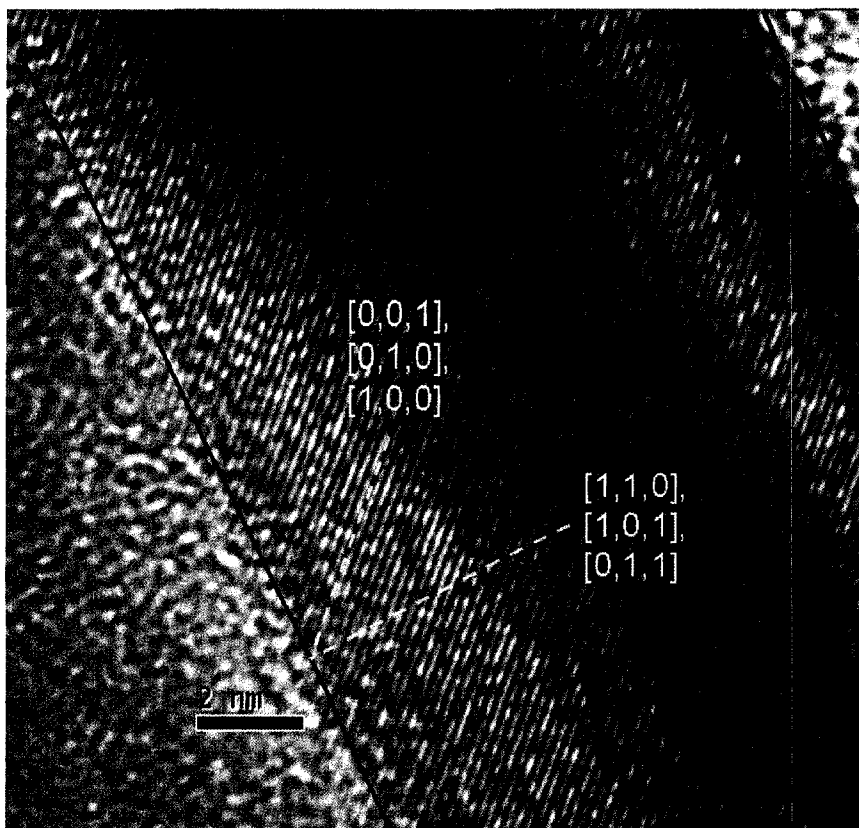


Figure 20. TEM image of SiNW synthesized at 500 °C for 1hr

### 3.3.5. Effect of reaction temperature on synthesis of SiNWs

#### 3.3.5.1. Procedure

Three silicon substrates were heavily sprayed with 28  $\mu\text{M}$   $\text{Au}^0$  nanoparticles solution then heated to 180 °C. This process was repeated three times. A total of 7  $\mu\text{L}$  of DPS was used. The reaction was carried out at 4 different temperatures: 500, 550, 600 and 650 °C. Reaction times were held constant at 30 min for this study. SEM analysis was performed on the samples.

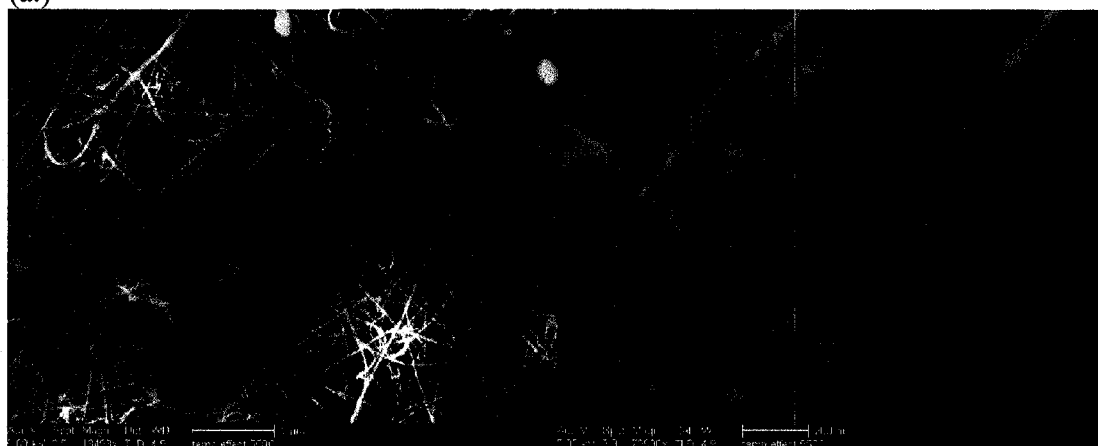
Acc. #	Dist. Map	Dist. WD	Scale
6710	1000	100	1:1000

200 cm

Acc. #	Dist. Map	Dist. WD	Scale
6711	1000	100	1:1000

200 cm

(a.)



(b.)



(c.)

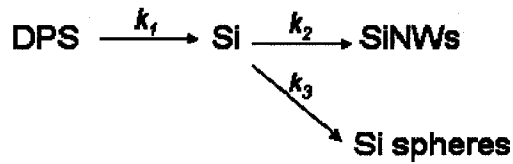




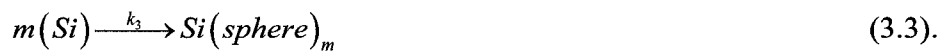
### 3.3.5.3. Discussion

#### A.) Rate of reaction

Our tentative interpretation of the temperature dependent structures is based on following crude kinetic consideration. Consider the system as consecutive irreversible reactions with an intermediate [Si] and two products, nanowires and spheres.



The model assumes that a decomposition of DPS will results in the formation of an unstable intermediate of Si. The [Si] could be consumed in two competing pathways either the Si sphere or SiNW. VLS mechanism could completely suppressed, ( $k_2=0$ ), when the reaction is carried out in the absence of  $\text{Au}^0$ . Alternatively when Au nanoparticles are present,  $k_2$  could be enhanced. At elevated temperature, the rate of DPS decomposition is fast (large  $k_1$ ) thus this is not a rate determining step. The rate constants  $k_2$  and  $k_3$  are also inherently temperature dependent and change with temperature. Whichever product(s) dominates would depend on the ratio of  $k_2$  to  $k_3$  and the stoichiometry of the respective reaction.



Two limiting conditions are considered: 1.) all DPS spontaneously decomposed to Si, and 2.) not all DPS decomposed to Si vapor but a steady state for [Si] is established.

### A1.) Model 1. Spontaneous decomposition of DPS

The rate of formation of SiNWs can be written for equation (3.2) as,

$$R_1 = \frac{d[SiNW]}{dt} = k_2 [Au^o] \cdot [Si]^n \quad (3.4)$$

The rate of formation of Si sphere can be written for equation (3.3) as,

$$R_2 = \frac{d[Si(sphere)]}{dt} = k_3 \cdot [Si]^m \quad (3.5)$$

The ratio of the rate of reactions is,

$$\frac{R_1}{R_2} = \frac{k_2 [Au^o] \cdot [Si]^n}{k_3 \cdot [Si]^m} = K \cdot [Si]^{(n-m)} \quad (3.6)$$

From equation (3.6), one can conclude that  $\frac{R_1}{R_2} \propto [Si]^{(n-m)}$ . Thus if  $m \gg n$ ;

$$\frac{R_1}{R_2} \propto [Si]^{(n-m)} \xrightarrow{\lim m \gg n} \frac{1}{[Si]^m} \quad (3.7)$$

Therefore, at high temperature when the silicon concentration in the vapor phase is high the ratio  $R_1 / R_2 \ll 1$ , meaning that the rate of Si sphere formation would dominate the rate of SiNWs formation. In other words, the rate of heterogeneous nucleation would exceed rate of nanowires crystallization mediated through Au nanoparticles. This results in higher density of Si sphere and lower quantity of SiNWs. However at low temperatures, the Si concentration in vapor is low,  $[Si] \ll 1$ , so  $R_1 / R_2 \gg 1$ . Under these conditions, the rate of SiNWs formation dominates the rate of Si sphere formation. This results in a higher density of SiNWs and lower quantity of Si spheres.

## A2.) Model 2. Steady decomposition of DPS

Using steady state approximation, for Si is,

$$\frac{d[Si]}{dt} = k_1 [DPS] - k_2 [Si]^n - k_3 [Si]^m = 0 \quad (3.8)$$

Consider  $m \gg n$ , and assigning  $n=2$  and  $m=4$  into equation 3.8.

$$k_1 [DPS] - k_2 [Si]^2 - k_3 [Si]^4 = 0$$

Solving the quadratic equation, i.e.  $\alpha - \beta x^2 - \gamma x^4 = 0$ ;

$$x^2 = \frac{\beta \pm \sqrt{\beta^2 + 4\alpha\gamma}}{-2\alpha}$$

$$[Si]^2 = \frac{-k_2 \pm \sqrt{k_2^2 + 4k_1 [DPS] k_3}}{2k_3}$$

$$[Si] = \sqrt{\frac{-k_2 \pm \sqrt{k_2^2 + 4k_1 [DPS] k_3}}{2k_3}}$$

$$[Si] = \sqrt{\frac{-k_2}{2k_3} \pm \frac{k_2}{2k_3} \sqrt{1 + \frac{4k_3 k_1}{k_2^2} [DPS]}}$$

Solving using Taylor's expansion, thus

$$[Si] = \sqrt{\frac{k_1}{k_2}} [DPS] \quad (3.9)$$

Substituting solution (3.9) into equation (3.4) and (3.5),

$$R_1 = \frac{d[SiNW]}{dt} = k_1 [DPS] \quad (3.10)$$

$$R_2 = \frac{d[Si(sphere)]}{dt} = \frac{k_3 k_1^2}{k_2} [DPS]^2 \quad (3.11).$$

Thus the ratio

$$\frac{R_1}{R_2} = \frac{k_2^2}{k_3 k_1 [DPS]} \quad (3.12).$$

The rate determining step is the temperature dependent DPS decomposition  $k_1$ , which can be written using Arrhenius equation as,

$$k_1 = A e^{-E_{a1}/RT} \quad (3.13).$$

The rate constants  $k_2$  and  $k_3$  also exhibits Arrhenius type behavior, thus they can be written as,

$$k_2 = A e^{-E_{a2}/RT} \quad (3.14)$$

$$k_3 = A e^{-E_{a3}/RT} \quad (3.15)$$

Substituting equation (3.13) – (3.15) into (3.12),

$$\frac{R_1}{R_2} = \frac{A_2^2}{A_1 A_3 [DPS]} \cdot e^{(E_{a1} + E_{a3} - 2E_{a2})/RT}$$

$$\frac{R_1}{R_2} = \frac{A_2^2}{A_1 A_3 [DPS]} \cdot e^{E_a/RT} \quad (3.16).$$

Where  $E_a = E_{a1} + E_{a3} - 2E_{a2}$ .

A model plot of  $R_1/R_2$  versus the reaction temperature was illustrated in Figure 22, with  $n=2$ ,  $m=4$ ,  $A_2=1.0 \times 10^{-5}$ ,  $A_3=1.0 \times 10^{-2}$ ,  $A_1=1.0 \times 10^{-3}$  and  $E_a=38$  kJ/mol (arbitrary value).

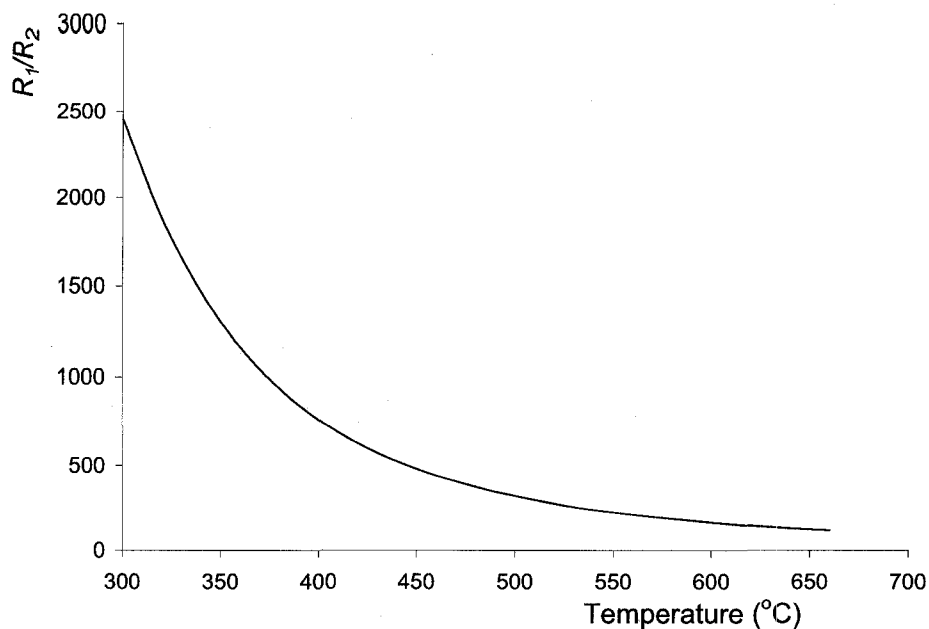


Figure 22. A model plot of ratio  $R_1/R_2$  as a function of temperature.

At low temperatures, the rate of SiNWs formation supersedes Si particles. As the temperature is increased the ratio of  $R_1/R_2$  decreases until it reaches a plateau suggesting Si particles formation suppresses wires formation.

From the derived equation 3.12, the ratio  $R_1/R_2$  is inversely dependent on  $k_1$ . By selecting a Si precursor with high  $k_1$ , the rate of SiNWs formation can be suppressed. Alternatively, by selecting a Si precursor with a low  $k_1$  the rate of SiNW can be increased. This was observed when triphenylsilane was used as Si precursor. SEM images of this experiment at various temperatures are shown in Figure 23.



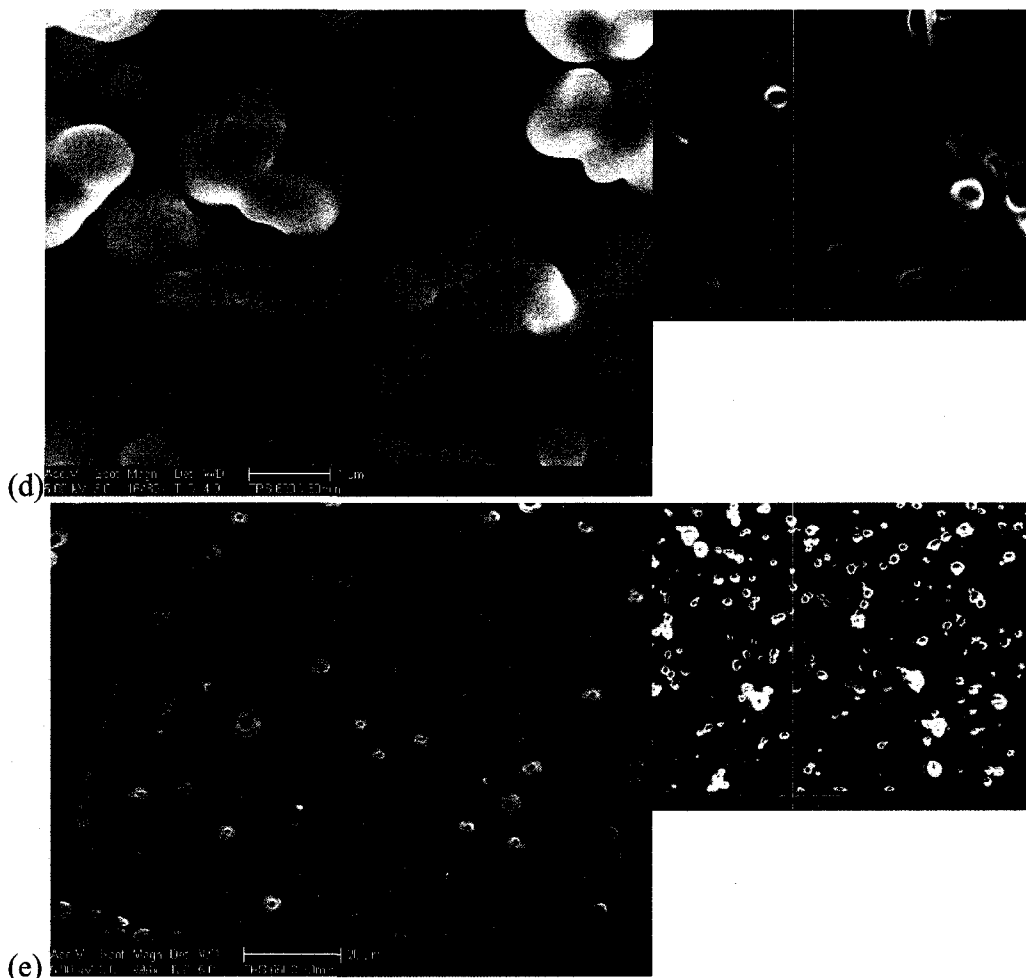


Figure 23. SEM images of SiNWs synthesized with triphenylsilane at different temperature: (a) 450 °C; (b) 500 °C; (c) 550 °C; (d) 600 °C; and (e) 650 °C. [Smaller images to the right are synthesis with comparable condition using DPS as Si precursor].

Triphenylsilane (TPS) has a different decomposition rate thus a different  $k_f$  value. At 450 °C, the growth of SiNWs is delayed and only Au particles with a tail of crystallizing Si were observed. This suggests that TPS has a higher activation energy than DPS, or a lower  $k_f$ . A lower  $k_f$ , should result in higher rate of SiNWs formation. In Figure 23d the absence of Si particles at 600 °C with TPS, can be compared to the DPS image where SiNWs and Si particles are observed. However, the Si wires are much shorter and larger in diameter. Finally, at 650 °C the rate of Si particles



formation exceeds any formation of SiNWs for both cases, and no wires are observed. Thus, if tetraphenylsilane were to be used, the  $k_I$  could be lowest among the phenylsilane series and reaction could be carried out at slightly elevated temperature.

Results for synthesis using triphenylsilane (TPS)						With DPS	
temp (°C)	mass used (g)	moles (μmol)	reaction time (min)	Si		Si	
				NW	Sphere	NW	Sphere
				(diameter, nm)		(diameter, nm)	
450	0.01	38	30	--	--	21±1	--
500	0.01	38	30	37±7	--	21±5	--
550	0.005	19	30	59±6	--	28±10	--
600	0.005	19	30	644±68	--	416±88	4687±848
650	0.005	19	30	--	4900±1000	--	3926±925

Table 2. Comparison of Si NW/Sphere synthesized using TPS versus DPS

The results are summarized in Table 2. It can be seen that the SiNWs synthesized from TPS have larger diameters than SiNWs synthesized from DPS. This could be due to the lower decomposition rate of TPS (i.e. lower  $k_I$ ), resulting in a lower Si concentration in the vapor. The Si concentration in the vapor (supersaturation) has an inverse relation with the size of the SiNWs and this will be discussed in model B below.

#### B.) Model for diameter of Silicon nanowires grown through VLS mechanism

The first kinetic model of VLS growth mechanism was studied by Givargizov et. al.<sup>66</sup> The critical diameter,  $d_c$ , of the NWs is dependent on the supersaturation of the vapor phase following Gibbs-Thomson rule.

$$\Delta\mu = \Delta\mu_0 - \frac{4\Omega\alpha}{d} \quad (3.17)$$

Where  $\Delta\mu$  is the chemical potential difference between the Si in vapor and in the SiNW,  $\Delta\mu_0$  is the equilibrium chemical potential difference between Si in the vapor and Si at the plane boundary,  $\alpha$  is the specific free energy of the SiNW, and  $\Omega$  is the

atomic volume of Si. In equation (3.17) when equilibrium is reached, the chemical potential of Si in the vapor, liquid and solid are equal, and a finite minimum critical diameter of SiNW exists, this is known as the critical diameter,  $d_c$ . When this occurs,  $\Delta\mu \rightarrow 0$ , and equation (3.17) simplifies into,

$$\Delta\mu_0 = \frac{4\Omega\alpha}{d_c} \quad (3.18).$$

Thus, most observed NW should exhibit diameter larger than  $d_c$ . When the Si nucleates into a crystal, the chemical potential difference between the Si in the metal nanoparticle and in the SiNW crystal phase is also given by,

$$\Delta\mu_o = k_B T \ln x \quad (3.19)$$

Where  $x = \frac{S}{S_o}$ .  $S$  is the concentration of Si in the vapor and  $S_o$  is the solubility or equilibrium concentration of Si in the catalyst.  $S_o$  is temperature dependent. Equating equation (3.18) and (3.19), this gives rise to the critical diameter relation with the concentration of Si vapor.

$$d_c = \frac{4\Omega\alpha}{k_B T \ln x} \quad (3.20).$$

From this relation, to have SiNWs with small diameter the concentration of Si in the vapor has to be large, ie  $\frac{S}{S_o} \gg 1$ . Thus,  $x$  is the measure of Si supersaturation in the metal catalyst. The critical diameter is inversely proportional to the supersaturation of Si vapor that depends on DPS concentration. Expanding equation 3.20,

$$\frac{1}{d_c} = \frac{k_B T}{4\Omega\alpha} \ln S - \frac{k_B T}{4\Omega\alpha} \ln S_o \quad (3.21).$$

From equation 3.21, a plot of  $1/d_c$  with respect to  $\ln S$  should predict a linear relation.

Concentration of DPS and diameter data were extrapolated from various studies presented above are plotted in Figure 24.

Moles DPS ( $\times \mu\text{mols}$ )	$\ln S$	$1/d_c$ ( $\text{cm}^{-1}$ )
108	4.7	384615
81	4.4	263158
54	4.0	322581
38	3.6	476190
16	2.8	243902
8	2.1	78740

Table 3. SiNWs diameter with respect to number of moles of DPS (at constant reaction temperature of 450 °C).

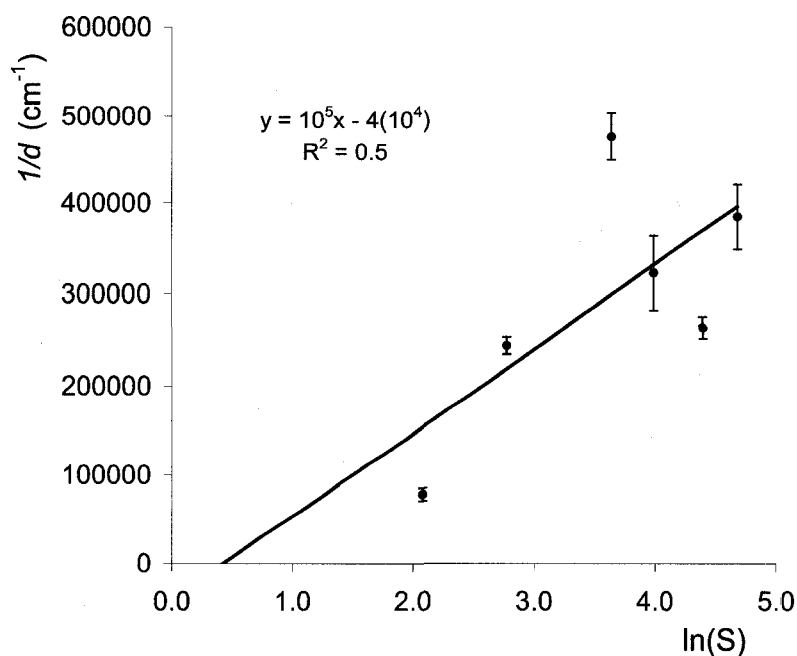


Figure 24. Plot of SiNWs mean diameter with respect to number of moles of DPS.

The SiNWs diameter has an inverse relation with the concentration of DPS as predicted by Givargizov model. Thus, this provides a semi-quantitative control for synthesizing SiNWs with desirable diameter simply by controlling the concentration

of DPS in the reactor. The data shown above corresponded to reaction carried out at 450 °C. For reactions carried out at different temperatures the  $d_c$  will deviate from the plot, but the  $d_c$  concentration relation may well be consistent with the theory. Using

$$\Omega = \frac{2 \times 10^{-23} \text{ cm}^3}{1 \text{ atom Si}}; \alpha = 1600 \text{ erg/cm}^2, \text{ and } T = 723 \text{ K, we estimated the slope } \left( \frac{k_B T}{4\Omega\alpha} \right) \text{ to}$$

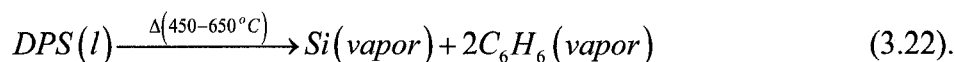
be about  $7.8 \times 10^5 \text{ cm}^{-1}$ . While the experimental results gave a slope of  $10^5 \text{ cm}^{-1}$  which is in the same order of magnitude of predicted value.

We observed a significant increase in NWs diameter as the synthesis temperature was increased. This could be understood in terms of a decrease in the  $\ln x$  term near the eutectic point. Away from the eutectic point the melting point rises and the solubility or saturation concentration of Si in Au also increases. This leads to decrease in supersaturation and according to equation 3.20, leading to increase in  $d_c$ . An alternate explanation of the increased diameter could be that the Au/Si liquid nanoparticles diffuse faster at higher temperature and coalesce into larger sized nanoparticles capable of nucleating larger diameter nanowires. Under realistic conditions both the mechanisms are likely to prevail. Unless Au particles are immobilized, the two effects are difficult to disentangle.

### C.) Mass flow and wetting considerations during the growth of nanowires

Growth of SiNWs on any of the surface using the sealed glass tube method has been observed to be parallel and not normal to the surface as commonly observed in flow CVD reactors. This is observed in the initial growth as illustrated in Figure 13 and 14. Such growth implies eutectic liquid tends to wet the substrate in the closed

CVD system. The relatively high silicon precursor pressure (Table 4) used in the chamber could possibly quench the chemical potential gradient driven surface normal growth process, i.e., surface depletion length is effectively zero<sup>67</sup>. The relative silicon vapor pressure in the tube is determined by assuming all DPS decomposes into vapor. Assuming one mole of DPS decomposes into one mole of Si and two moles of benzene,



By using the ideal gas equation  $PV = nRT$  the internal pressure can be determined, where  $V$  represents the internal volume of the tube (0.015 L),  $n$  is the total number of moles of decomposed products, and  $T$  is the reaction temperature.

Vol. of DPS used ( $\mu$ L)	# moles DPS ( $\mu$ moles)	# moles Si+benzene ( $\mu$ moles)	Temperature ( $^{\circ}$ C)				
			450	500	550	600	650
			Internal Pressure (atm)				
0.9	4.8	14	0.06	0.06	0.07	0.07	0.07
1.5	8.0	24	0.10	0.10	0.11	0.12	0.12
3.0	16.0	48	0.19	0.21	0.22	0.23	0.25
4.0	21.6	65	0.26	0.28	0.30	0.31	0.33
5.0	27.0	81	0.33	0.35	0.37	0.39	0.42
7.1	38.0	114	0.46	0.49	0.52	0.56	0.59
8.0	43.0	129	0.52	0.56	0.59	0.63	0.66
10.0	54.0	162	0.65	0.70	0.74	0.79	0.83
15.0	81.0	243	0.98	1.05	1.12	1.18	1.25
16.0	86.0	258	1.04	1.11	1.18	1.26	1.33
18.6	100.0	300	1.21	1.29	1.38	1.46	1.54
20.0	107.8	323	1.30	1.39	1.48	1.57	1.67

Table 4. Internal pressure of glass tube assuming complete decomposition of the DPS (the internal volume of the sealed glass tube is 0.015 L).

Studies of growth kinetics of NWs using VLS model have revealed importance of two regimes. One is with respect to vapor phase concentration (hence flux flowing into liquid eutectic) of reactant and second is when diffusion flux of Si from the

surface of preformed nanowires. In the former case, Givargizov<sup>66</sup> showed that the Length of NW  $\sim (A-B/R)^2$ , where R is the radius of the NW. This relationship implies smaller wires grow more slowly than larger wires, due to Gibbs-Thompson effect. In other limit, where the diffusion on the NW surface is fast and its contribution overwhelms the direct adsorption flux, Dubrovsky<sup>68</sup> shows that  $L \sim (A+B/R)^2$ . In this limit the smaller wires grow faster than larger. In our experiments both the limits are relevant, the former at the beginning and the latter near end of the experiment when the vapor phase concentration of DPS is diminished.

The observed surface parallel growth could be rationalized in terms of differences in advancing and retreating contact angles for a partially wetting droplets moving on a solid surface<sup>69</sup> with slightly different balance of surface forces at advancing and receding ends of the drop:

$$v = \frac{Wh\gamma_{LV}}{\mu A} (\cos \theta_a - \cos \theta_r) \quad (3.23)$$

where  $v$ ,  $h$ ,  $\mu$  and  $\gamma_{LV}$  are the surface velocity of droplet, the average height  $h$ , viscosity and air-liquid surface tension respectively.  $A$  is the contact area between liquid droplet and solid surface.  $W$ ,  $\theta_a$  and  $\theta_r$  are constant, advancing and receding contact angles respectively. To realize a small, i.e., few  $\mu\text{m}/\text{min}$  growth rates, the differences in advancing and receding contact angle need be very small. In our system, such a difference in contact angles may arise from adsorption of the decomposition products generated at the catalytic liquid/vapor interface.

During the growth of nanowires, following mass fluxes are relevant; Flux from environment to surface ( $J_0$ ), flux due to surface reaction ( $J_1$ ), diffusional flux of Si towards Au/Si nanoparticle ( $J_{Diff}$ ). Neglecting diffusion of silicon from the surface of nanowire; efflux of NW ( $J_{NW}$ ):

$$J_0 = \frac{P}{\sqrt{2\pi m k_B T}} \quad (3.24)$$

$$J_1 = k_s C_s \quad (3.25)$$

$$J_{Diff} \approx -D \frac{dC}{dz} \approx D \frac{C_s}{\delta} \quad (3.26)$$

$$J_{NW} = -\frac{1}{\Omega} \frac{dz}{dt} \quad (3.27)$$

Here  $\Omega$  is volume of Si atom and other symbols have their accepted meaning. If a steady state growth of nanowire,  $\nu$ , exists then equating the fluxes  $J_{diff}=J_{NW}$ , and integrating (which defines  $\delta$ ):

$$\nu = \frac{dz}{dt} \approx \frac{C_s \Omega D}{\delta} = k_s \Omega C_s \quad (3.28)$$

Here  $\delta$  is a characteristic distance over which the surface bound DPS concentration varies from very small value at the surface of the nanoparticle to a constant equilibrium value of  $C_s$  at  $z=\delta$ . Thus if the surface concentration  $C_s \rightarrow 0$ , so would horizontal VLS growth rate  $\nu$ . Given that our studies employed a high vapor phase saturation, this mechanism appears plausible. Clearly, more careful theoretical studies are needed to explain our observed surface parallel growth.

### 3.4. Summary of SiNWs diameter from optimization experiments

Optimization studies	# moles DPS ( $\mu\text{moles}$ )	Reaction time (min)	Reaction temp. ( $^{\circ}\text{C}$ )	SiNWs diameter (nm)	Si sphere diameter (nm)
Concentration dependent	5	25	450	NA	NA
	8	25	450	$127 \pm 38$	NA
	16	25	450	$41 \pm 8$	NA
Time dependent	54	3.3	450	NA	NA
	54	5.5	450	NA	NA
	54	7.2	450	$31 \pm 11$	NA
Temperature dependent	38	30	500	$21 \pm 5$	NA
	38	30	550	$28 \pm 10$	NA
	38	30	600	$416 \pm 88$	$4687 \pm 848$
	38	30	650	NA	$3926 \pm 925$
Spray deposition of Au	38	60	500	$30 \pm 11$	NA
	38	90	500	$49 \pm 26$	NA

Table 5. SiNWs diameter from optimization experiments



### 3.5. Synthesis of silicon nanowires on different substrates

The basic experiment described previously was repeated on silicate (Gold Seal® Micro slides) glass, surface of copper wire or copper tape, and aluminized silicon substrate.

#### 3.5.1. Silicate glass, aluminized-silicon and copper substrate experiemnts

The silicate glass (1.5x0.5 cm), copper tape (1.5x0.5 cm) and aluminized silicon (40nm Aluminium on 200 nm silicon oxide, ~1.2x0.5 cm) were used as substrate for synthesis of SiNWs. Conditions were as follow: 6  $\mu$ L of 28  $\mu$ M diol-Au (in DMF) solution; 15  $\mu$ L of DPS; reaction temperature and time 460 °C and 25 min. SEM and AFM studies were performed on the samples.

#### 3.5.2. Results

##### 3.5.2.1. SiNWs on Cu

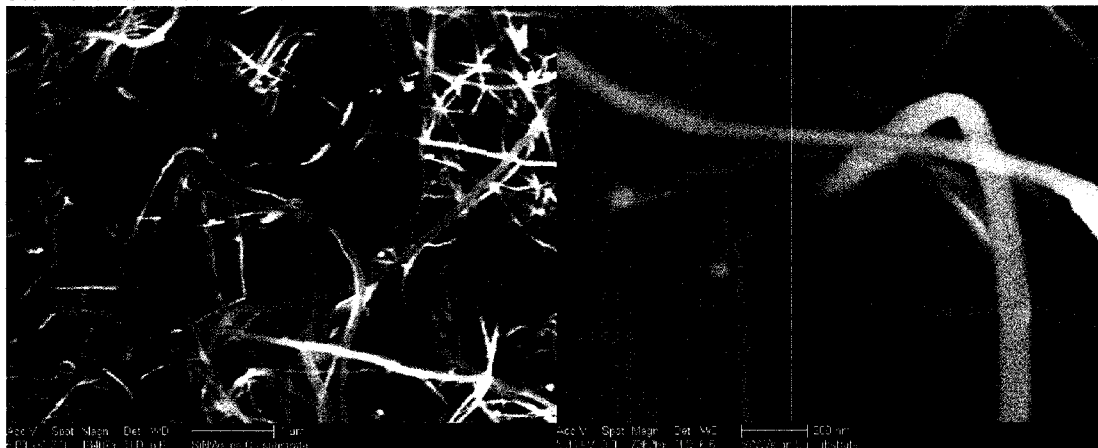


Figure 25. SEM images of Si nanowires grown on copper substrate

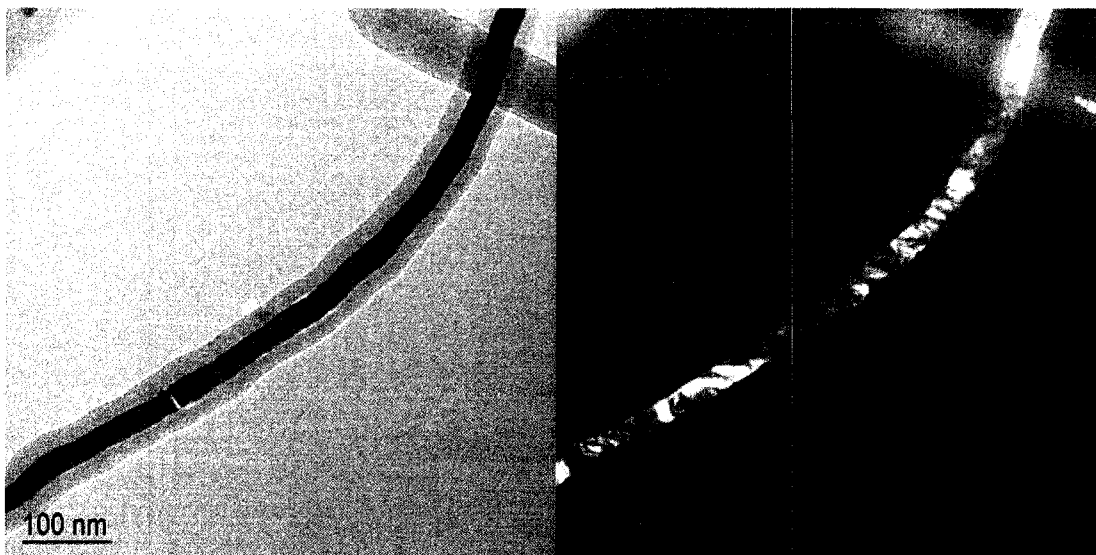


Figure 26. Low resolution TEM images of Si nanowires grown on copper TEM grid. [Bright field imaging on left and dark field image on right).

The SiNWs synthesized on Cu surface exhibited bimodal distribution in diameters; small wires with diameter of  $62 \pm 15 \text{ nm}$  and the larger ones with diameter of  $125 \pm 23 \text{ nm}$ . From the TEM image in Figure 25, the SiNWs synthesized on Cu surface has an amorphous oxide sheath  $19 \text{ nm}$  and a Si core (shown by the darker intensity diffraction) of  $36 \text{ nm}$ . The thicker oxide was probably due to reaction of Si with the copper oxide on the surface.

#### 3.5.2.2. SiNWs on silicate glass



Figure 27. SEM images of Si nanowires grown on silicate glass substrate.

The SiNWs synthesized on silicate glass also exhibited bimodal diameter distributions, as observed in copper case. The smaller wire has diameter of  $58 \pm 10$  nm and larger has diameter of  $104 \pm 17$  nm .

### 3.5.2.3. SiNWs on aluminium

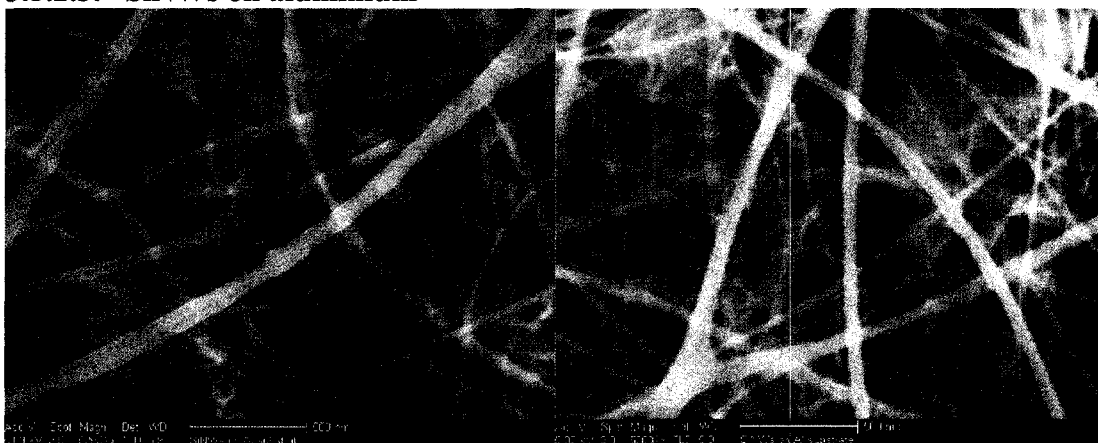


Figure 28. SEM images of Si nanowires grown on aluminized substrate.

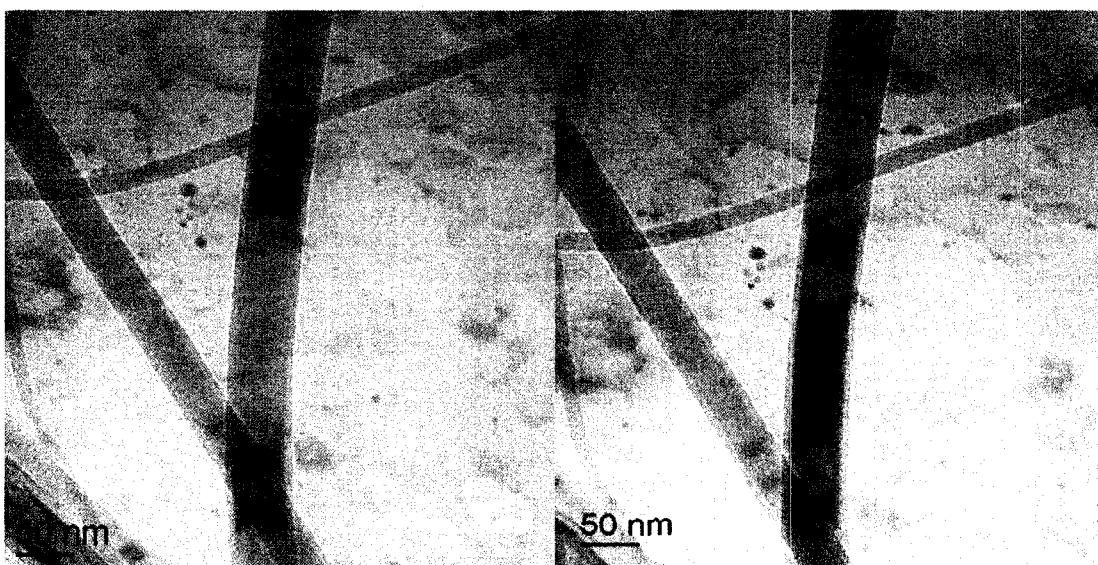


Figure 29. TEM images of Si nanowires grown on aluminized substrate.

In Figure 29 a TEM image of SiNWs synthesized on Al surface, the wires have a thinner oxide sheath of 6 nm. While tilting the wire, a shift in the dark band was observed that was caused by the electron beam hitting the SiNWs at a different plane.

The diameters of the SiNWs synthesized on different substrates were summarized in Table 6.

### 3.5.3. Summary of SiNWs diameter synthesized on different substrates

Substrates	mole DPS ( $\mu\text{mols}$ )	Reaction temp. ( $^{\circ}\text{C}$ )	Reaction time (min)	SiNWs diameter (nm)	
				(smaller)	(bigger)
Silicate glass	81	460	25	$58 \pm 10$	$104 \pm 17$
Cu	81	460	25	$62 \pm 15$	$125 \pm 23$
Si	81	460	25	$38 \pm 16$	NA
Al	81	460	25	$67 \pm 23$	NA

Table 6. Summary of SiNWs diameter synthesized on different substrates

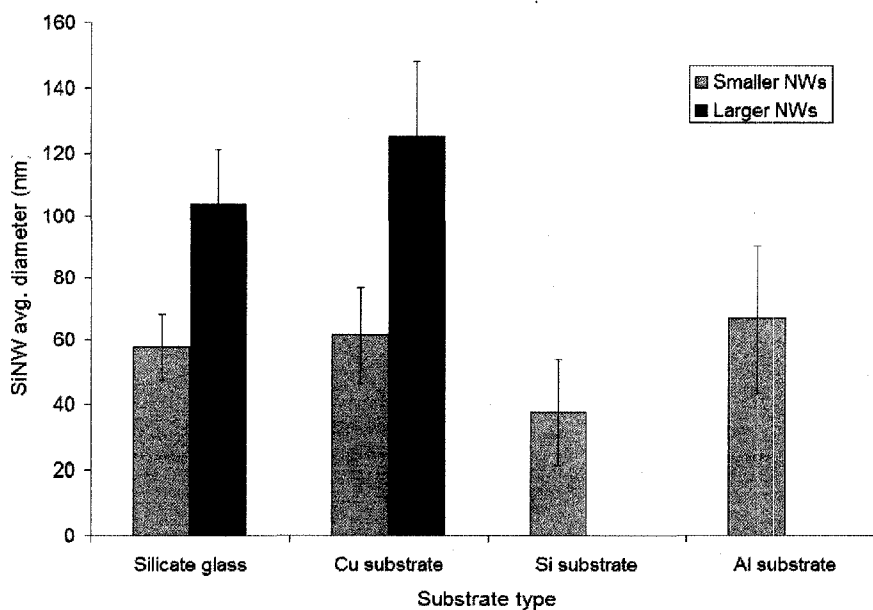


Figure 30. Average diameter of SiNWs on different substrates.

The bimodal distribution observed when Cu and silicate glass substrate might be due to use of a single chamber glass vessel. Within the uncertainties of diameter measurement the size of smaller diameter SiNWs are constant, perhaps controlled only by the DPS concentration as discussed previously.

Diameter of these NWs is almost a factor of 10 larger than the gold nanoparticles used in the synthesis. Several SEM images of gold catalyst at tip of SiNW, shown in Figure 25, indicate the size of the eutectic drop on top of growing SiNW was much greater than NW diameter. This observation suggests high mobility of gold nanoparticles on the substrates which leads to significant rise in diameter due to fusion of eutectic particles before SiNWs growth begins.

### **3.6. Bulk synthesis of SiNWs**

Initial attempt of synthesizing bulk SiNWs via supercritical VLS mechanism failed due to large dead volume in the system, extraction difficulty, premature decomposition of solvent and system break down due to extreme high pressure and temperature. Therefore, bulk synthesis of SiNWs via VLS mechanism in an enclosed glass vessel was attempted. The previous section 3.5 showed that, SiNWs could be grown on various substrates. Here a simple strategy of choosing a sacrificial substrate that acts as a growth template for SiNWs was followed. Post synthesis selective etching of the substrate could release perfectly intact bulk SiNWs. Four substrates were used as templates for SiNWs: aluminized-silicon substrate, glass fiber, aluminium oxide ( $\text{Al}_2\text{O}_3$ ) and calcium carbonate ( $\text{CaCO}_3$ ).

#### **3.6.1. Aluminized silicon template**

An aluminized silicon substrate (40 nm aluminium on 200 nm silicon oxide,  $\sim 1.2 \times 0.5$  cm) was used as template for synthesis of SiNWs. The synthesis procedure used is described in Section 3.5.1. After synthesis of SiNWs the underlying aluminium

was etched away by 0.07 M NaOH at 43 °C. Figure 31 shows the receding aluminium template layer exposing the underlying oxide and silicon nanowire.

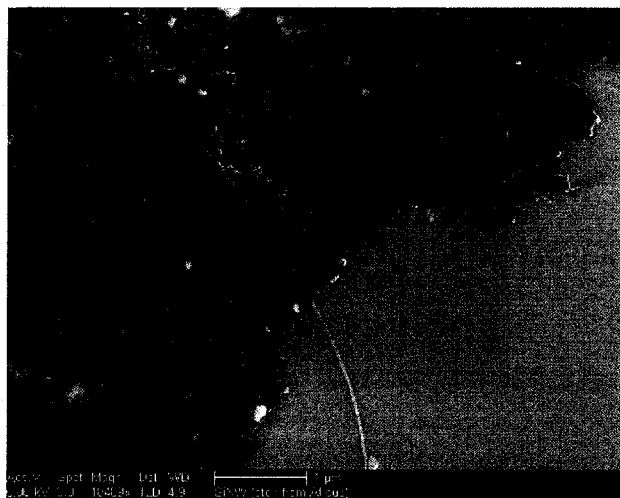


Figure 31. SEM images of partially etched aluminium layer exposing the underlying oxide.

### 3.6.2. Glass fiber template

A bundle of glass fibers ( $\approx 100 \mu\text{m}$  OD) was gathered and soaked in a tube consisting of  $28 \mu\text{M}$  diol-Au (in DMF) solution then baked to dry at  $100^\circ\text{C}$ .  $20 \mu\text{L}$  of DPS was used. The reaction was carried out at  $450^\circ\text{C}$  for 2 hours.

After synthesis, the silicate fiber was etched with aqueous ammonium bifluoride ( $\text{NH}_4\text{F} \cdot \text{HF}$ ).  $\text{NH}_4\text{F} \cdot \text{HF}$  has tendency to selectively etch  $\text{SiO}_x$  and not Si. Once the white flakes of  $\text{NH}_4\text{F} \cdot \text{HF}$  are dissolved in water, volatile and toxic hydrofluoric acid is generated. Appropriate rubber gloves, protective gowns and face shield were worn. The etch-rate of  $\text{NH}_4\text{F} \cdot \text{HF}$  on glass fiber was first studied.

### 3.6.2.1. Results

Silicon nanowires generated on glass fiber are shown in Figure 32. As before we observed growth primarily parallel to surface and not perpendicular to it as is commonly the case for SiNW grown in CVD flow reactors.

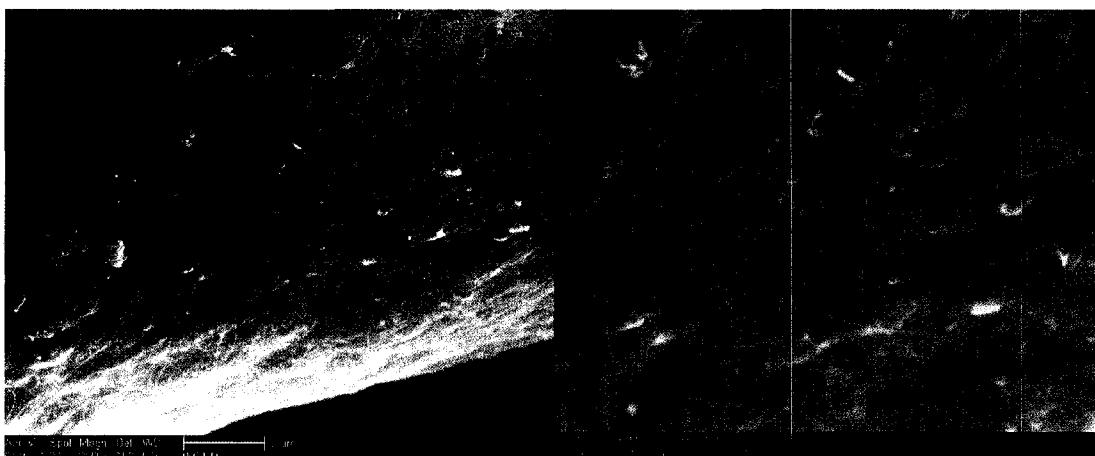


Figure 32. SEM images of Si nanowires grown on glass fiber substrate

Etch-rate study was performed by preparing a sequence of concentration of  $\text{NH}_4\text{F}.\text{HF}$  solutions and determining the time required to etch a known mass of silicate fiber. Etching of silicate fiber was performed in polypropylene (Fisher brand) tubes only.

Conc $\text{NH}_4\text{F}.\text{HF}$ (Molar)	Mass of silicate fiber (g)	Etch time (sec)	Etch rate g/sec
0.20 (1%)	$0.0030 \pm 0.0003$	2150	$1.40\text{E-}06$
0.61 (3.5%)	$0.0044 \pm 0.0002$	718	$6.13\text{E-}06$
0.89 (5%)	$0.0045 \pm 0.0002$	447	$1.00\text{E-}05$
1.22 (7%)	$0.0057 \pm 0.0002$	373	$1.53\text{E-}05$
1.57 (9%)	$0.0060 \pm 0.0002$	240	$2.50\text{E-}05$

Table 7. Concentration dependent of etch rate of  $\text{NH}_4\text{F}.\text{HF}$  on fiber glass.

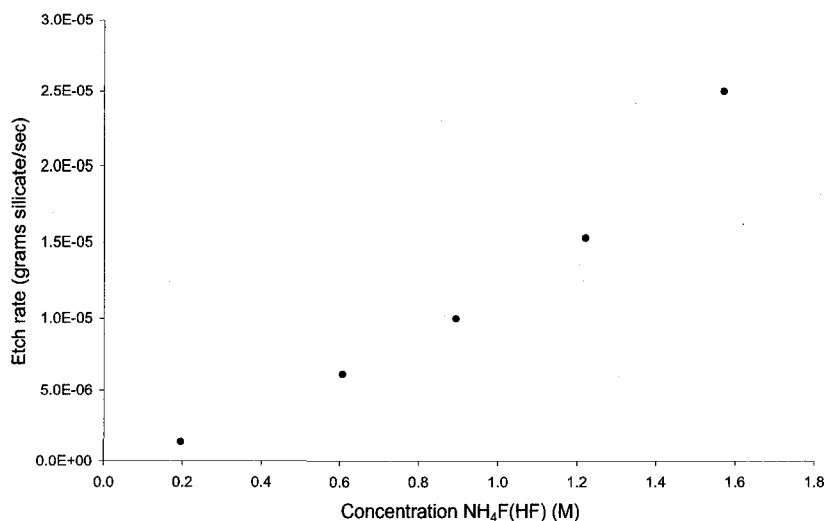


Figure 33. Plot of etch rate (grams of silicate/sec) versus concentration of  $\text{NH}_4\text{F}(\text{HF})$  in  $\text{H}_2\text{O}$ .

The bundle of silicate fibers with SiNWs were etched with 7-9%  $\text{NH}_4\text{F}(\text{HF})$  solution. Once all silicate fibers were etched away, 0.75 M NaOH was gradually pipetted to neutralize the HF acid. Removal of ionic salts was performed by a washing and a centrifuge cycle. SiNWs were centrifuged to the bottom allowing the ionic solutions to be pipetted away. This was followed with a water wash and additional centrifuging.

### 3.6.3. Aluminium oxide (alumina) template

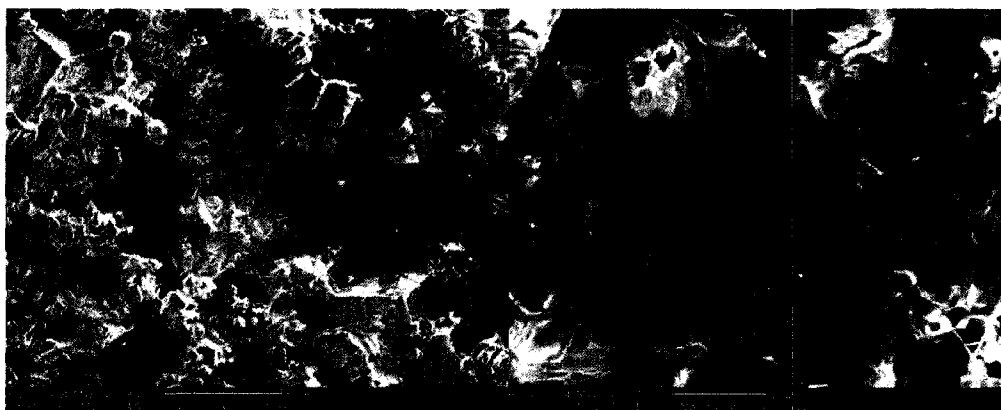
6  $\mu\text{L}$  of 28  $\mu\text{M}$  diol- $\text{Au}^0$  were pipetted on to a small pinch of alumina on a watch glass followed by mixing. The mixture was heated to evaporate DMF. The remaining powder was packed on to a silicon substrate. Loose and excess powder was tapped away. 7  $\mu\text{L}$  of DPS was pipetted into two glass tubes one containing silicon substrate packed with Au-alumina powder while the other tube only contained loose Au-alumina powder. The reaction was carried out at 515  $^\circ\text{C}$  for 25 min.





### 3.6.4. Calcium carbonate template

Sufficient amount of 28  $\mu\text{M}$  diol- $\text{Au}^0$  was pipetted on a pinch of  $\text{CaCO}_3$  (white powder) on a watch glass followed by mixing. The powder solution was pipetted on to a silicon substrate followed by heating to evaporate away the DMF. The remaining mixture on the watch glass was heated to evaporate away DMF. A volume of 15  $\mu\text{L}$  of DPS was pipetted into two glass tubes. The silicon substrate with  $\text{CaCO}_3$  powder was inserted into one glass tube. Gold coated  $\text{CaCO}_3$  powder was scooped into the second glass tube. Reaction was carried out at 450  $^\circ\text{C}$  for 60 min.  $\text{CaCO}_3$  can be etched away with dilute  $\text{HCl}$  acid after reaction.



(a.)



(b.)

Figure 35. SEM images of SiNWs on  $\text{CaCO}_3$ . Reaction carried out on: a.)  $\text{CaCO}_3$  deposited on Si substrate; and b.)  $\text{CaCO}_3$  powder.

### 3.6.5. Summary of SiNWs diameter on different templates

Template material	moles DPS ( $\mu\text{mols}$ )	Reaction temp. ( $^{\circ}\text{C}$ )	Reaction time (min)	SiNWs diameter (nm)
Aluminium	81	460	25	$67 \pm 23$
Fiber glass	108	450	60	$26 \pm 8$
Aluminium oxide	37	515	25	$27 \pm 4$
Calcium Carbonate	81	450	60	$32 \pm 8$

Table 8. SiNWs diameter synthesized on different templating materials prior to etching (data extrapolated from SEM images).

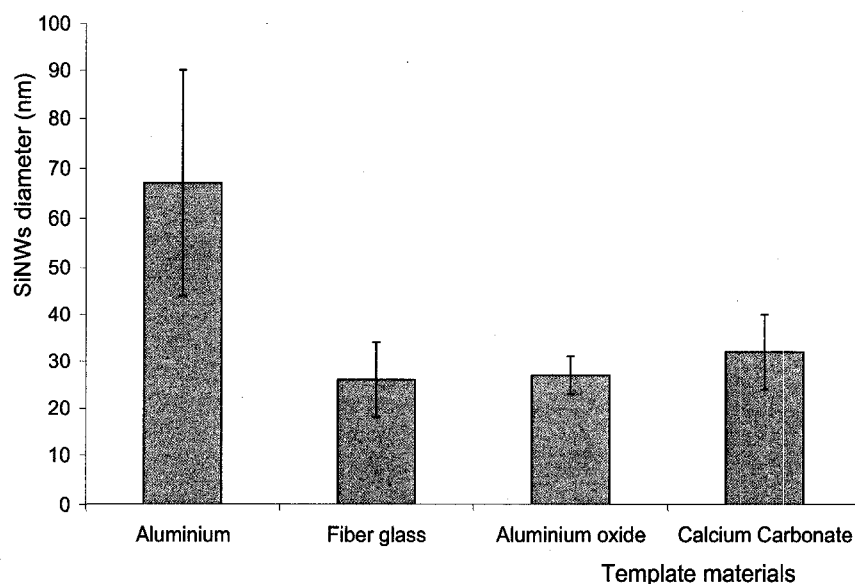


Figure 36. SiNWs diameter synthesized on different templating materials prior to etching.

### Conclusion

It was possible to synthesize bulk scale of SiNWs on an etch friendly powdered surfaces.

### **3.7. Synthesis of SiNWs using aluminium as catalyst via closed CVD technique in glass vessel**

Many metallic catalysts have been examined in synthesis of SiNWs. An appropriate metal catalyst, reaction temperature and reagent concentration for synthesis of SiNWs can be determined by the binary phase diagram of the chosen metal-Si pair. This sets the minimum reaction temperature and concentration for the synthesis of SiNWs. Apart from the most frequently cited gold and iron catalyst, metals such as titanium<sup>70,71</sup> (Ti), gallium<sup>72,73</sup> (Ga), and aluminium<sup>74</sup> (Al) have been reported as catalysts for the synthesis of SiNWs. SiNW formed by Au and Fe catalyst particles appears to grow by the VLS mechanism in which the synthesis is carried out at temperatures above the eutectic point. However, in some metal catalyst the SiNW has been observed to grow at a reaction temperature below the eutectic point. This mechanism is attributed to vapor-solid-solid (VSS) phase interaction, which will be discussed briefly.

Kamins et al<sup>70,71</sup> have first reported synthesis and formation of SiNW using Ti as catalyst via CVD. The synthesis temperature was carried out between 640-670 °C even though the lowest liquid eutectic of the equilibrium phase diagram for Ti and Si occurs at 1330 °C at a ratio by weight percentage of 75% Si to 25% Ti. The phase diagram can be seen in Figure 37. Even if the eutectic temperature is reduced due to small particle size, it is unlikely to reduce to the 600 °C range. At 600 °C range the Ti-Si alloy (TiSi<sub>2</sub>) catalyst form is as solid, not a liquid. The mechanism of SiNW formation initiates from silane decomposing to Si atoms in the vapor phase at an

elevated temperature, diffuses across  $\text{TiSi}_2$  solid nanoparticles and finally precipitating at the growing nanowire. This is known as VSS mechanism. VSS is different from VLS by having reaction temperature below the eutectic of the metal-Si and the catalyst alloy is in the solid state. Diffusion of Si across the solid particle is dramatically different than diffusion across a liquid particle. The diffusion coefficient is an order of magnitude higher across the liquid than the solid phase. At such elevated temperature the rate of Si decomposition is higher than rate of Si diffusion across the  $\text{TiSi}_2$  particles. Due to this difference the wires formed appear to be tapered mainly resulting from continuous deposition of Si along the sidewall of the nanowires.

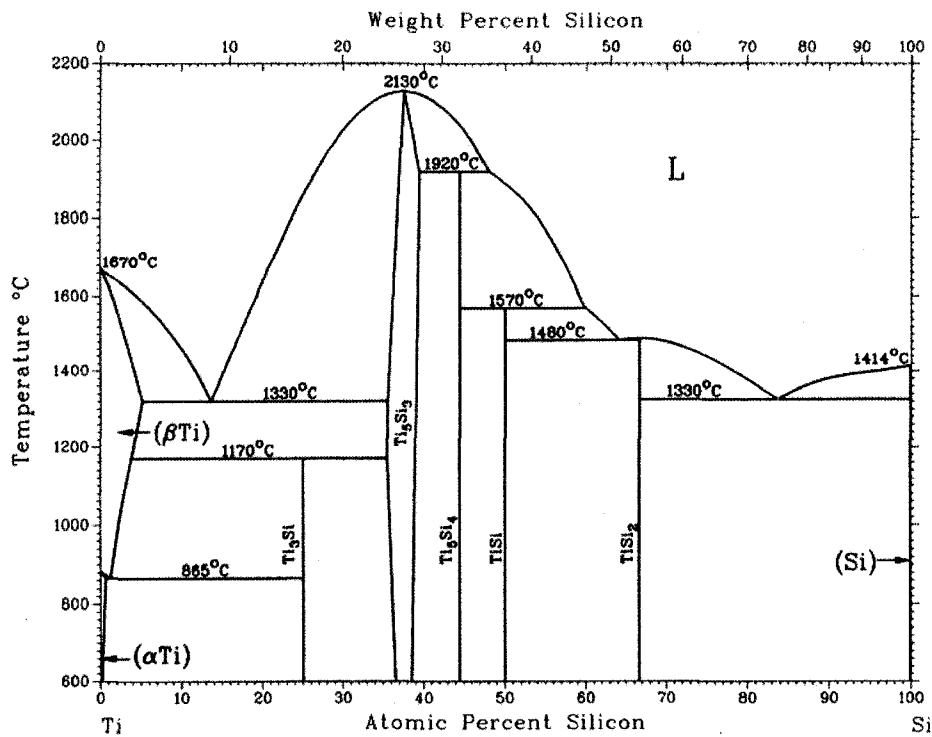


Figure 37. Binary phase diagram of Ti and Si<sup>75</sup>.

Wang et al<sup>74</sup> were the first to reported the synthesis of SiNW using Al as catalyst via VSS mechanism. Al and Si have a eutectic temperature at 577 °C (at a

ratio by weight percentage of 12.2% Si to 87.8% Al) as observed in Figure 38. Synthesis was carried out from 430 to 490 °C. SiNWs synthesized at 490 °C exhibit tapering, due to similar rational as for Ti-catalyzed studies. The tapering is reduced as reaction temperature is reduced. Uniform diameter SiNW was obtained at a reaction temperature of 430 °C. The experiment carried out at 530 °C exhibits a strong p-doping of Si by Al of about  $2 \times 10^{18} \text{ cm}^{-3}$  (0.004%).

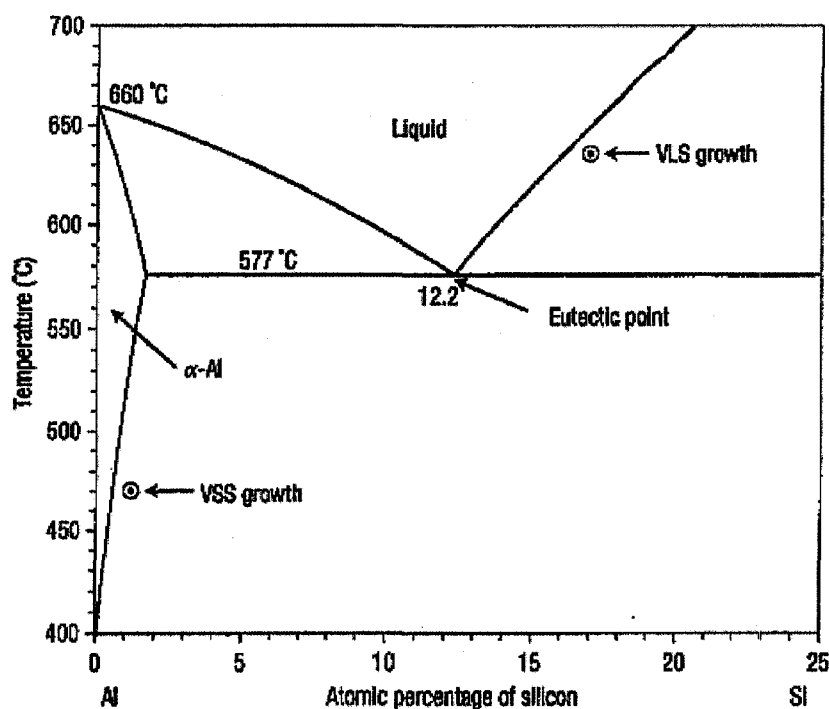


Figure 38. Binary phase diagram of Al-rich region of Al and Si<sup>74</sup>. (VLS and VSS are indicated for arbitrarily chosen temperatures)

Here we demonstrate the synthesis of SiNW using Al as catalyst via glass tube method. The SiNWs were analyzed using SEM and compared to the results obtained by Wang et al. Apart from using Al, antimony was found to be a good catalyst for synthesis of SiNW.

### **3.7.1. Procedure**

#### **3.7.1.1. Aluminium as catalyst**

A 200 Å of Al was evaporated on 1000 Å of SiO<sub>2</sub> (on a p-doped Si wafer). A small piece of the aluminized silicon substrate (1.5x0.7 cm) was partially etched in a N<sub>2</sub> purged glovebox (O<sub>2</sub> level ~0.9%) by 0.15 M NaOH. Next, 5 µL of DPS was pipetted into a glass tube (duo chamber was fabricated). The Al substrate was inserted and the tube was evacuated to 60 mTorr before sealing. The reaction was carried out at 500 °C for 90 min. SEM and TEM (FEI Tecnai F-20) were used to analyze the SiNWs (Figure 39 and 40).

#### **3.7.1.2. Antimony as catalyst**

Antimony particles were prepared using antimony(III) chloride (SbCl<sub>3</sub>). The SbCl<sub>3</sub> was dissolved in DMF to a concentration of 0.157 M. The 0.157 M SbCl<sub>3</sub> (in DMF) was pipetted in 2.9 M 1,8-octanediol solution in DMF. The resulting concentration of Sb<sup>3+</sup> was 0.005 M. Since SbCl<sub>3</sub> can be easily hydrolyzed by water to insoluble Sb(OH)<sub>3</sub>, a pinch of the reducing agent NaBH<sub>4</sub> was directly added to SbCl<sub>3</sub> solution. The solution gradually turned brownish then dark. The final concentration of Sb<sup>0</sup>-diol catalyst was 0.005 M.

The conditions of the reaction were as follows: 15 µL of the Sb<sup>0</sup>-diol; 5µL of DPS; and reaction time of 60 min. Three reaction temperatures were studied (450, 500 and 550 °C).

### 3.7.2. Results

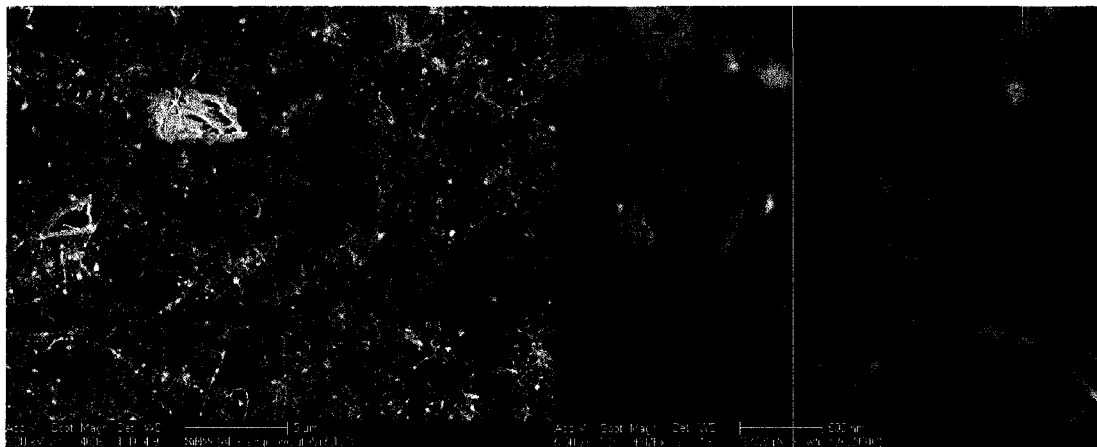


Figure 39. SEM images of SiNWs synthesized using Al as catalyst.

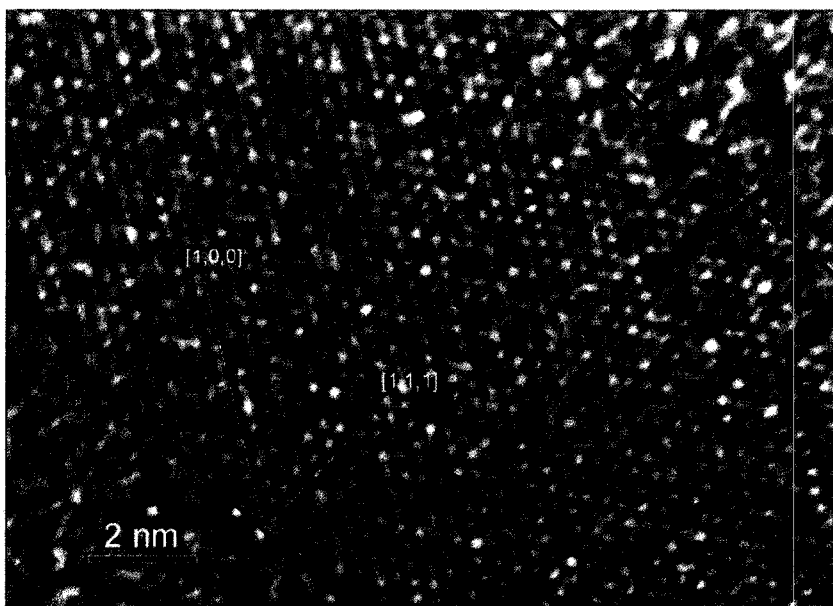


Figure 40. TEM images of SiNWs synthesized using Al as catalyst.



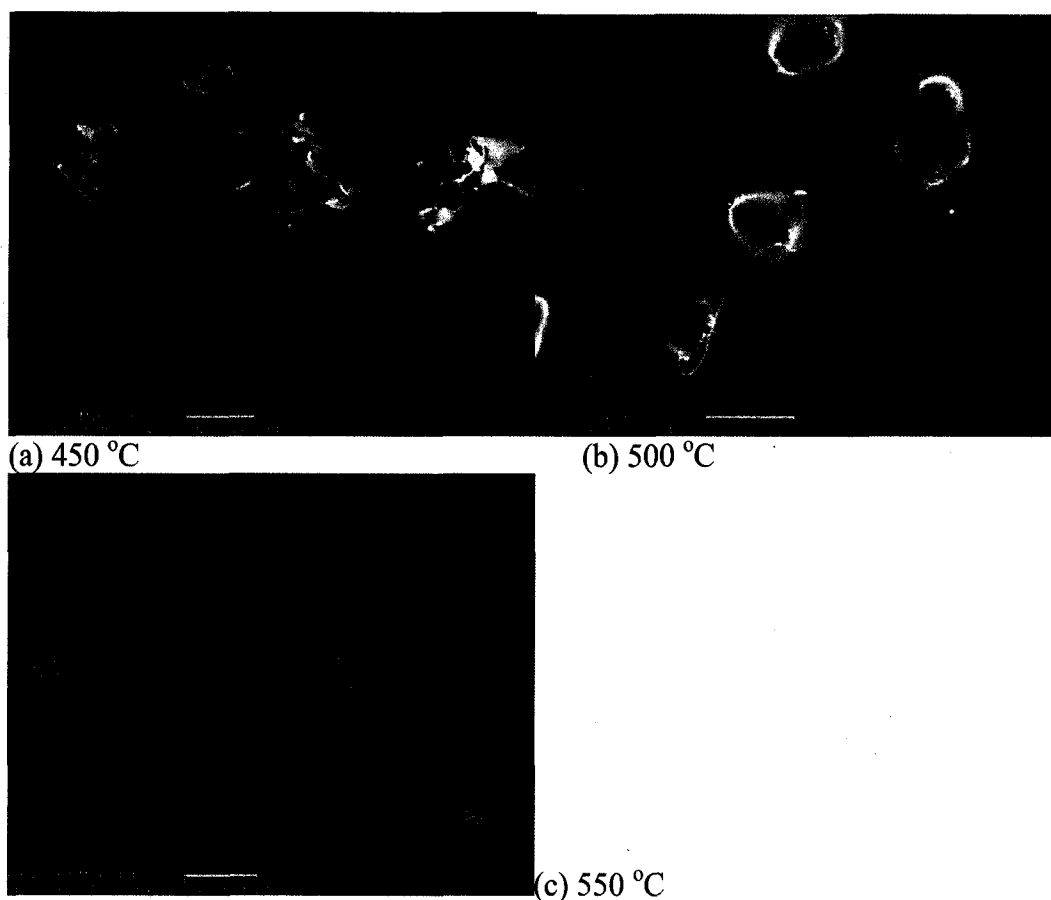


Figure 41. SEM images of SiNWs synthesized using Sb as catalyst at: (a) 450 °C; (b) 500 °C; and (c) 550 °C.

The Al catalyzed SiNW is single crystalline with growth direction in the [1,1,1] plane. The SiNWs have a sheath of oxide approximately 5-6 nm surrounding the crystalline wire of diameter 12 nm. Diameters of the Al and Sb catalyzed SiNWs are tabulated in Table 9.

### 3.8. Doping of SiNWs using organometallic precursors

SiNW doping is routinely carried out *in situ*, in a CVD reactor or enclosed chamber, by flowing highly toxic gases such as diborane<sup>76,77,78</sup>, phosphine<sup>79,80</sup>, arsine, etc., via mass flow regulators that control the precise flow rate, thus the concentration of the dopants. The overall cost of hazards and handling toxic gases are large obstacles

for the synthesis of doped-SiNW, and this method is considered a “non-green” approach in doping the SiNW. This work will demonstrate a low cost and “green” method for synthesizing and doping of SiNW in a glass tube.

The advantage of the glass tube synthesis method is that clean doping is possible by either selecting the appropriate metal catalyst as shown in section 3.7 with high solubility with Si at eutectic and/or selecting a dopant-containing organic precursor that is soluble with DPS. From the experiment carried out in previous section, synthesis of SiNWs using Al as catalyst, and report from Wang et al<sup>74</sup>, Al can be doped into SiNW rendering the wires p-type. Thus, Al is simultaneously a catalyst and a dopant for synthesis and doping of p-type SiNWs. In the following section, the use of a dopant-containing organic precursor that is soluble with DPS to synthesize doped SiNWs will be validated.

### **3.8.1. Procedure**

#### **3.8.1.1. Synthesis of p-type SiNW**

The dopant used is triphenylborane (TPB). TPB is highly soluble in DPS. Stock solution of 750 ppm of TPB in DPS was prepared by direct dissolving a stoichiometric amount of TPB to DPS. The synthesis conditions were as follow: 10 $\mu$ L of 28 $\mu$ M Au<sup>0</sup> nanoparticle solution; 4 $\mu$ L TPB/DPS; and reaction time of 60 min. Three reaction temperatures were studied (450, 500 and 600 °C). These samples were analyzed by SEM (Figure 42).

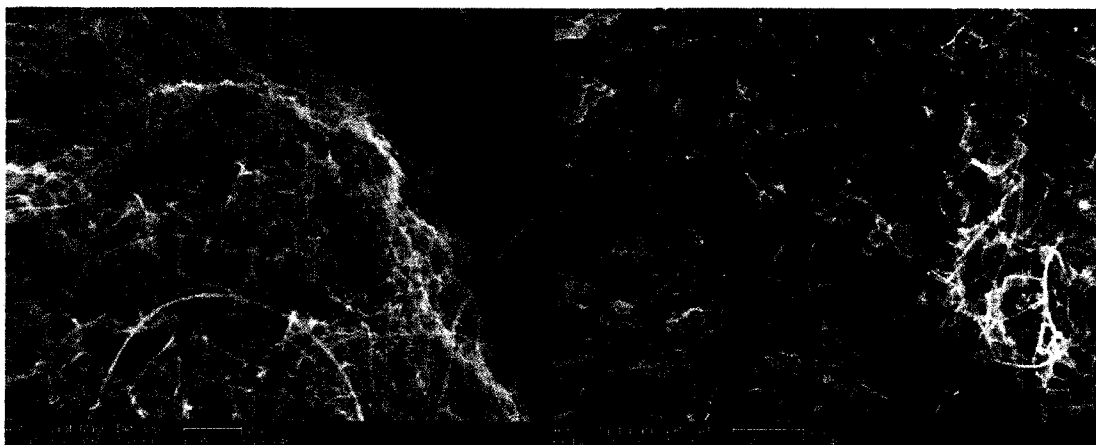
A fresh sample was prepared for TEM analysis by directly synthesizing p-type SiNWs on a copper TEM grid (Figure 43).

### 3.8.1.2. Synthesis of n-type SiNW

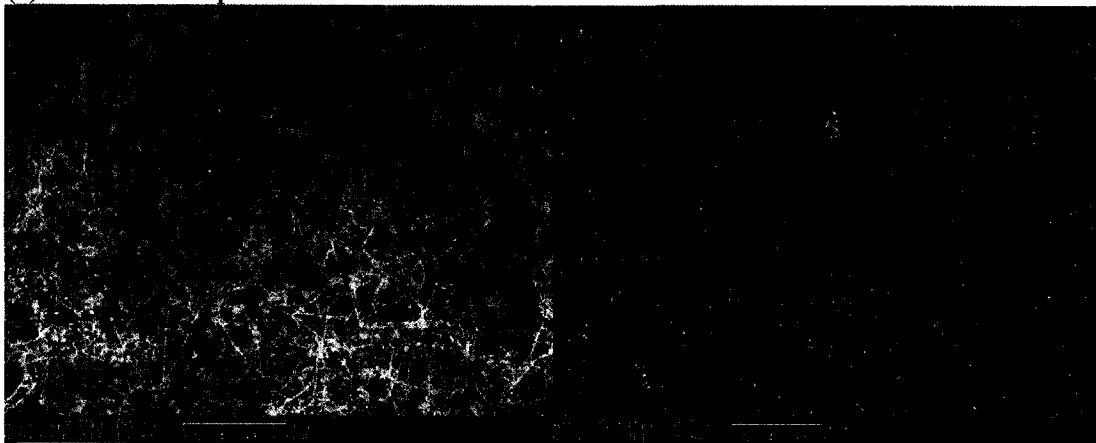
The dopants used were diphenyl phosphine (DPP) and triphenyl antimony (TPA). Stock solution of 440 ppm of TPA in DPS (moles to moles ratio) and 531 ppm of DPP in DPS were prepared. Both dopant compounds are soluble in DPS.

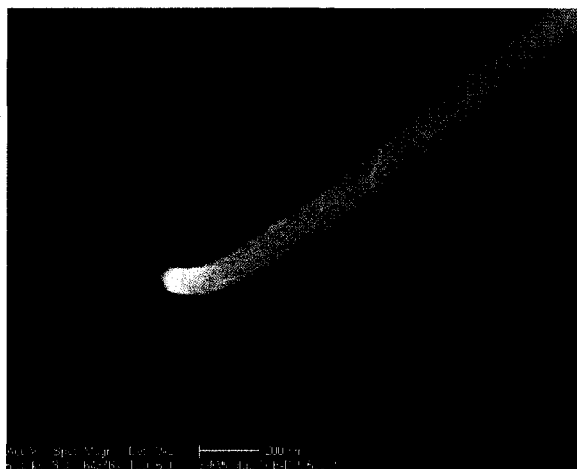
The synthesis conditions were as follow: 10  $\mu\text{L}$  of 28  $\mu\text{M}$   $\text{Au}^0$ -diol; 4  $\mu\text{L}$  of DPP/DPS or TPA/DPS; and reaction time of 60 min. Two reaction temperatures were studied (450 and 500  $^{\circ}\text{C}$ ). SEM analysis was performed on the samples (Figure 44 and 45).

### 3.8.2. Results

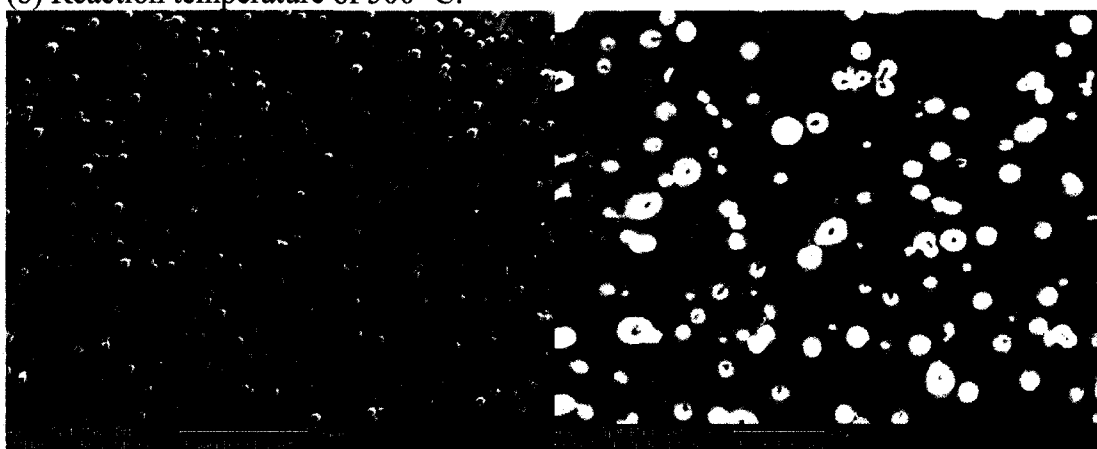


(a) Reaction temperature of 450  $^{\circ}\text{C}$ .





(b) Reaction temperature of 500 °C.



(c) Reaction temperature of 600 °C.

Figure 42. SEM images of boron-doped SiNWs carried out at (a) 450 °C, (b) 500 °C, and (c) 600 °C.

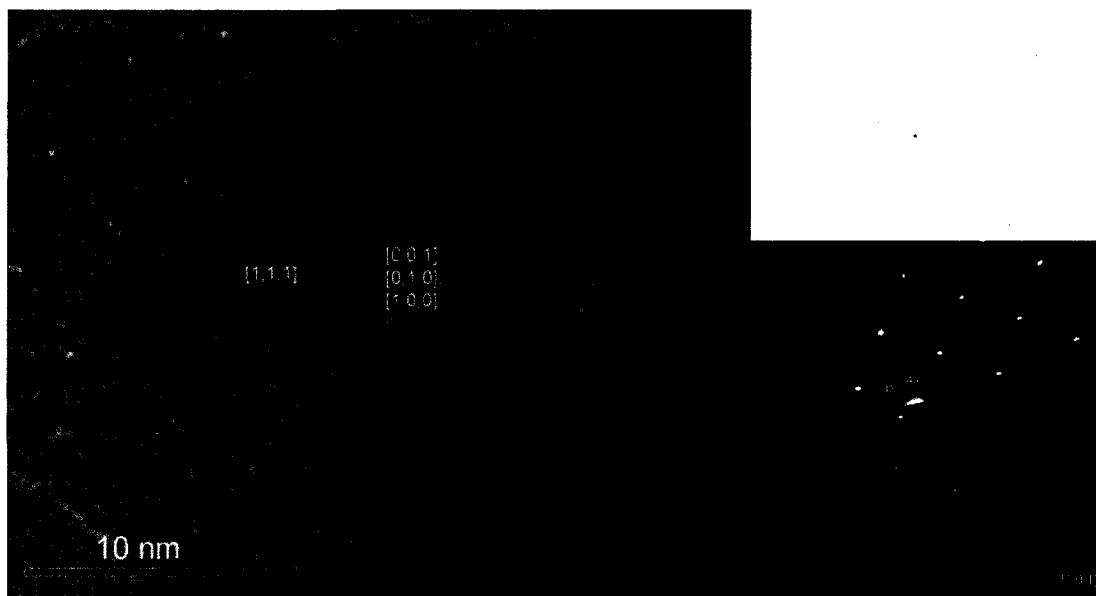


Figure 43. HRTEM image and corresponding diffraction pattern of boron-doped SiNW.

The boron doped SiNW is single crystalline as shown from the HRTEM lattice plane image and from the selected area diffraction pattern (Figure 43), with a growth direction in the  $[0,0,1]$  plane. The SiNWs have a sheath of oxide approximately 8-9 nm surrounding the crystalline wire of approximately 10 nm diameter.

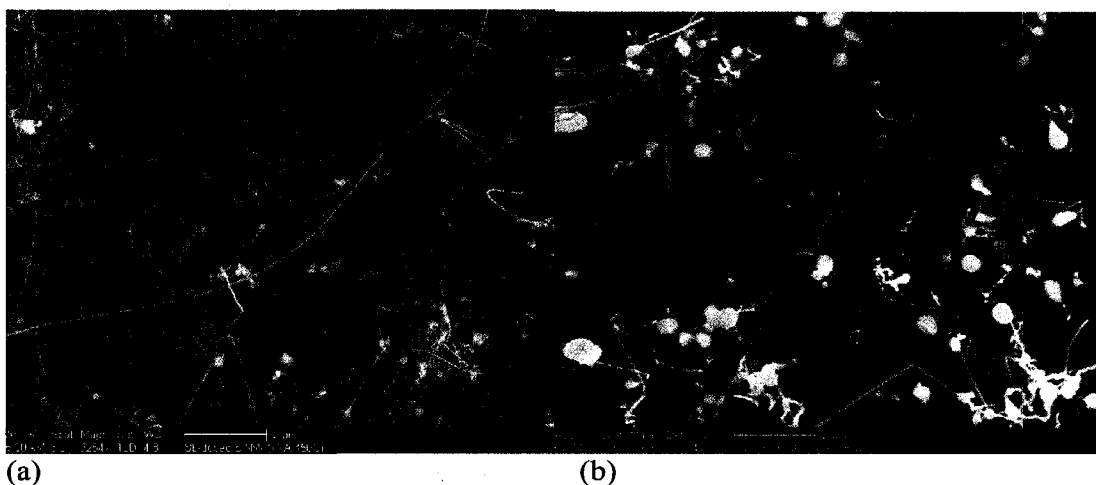


Figure 44. SEM image of antimony-doped SiNWs at (a) 450 and (b) 500 °C.

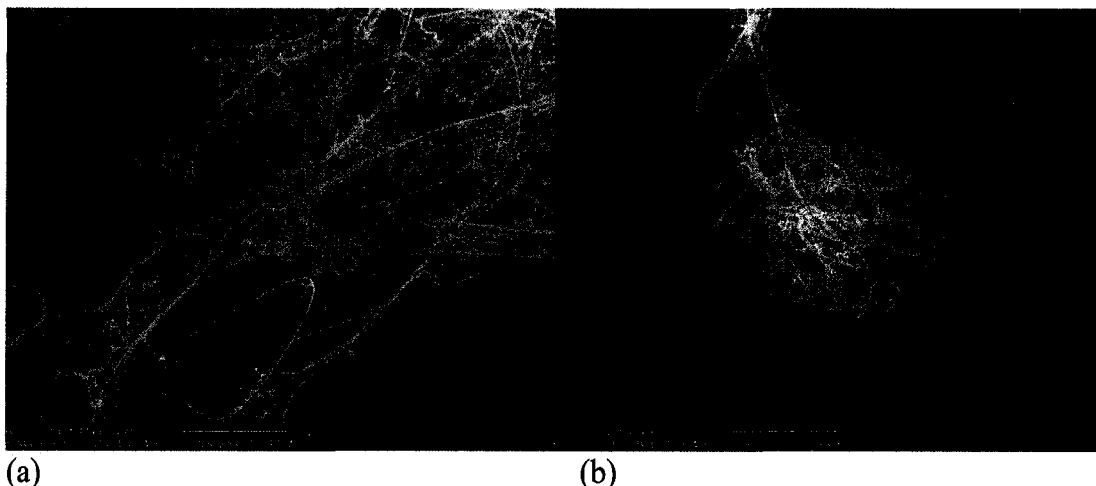


Figure 45. SEM image of phosphorus-doped SiNWs at (a) 450 and (b) 500 °C.

### 3.8.3. Discussion

The actual level of doping in these SiNWs is unknown due to limitation in instrumentation for quantification. EDX from both SEM and TEM, to detect trace amount of dopant, have been attempted but not successful. However, the SEM images observed for the sample with dopant containing precursor indicate that the structure of the wires have altered from the optimum case (Figure 19) using the duo chamber tube method. The dopant containing precursor wires have many kinks and bends. Furthermore, the diameters of the wires are larger than the undoped samples, with average of 77 nm and as large as 169 nm is observed. With similar synthesis conditions the SiNWs produced have variable diameters. From these collective observations it is safe to assume some level of extrinsic dopant in the Si lattice. More careful quantification is still needed to verify the presence of doping and the distribution of dopant atoms in the SiNW.

No.	Samples	# moles DPS ( $\mu$ moles)	Reaction temp. ( $^{\circ}$ C)	Reaction time (min)	Internal pressure (atm)	SiNW diameter (nm)
1	SiNW catalyzed by Al	27	500	109	0.26	46 $\pm$ 10
2	SiNW catalyzed by Sb	27	450	60	0.25	40 $\pm$ 12
3	SiNW catalyzed by Sb	27	500	60	0.26	42 $\pm$ 11
4	DPP (531 ppm)/DPS	22	450	60	0.20	169 $\pm$ 57
5	DPP (531 ppm)/DPS	22	500	60	0.21	148 $\pm$ 46
6	TPA (440 ppm)/DPS	22	450	60	0.20	33 $\pm$ 6
7	TPA (440 ppm)/DPS	22	500	60	0.21	54 $\pm$ 18
8	TPB (750 ppm)/DPS	22	450	60	0.20	57 $\pm$ 10
9	TPB (750 ppm)/DPS	22	505	60	0.21	102 $\pm$ 21

Table 9. Diameter of doped SiNWs.

Conductivity measurements<sup>24</sup> and ultra-high vacuum STM (room temperature) studies of p-doped silicon nanowires has been reported<sup>81</sup>. Rectangular and uniformly distributed domains on the silicon nanowires of several nanometers in size were observed under UHV STM which was suspected to be associated with the p-type dopant. Future studies involving UHV STM analysis will be an appropriate for monitoring the uniform distribution of the dopant in the SiNWs. Alternative methods of analyzing should include bulk doped SiNWs using inductive coupled plasma mass spectroscopy (ICPMS) and total reflection fluorescence spectroscopy (TRFS) have lower detection limits.

### 3.9. SiNW junctions

An important consequence of surface parallel growth is the possibility of collisions amongst growing liquid tips and the pregrown nanowires. This feature is believed to lead to metallurgical fused junctions shown in Figure 46 which has not been observed before.

Since the growth temperatures employed in these studies fall well below the melting points of either Si or  $\text{SiO}_x$  it is suspected that the junctions are created by colliding liquid catalyst droplet with preformed SiNW lying in its path. These single crystalline SiNWs are fused by either amorphous  $\text{SiO}_x$  or uncatalyzed Si due to a significant amount of  $\text{O}_2$  (lowest pressure achieved by the mechanical oil pump is  $\sim 70$  mTorr, thus partial pressure of  $\text{O}_2$  remaining in the tube is  $\approx 0.2 \times 70 \text{ mTorr} \approx 14 \text{ mTorr}$ ) and high amount of moles of Si in vapor (Table 4).

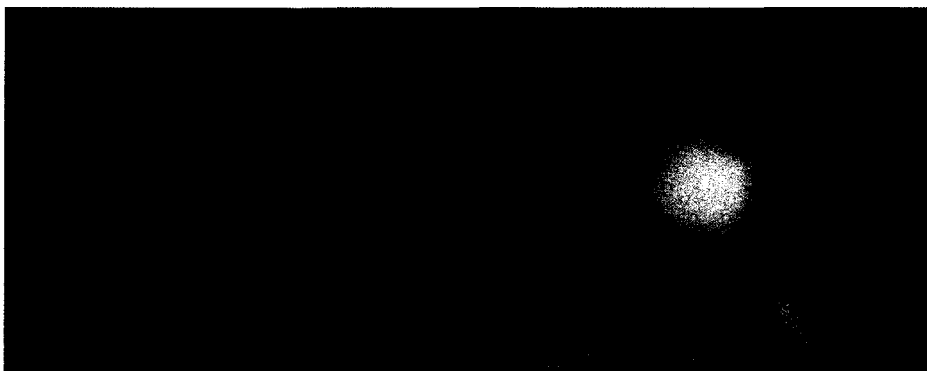


Figure 46. SEM images of cross junction structure observed with undoped (left) and boron-doped (right) SiNWs.

Figure 46 shows a HR TEM junction formed by two SiNWs. The top wire has lattice fringes along the  $[0,1,1]$  plane and bottom wires along the  $[1,1,0]$ . Both the planes have similar orientations. Due to this symmetry the junction is showing constructive fringes of the same orientation (Figure 47). The measured angle between



the wires is  $60^\circ$ . From Table F2 (Appendix F) the calculated angle between a  $[0,1,1]$  and  $[1,1,0]$  plane should be  $60^\circ$ .

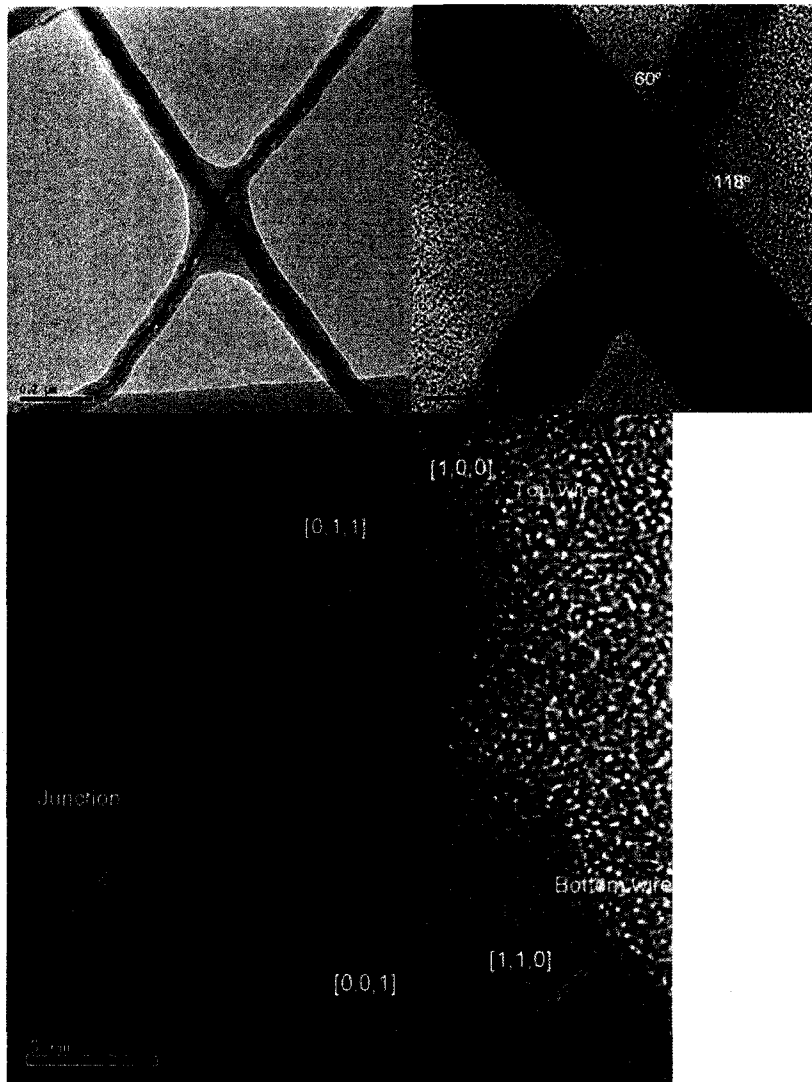


Figure 47. TEM image of an epitaxial SiNW junction.

In a second case of a junction illustrated in Figure 48, the vertical wire has  $[1,1,0]$  and horizontal  $[0,1,1]$  plane. The observed angle between the lattice planes is  $66^\circ$ , greater than the optimal angle between the lattice planes ( $60^\circ$ ). Overlapping fringes are observed at the junction. This non-epitaxial fusing of junction can give rise to high resistance from electron scattering.

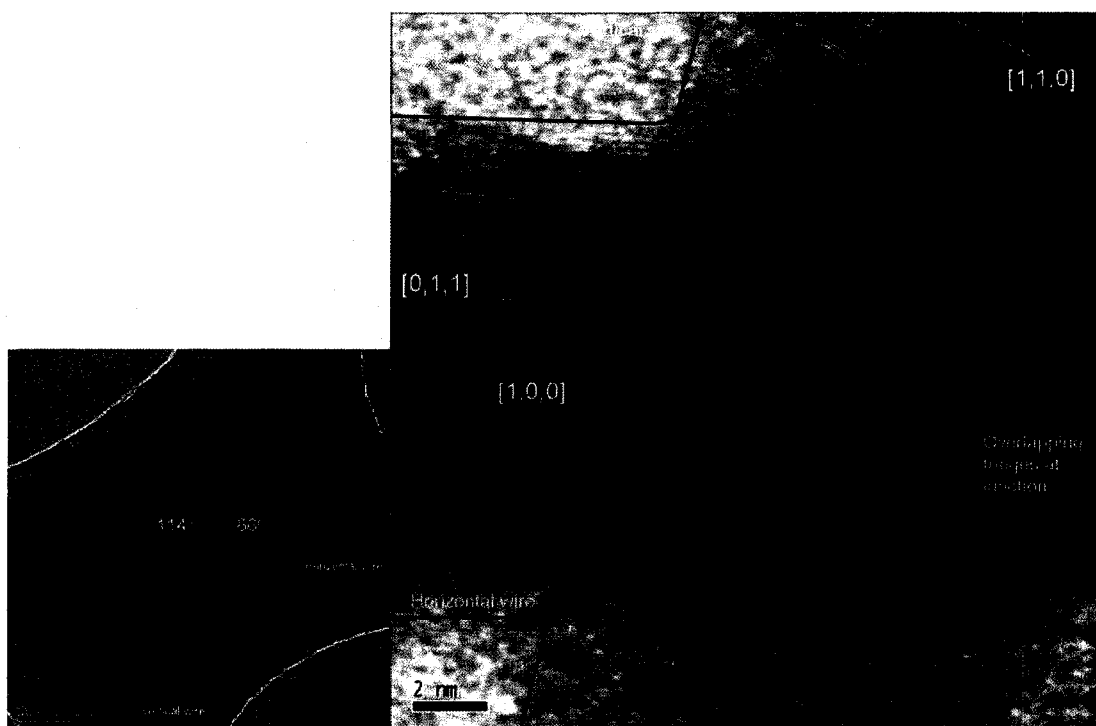


Figure 48. TEM image of a non-epitaxial SiNW junction.

In almost every instance where such junctions were observed, near perfect angles between the corresponding appropriate crystallographic planes were noted. To reduce the contact resistance at the junction, the criteria are that the two wires need to have matching lattice planes and the angle of the two wires coming in contact have to match the angle between the two lattice planes. This form of epitaxy will reduce electron scattering effect. More HRTEM images on the SiNWs and junctions are presented in Appendix F2.

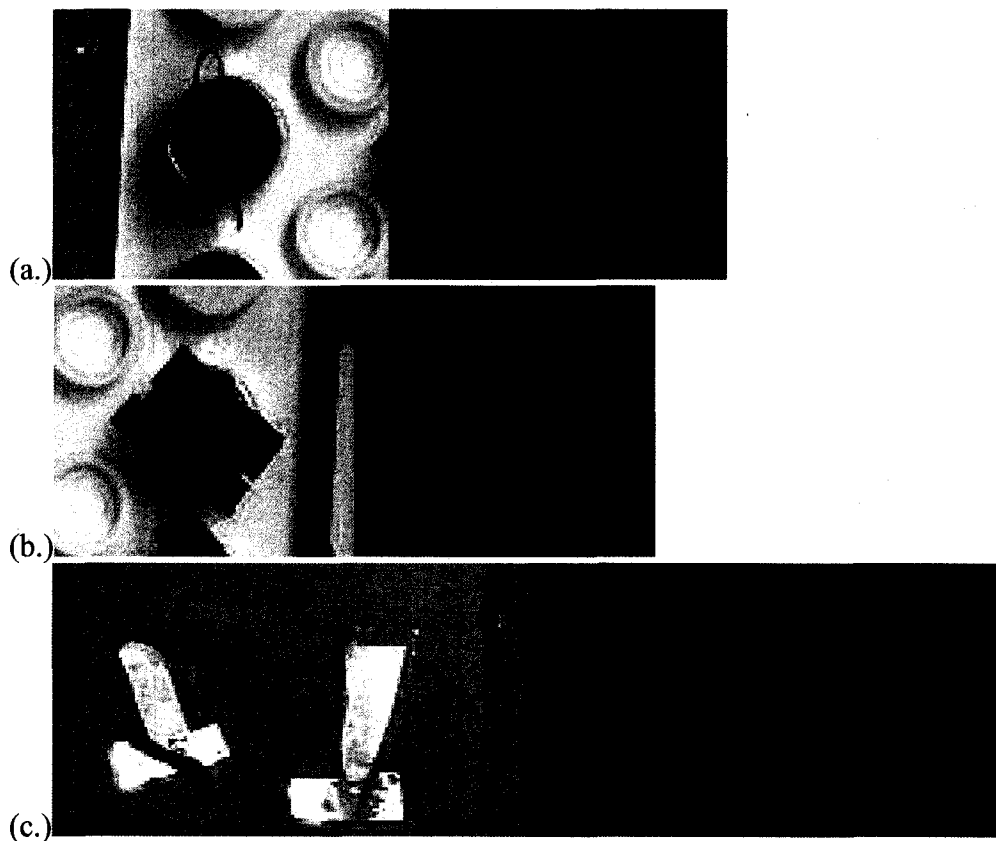
### 3.10. Fluorescence spectroscopy analysis

Fluorescence was observed in all the samples after synthesis under a low intensity 366 nm and 254 nm UV light. Traditionally, photoluminescence (PL) has been used to determine the bandgap for materials with direct bandgap. Due to lack of a PL spectrophotometer, the fluorometer was used to probe the emission of the SiNWs.

Four excitation wavelengths were chosen, 250, 271, 300, and 350 nm. The emission spectra at each excitation were obtained. The fluorescence spectra for the bare substrates were collected and a plot of  $\log\left(\frac{I}{I_o}\right)$  versus emission wavelength was obtained, where  $I$  is the emission spectra of the sample and  $I_o$  is the emission spectra of the bare substrate.

### 3.10.1. Results

Figure 49 illustrates the fluorescence of NWs on different substrates after the reaction. Sample on borosilicate glass also exhibits phosphorescence immediately after the UV (366 nm and 254 nm) light was switched off. The lifetime was only 4 sec as captured by a CCD digital camera.





(d.)

Figure 49. UV Photo-illumination of Si nanowires grown on a.) copper; b.) silicon; c.) and silicate glass. Phosphorescence (d.) observed for Si nanowires grown on silicate glass surface.

The fluorescence emission spectra for undoped SiNWs showed average peak maxima at 3.35 eV (370 nm), 3.37 eV (368 nm) and 2.92 eV (425 nm), corresponding to excitation at 250 nm, 271 nm and 300 nm, respectively. A complete table of emission data for undoped SiNWs is presented in Appendix G (Table G4). The fluorescence emission spectra for doped SiNWs showed average peak maxima at 3.04 eV (409 nm), 2.95 eV (420 nm) and 2.77 eV (448 nm), corresponding to excitation at 250 nm, 271 nm and 300 nm, respectively. The fluorescence emission spectra for Si sphere showed average emission at 2.84 eV (500 nm), 2.79 eV (444 nm) and 2.61 eV (475 nm), corresponding to excitation at 250 nm, 271 nm and 300 nm, respectively. The average emission energy for undoped SiNW, doped SiNW and Si sphere are presented in Appendix G (Table G1-G3). Figures 50–53 illustrates selective emission peaks for Si spheres with and without Au catalyst, and Al catalyzed SiNWs. Reaction carried out without Au catalyst will only have Si spheres. These samples are used to verify if fluorescence allows any significant resolution between doped and undoped SiNWs and Si spheres.

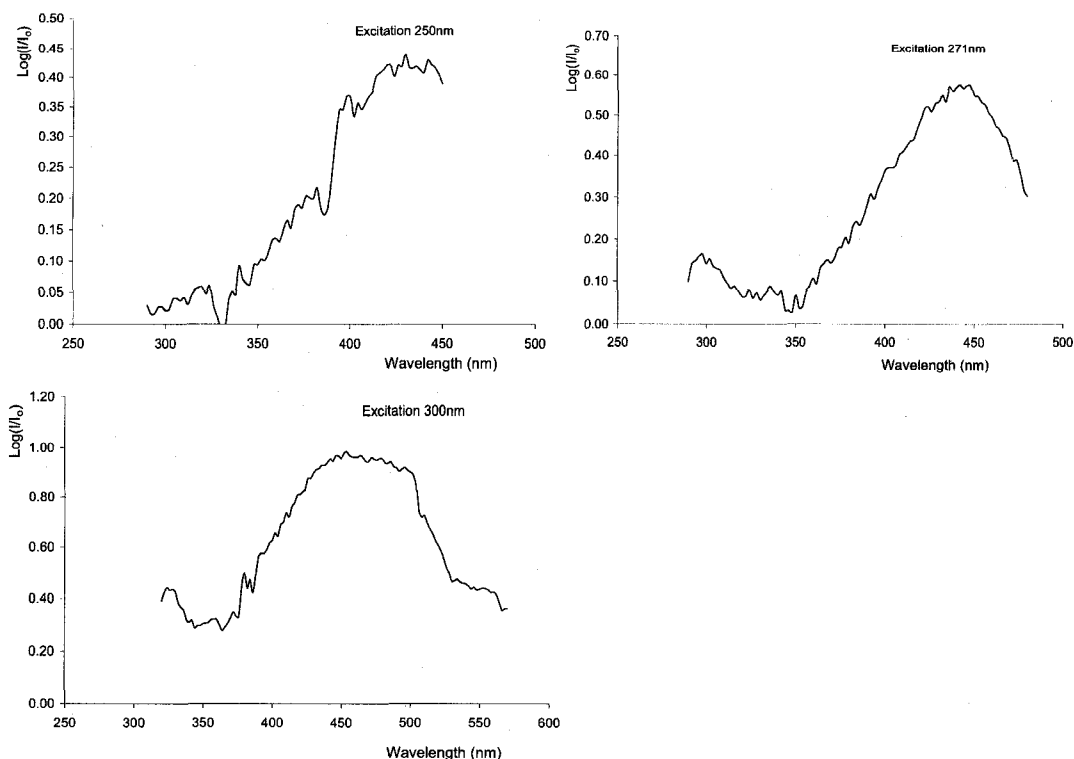


Figure 50. Fluorescence spectra of Si sphere on Si substrate (excitation wavelength at 250, 271 and 300 nm; reaction condition 550 °C; 30 min; without Au catalyst).

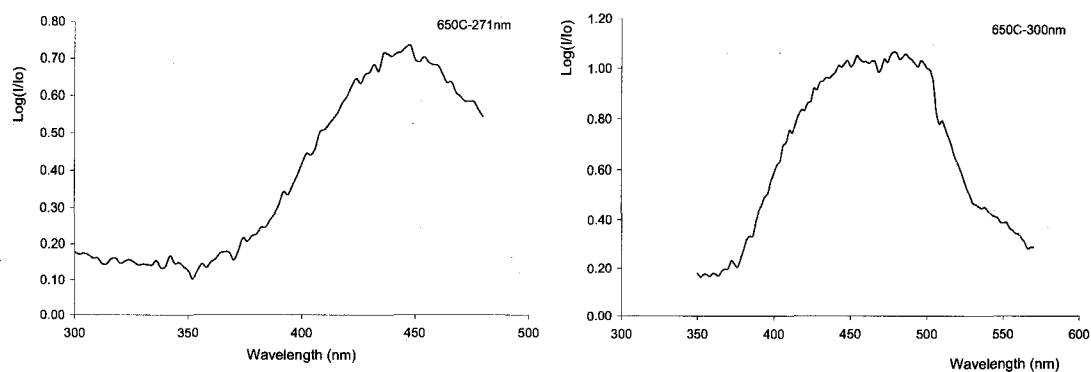


Figure 51. Fluorescence spectra of Si sphere on Si substrate (excitation wavelength at 271 and 300 nm; reaction condition 650 °C; 30 min; with Au catalyst).

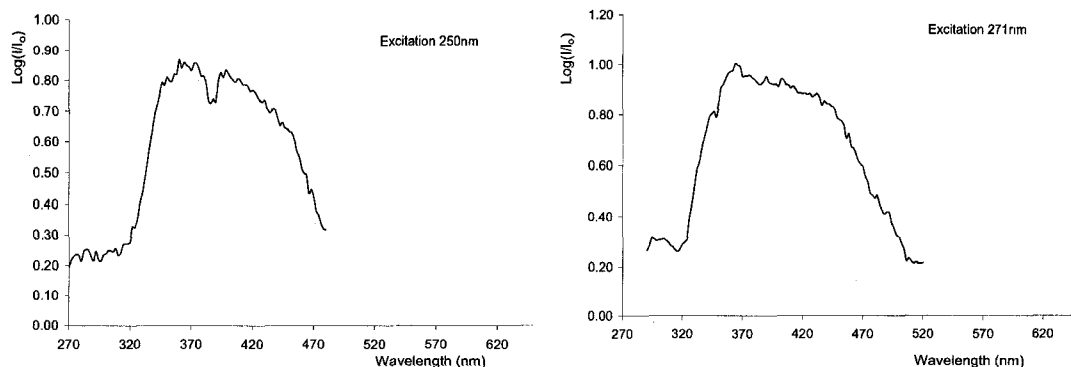


Figure 52. Fluorescence spectra of Au catalyzed SiNW on Si substrate (reaction condition: 500 °C; 60 min).

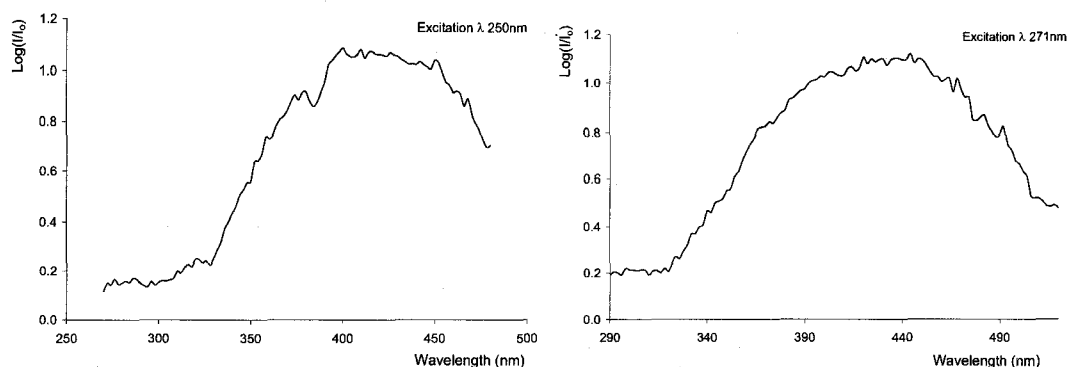


Figure 53. Fluorescence spectra of Al catalyzed SiNWs (reaction condition: 500 °C; 109 min).

Holmes et. al.<sup>82</sup> observed emission peaks at 420 nm (2.93 eV), 375 nm (3.3 eV), 355 nm (3.5 eV) and 310 nm (4.02 eV), from SiNWs of diameter of 7.3 nm, 5.0 nm, 4.5 nm, 3.0 nm and 2.2 nm, respectively. Based on the early calculation by Rama Krishna et. al.<sup>83</sup>, prediction of a direct band transition ( $\Gamma \rightarrow \Gamma$  of 3.4 eV) occurs when the radius Si cluster decreases to 2.5 nm (~5 nm diameter). Many reports have shown an emission peak in the 600-700 nm range corresponding to a bandgap of ~2.0 eV<sup>52,84</sup> for SiNWs of 2-3 nm. This peak was barely observed in the current studies presented here. The majority of the SiNWs synthesized have diameters larger than 20 nm, too large to be in the direct bandgap regime. Yet peaks at 3.35 eV and 2.92 eV were

observed. Initially it was hypothesized that this effect could arise from polycrystalline nanosized grains in these SiNWs. However, all the HR TEM images and diffraction patterns obtained the results show single crystalline SiNWs from wire to wire.

An alternate explanation based on the band energy diagram of bulk silicon as shown in Figure 54 is possible. The energy gap between the top of the valance band and the second lowest conduction band is about 3.4 eV as shown in Figure 54. Furthermore, momentum space location of these conduction bands falls directly on top of two highest valence bands. For nanoscale material it is conceivable that the transitions that are normally forbidden in bulk materials may become allowed. The selection rule is slightly relaxed at this regime. The other classical explanation<sup>85</sup> can be advocated on finite size effects on band gap. It would require silicon nanowires to be less 5 nm in diameter to explain the 355 nm emission peak. The origin of 468 nm peak has been ascribed to silicon rich oxides and silicon nanoparticles<sup>86</sup>.

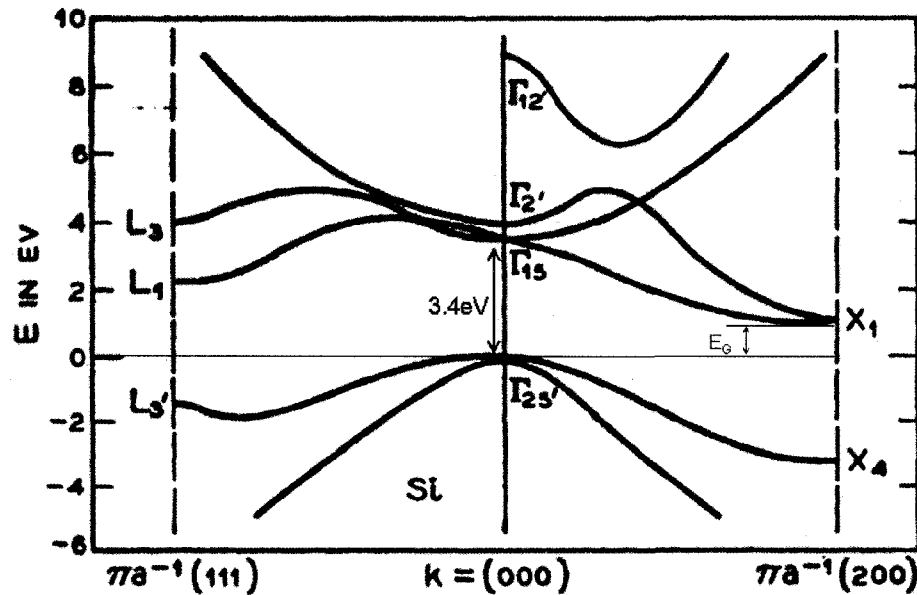


Figure 54. Band energy diagram of silicon<sup>87</sup>.

The fluorescence data for the doped wires samples, from section 3.8, were obtained at similar excitation wavelength. The results of undoped SiNW (full results for the undoped SiNW are presented in Appendix G Table G4), doped SiNW and Si sphere are tabulated in Table 10.

A boxplot summary of the complete undoped SiNW, doped SiNW and Si sphere fluorescence data is illustrated in Figure 55 for comparison. The lower quartile, median and upper quartile for the undoped SiNW data is 3.13, 3.47 and 3.53 eV, respectively. The right edge of the box is skewed much closer to the median. The lower quartile, median and upper quartile for the doped SiNW is 3.00, 3.03 and 3.13 eV, respectively. The left edge of the box is skewed much closer to the median.

The undoped SiNWs box spread encompass the direct band regime (3.4 eV) and its median lies closer then the undoped SiNW and Si sphere samples.

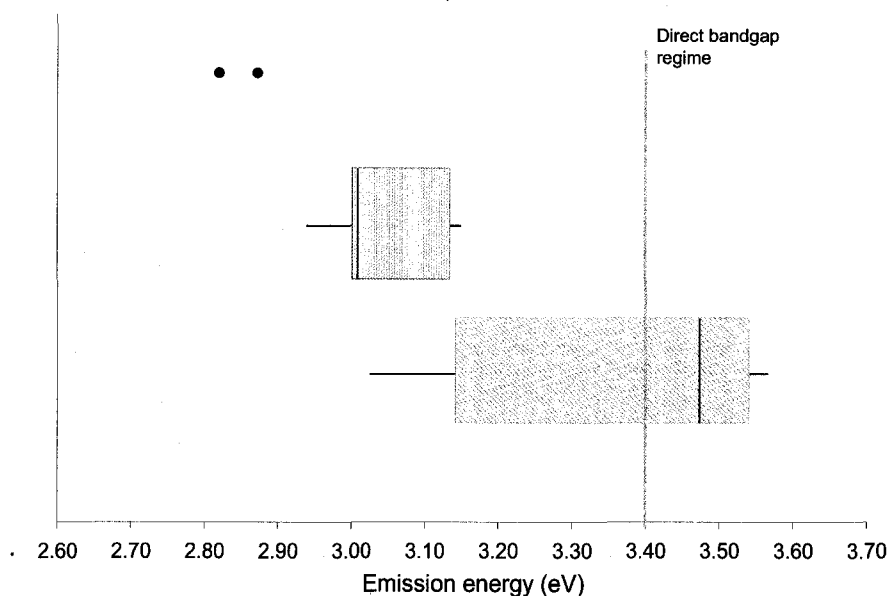


Figure 55. Boxplot of emission energy of undoped SiNWs (blue-diagonal line), doped SiNWs (green-vertical line) and Si spheres (dots), at an excitation wavelength of 250 nm.



From the box spread, there seems to be a shift in the doped SiNWs to a lower emission energy, but still overlapping the lower quartile of the undoped SiNWs. Doping of Si will introduce an energy state within the bandgap of Si. The p-dopant will have an energy state slightly above the valence band and the n-dopant slightly below the first conduction band of the Si bandgap. Emission from the second lowest conduction band to either of the dopant energy state results in a lower emission energy. This can explain the shift in emission energy observed in the doped samples.

Fluorescence spectroscopy allows clear differentiation of SiNWs from Si spheres and doped SiNWs. However, the emission ranges are broad thus it has high uncertainties. Alternative methods with high accuracy to determine the doping of SiNWs have to be resorted.

No.	Samples	Reaction temp. (°C)	Reaction time (min)	SiNW/sphere diameter (nm)	Excitation $\lambda$ (nm)	Emission $\lambda$ (nm)	Energy (eV)
1	DPS decomposed on Si substrate (No Au catalyst)	520	30		285 300	462 492	2.7 2.5
2	DPS decomposed on Si substrate (No Au catalyst)	555	30	*5000 $\pm$ 1900	250 271 300	432 442 470	2.9 2.8 2.6
3	Si particles Si substrate (with Au catalyst)	650	11	*3600 $\pm$ 400	250 271 300	440 446 468	2.8 2.8 2.7
4	SiNW on Si substrate	500	60		250 271 300	386 400 428	3.2 3.1 2.9
5	SiNW catalyzed by Al	500	109	46 $\pm$ 10	250 271 300	422 430 442	2.9 2.9 2.8
6	DPP/DPS	450	60	169 $\pm$ 57	250 271	396 408	3.1 3.0
7	DPP/DPS	500	60	148 $\pm$ 46	250 271	396 414	3.1 3.0
8	DPP/DPS	550	60		250 271 300 350	418 438 464 482	3.0 2.8 2.7 2.6
9	SiNW catalyzed by Sb	450	60	40 $\pm$ 12	250 271	408 420	3.0 3.0
10	SiNW catalyzed by Sb	500	60	42 $\pm$ 11	250 271	408 418	3.0 3.0
11	TPA/DPS	450	60	33 $\pm$ 6	250 271	394 408	3.1 3.0
12	TPA/DPS	500	60	54 $\pm$ 18	250 271 300	414 418 444	3.0 3.0 2.8
13	TPB/DPS	450	60	57 $\pm$ 10	250 271	414 432	3.0 2.9
14	TPB/DPS	505	60	102 $\pm$ 21	250 271 300	410 420 440	3.0 3.0 2.8

(\* Si particles diameter; Structure diameter extrapolated through SEM images)

Table 10. Summary of emission peaks of undoped SiNW, doped SiNW and Si sphere from fluorescence spectroscopy.

## Conclusion

The current research project provides a simple glass tube method for synthesis of SiNWs. The synthesis method involves a clean chemistry whereby no toxic or combustible gas eg. silane, or any mixture of toxic silane compounds with gases were used. The final excess of unreacted DPS was decomposed to  $\text{SiO}_x(\text{s})$ . This method also allows for a cleaner, less flammable and less toxic gas dopant, such as diborane and phosphine. By selecting appropriate liquid or solid dopant reagent that is soluble in DPS, doping can potentially be carried out under the current synthesis conditions.

The synthesis method presented here allows SiNWs growth on metallic, semiconductor, and insulating surfaces which facilitates the screening of potential contact materials with a low energy barrier. Furthermore, by selecting appropriate substrates to be used as template for growth of SiNWs, bulk SiNWs can be obtained by etching the template material post synthesis. Bulk SiNWs can be used for post assembly or alignment into potential devices.

Through optimization of the reaction condition and use of a double chamber glass tube reaction vessel, straight and uniformly narrow SiNWs can be achieved.

## **Chapter 4. Future work**

### **4.1. Characterization of dopant in SiNWs and junctions of SiNWs**

Better characterization techniques are still needed to determine the percentage and distribution of the dopant in the SiNWs. Dopant concentration in the SiNWs can be determined by Time-of-Flight Secondary Ion Mass Spectrometry (TOF SIMS). The location of the dopant can be detected by ultra-high vacuum STM which has been reported by Ma et al<sup>81</sup>. Finally, conductivity and I-V measurements should be performed to compare the epitaxial from the non-epitaxial contact SiNW junctions.

### **4.2. Synthesis of multiwall carbon nanotubes via glass tube method**

Single walled 1.5 nm diameter carbon nanotubes can conduct as much as 10  $\mu\text{A}/\text{nm}^2$  at room temperature, and exhibit a 1-D Luttinger liquid-type behavior implying phase-coherent electron transport. Because of their extraordinary thermal and chemical stability, carbon nanotubes are compatible with the current device processing environments.

By selecting the appropriate metal catalyst, reagent, and conditions, multi-wall carbon nanotube (MWCNT) can also be synthesized using the glass tube method. Iron nanoparticles (refer to Appendix A3 for synthesis) were used as the metal catalyst and naphthalene as a carbon precursor (1.0  $\mu\text{mol}$  Fe and 16  $\mu\text{mol}$  of naphthalene were used). The reaction was carried out at 610 °C for 2 hours. Figure 56a-c showed the similar competitive pathway for formation of CNTs and carbon particles as observed for SiNWs.

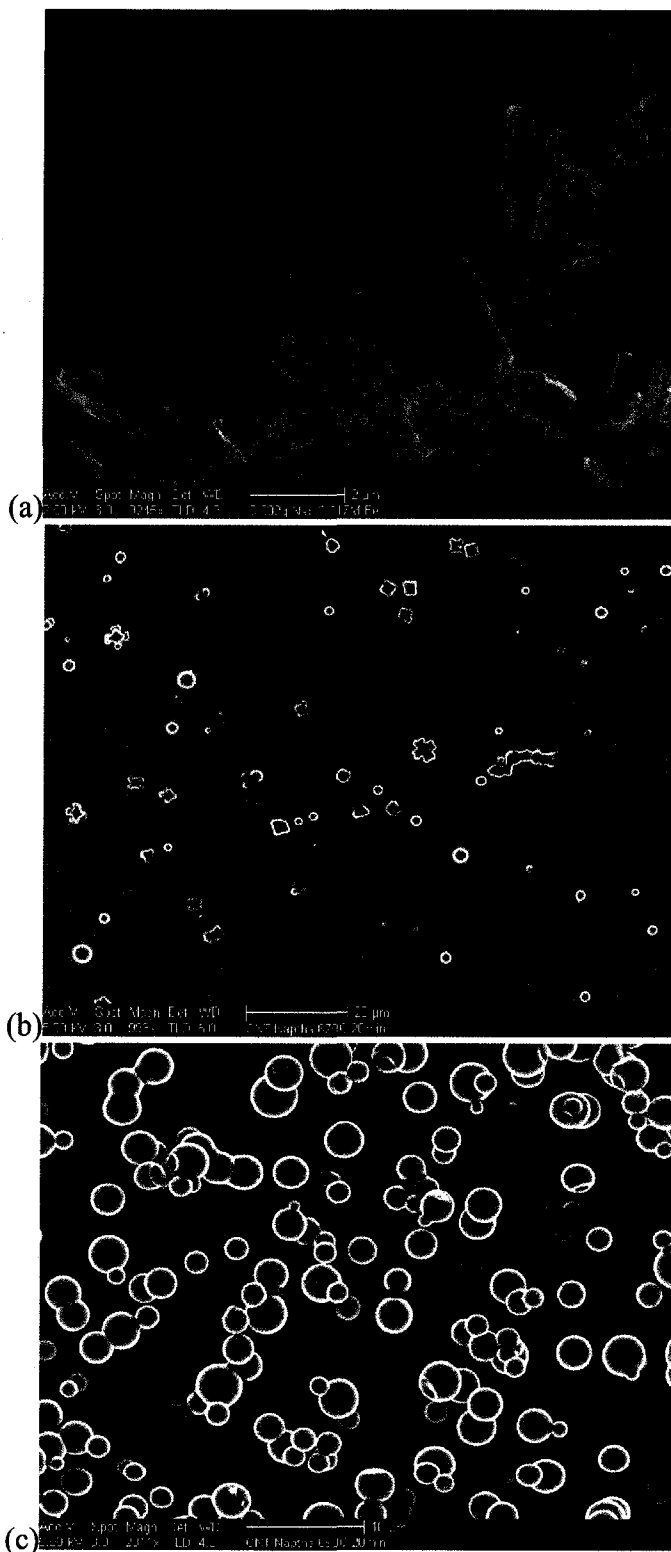


Figure 56. SEM images of CNTs synthesis at different temperature: (a) 610, (b) 670, and (c) 690 °C.

Apart from iron catalyst, nickel<sup>88,89,90</sup> has also been reported as a good catalyst for synthesis of CNTs. Nickel was synthesized with a similar reaction as used for gold and iron. CNT synthesis was carried out as described for Fe and the result is shown in Figure 57. Short curly structures were observed. It has been reported these were ascribed to amorphous carbon nanofibers<sup>91</sup> instead of CNTs. Further optimization in the synthesis conditions such as reagents concentrations, reaction temperature and time are needed to obtain CNTs.

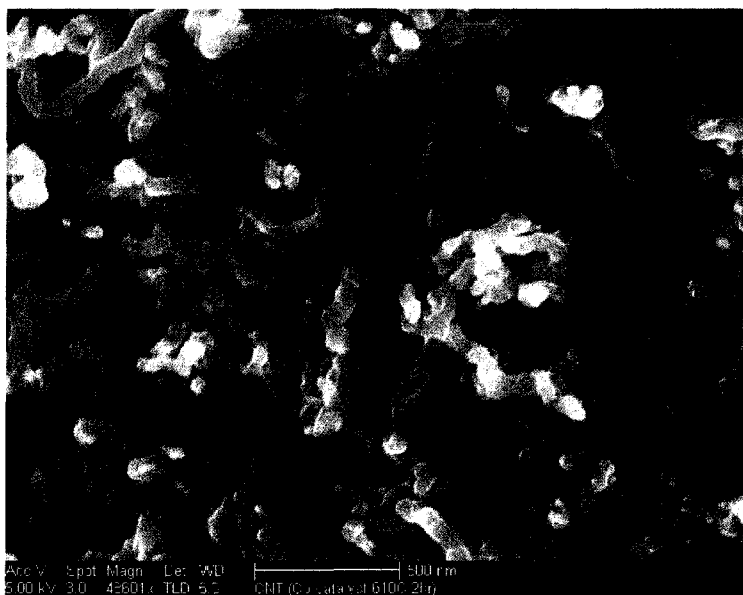


Figure 57. SEM images of curly carbon rods catalyzed from Ni.

#### 4.3. Challenges and limitation

Two of the greatest challenges in the glass tube synthetic technique are the choices of reagents and synthesis temperatures. An appropriate Si precursor or carbon precursor compounds must be carefully selected. If the organic precursor is decomposed before the desired reaction temperature this will result in formation of Si or C particles. Similarly if the eutectic temperature is higher then the decomposition

temperature of the precursor the results will again be particle formation. This has been observed by using Fe as catalyst for synthesis of SiNWs. The eutectic for Fe-Si is around 1200 °C (Figure 2) and decomposition of DPS is around 313 °C (Appendix B, Figure B2). As observed from section 3.3.5. heavy Si particles are observed with no SiNWs at synthesis temperature of 650 °C. Thus, Fe was not chosen as catalyst for synthesis of SiNWs.

A similar limitation has been observed in CNT synthesis. Different carbon precursors, beside naphthalene (melting point 81.2 °C and boiling point 218 °C), have been examined, namely, decane (boiling point 174.1 °C), hexadecane (boiling point 287 °C) and anthracene (melting point 218 °C; boiling point 340 °C). The catalyst used was an Fe-Co-Ni (mixture). A minimum temperature of 610 °C was required for synthesis of MWCNT.



Figure 58. SEM images of carbon particles observed using hexadecane (left) and anthracene (right) as carbon precursor.

Premature decomposition by hexadecane is unfavorable. Even though anthracene has a higher boiling point than naphthalene no tubes were observed. Anthracene, a triple fused benzene ring, could be structurally unfavorable as opposed

to naphthalene, a double fused benzene ring, since it requires higher deprotonation to form bonds with neighboring molecules.

A higher temperature generally produces better quality SiNWs and CNTs (single wall CNTs). The glass tube method is limited in high temperature range. The borosilicate glass has been observed to soften at 700 °C, thus reactions are limited to below 690 °C. To carry out synthesis at temperature higher than 700 °C with glass tube method, quartz tubes should be used but at a higher cost.

#### **4.4. Grid assembly of silicon nanowires**

Difficulties in assembly or in formation of ohmic contacts for nanowires or nanotubes hamper their device integration. Coulombic blockade and the associated quantum resistance degrade the resistance of electrical contacts. The top-down, or conventional lithographic approach, does not currently provide resolution below 15 nm, while the bottom-up approach, which requires self-assembly or mechanical placement needs large contact pads that vanquish the advantage of the nanoscale device density. One solution to this problem, which should be pursued, is to assemble them on a grid pattern<sup>92</sup>, where 2N wires generate  $N^2$  junctions<sup>93</sup>. Likharev et al have developed particularly attractive hybrid CMOS/nanodevice circuit architecture, dubbed CMOL<sup>94</sup> where proposed grid structures may be incorporated.

Future work in direct growth and alignment of junction appears plausible by restricting the path of the propagating gold by creating arrays of cross channels, as illustrated in Figure 59.



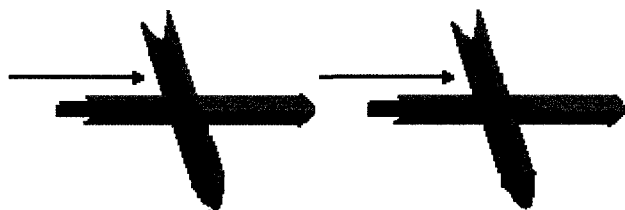


Figure 59. Cross array directional control growth of SiNWs.

By controlling the crystallinity of the wires (which depends on the synthesis condition) in conjunction with architecturally crafted cross array channels, ideal bipolar junction wire devices are plausible. For example, with the wires observed in Figure 47, a  $60^\circ$  cross-array channels can potentially create epitaxially bipolar junctions.

## References

- 
- <sup>1</sup> Faraday, M. *Phil. Trans.* **1857**, 147, 145
- <sup>2</sup> Binnig, G.; Rohrer, H.; Gerber, C.; Weibel, E. *Phys. Rev. Lett.* **1982**, 49, 57
- <sup>3</sup> Binnig, G.; Quate, C. F.; Gerber, C. *Phys. Rev. Lett.* **1986**, 56, 930
- <sup>4</sup> Lundstrom, M. *Science* **2001**, 299, 210
- <sup>5</sup> Ando, T., Arakawa, Y., Furuya, K., Komiyama, S., Nakashima, H. "Mesoscopic Physics and Electronics" Springer, Berlin (page 4)
- <sup>6</sup> Das, B.; Subramaniam, S.; Melloch, M. R. *Semicond. Sci. Technol.* **1993**, 8, 1347
- <sup>7</sup> T. Henning, *Charging effects in niobium nanostructures*, PhD thesis, Mikroelektronik och Nanovetenskap, Chalmers Tekniska Högskola AB och Göteborgs Universitet, Göteborg/Sweden, 1999.
- <sup>8</sup> Kautz, R. L.; Zimmerli, G.; Martinis, J. M. *J. Appl. Phys.* **1993**, 73, 2386
- <sup>9</sup> Korotkov, A. N.; Samuelson, M. R.; Vasenko, S. A. *J. Appl. Phys.* **1994**, 76, 6
- <sup>10</sup> Derycke, V.; Martel, R.; Appenzeller, J.; Avouris, Ph. *Nano. Lett.* **2001**, 1, 453
- <sup>11</sup> Martel, R.; Schmidt, T.; Shea, H. R.; Hertel, T.; Avouris, Ph. *Appl. Phys. Lett.* **1998**, 73, 2447
- <sup>12</sup> Wind, S. J.; Appenzeller, J.; Martel, R.; Derycke, V.; Avouris, Ph. *Appl. Phys. Lett.* **2002**, 80, 3817
- <sup>13</sup> Zhong, Z.; Fang, Y.; Lu, W.; Lieber, C. M. *Nano. Lett.* **2005**, 5(6), 1143
- <sup>14</sup> Jin, S.; Whang, D.; McAlpine, M. C.; Friedman, R. S.; Wu, Y.; Lieber, C. M. *Nano. Lett.* **2004**, 4(5), 915
- <sup>15</sup> Yao, Y.; Li, F.; Lee, S. T. *Chem. Phys. Lett.* **2005**, 406, 381

- 
- <sup>16</sup> Hochbaum, A. I.; Fan, R.; He, R.; Yang, P. *Nano. Lett.* **2005**, 5(3), 457
- <sup>17</sup> Gudiksen, M. S.; Wang, J.; Lieber, C. M. *J. Phys. Chem. B* **2001**, 105, 4062
- <sup>18</sup> Cui, Y.; Zhong, Z.; Wang, D.; Wang, W. U.; Lieber, C. M. *Nano. Lett.* **2003**, 3, 149
- <sup>19</sup> Webpage <http://www.ee.byu.edu/cleanroom/ohmic-schottky.phtml> (accessed on 04/30/07)
- <sup>20</sup> Aharonov, Y.; Bohm, D. *Phys. Rev.* **1959**, 115, 485
- <sup>21</sup> Yoshii, N.; Morita, S.; Shinozaki, A.; Aoki, M.; Morita, M. *IWGI*, **2003**, 96
- <sup>22</sup> Byon, K.; Tham, D.; Fischer, J. E.; Johnson, A. T. *Appl. Phys. Lett.* **2005**, 87, 193104
- <sup>23</sup> Huo, H. B.; Dai, L.; Liu, C.; You, L. P.; Yang, W. Q.; Ma, R. M.; Ran, G. Z.; Qin, G. G. *Nanotechnology* **2006**, 17, 5912
- <sup>24</sup> Cui, Y.; Duan, X.; Hu, J.; Lieber, C. M. *J. Phys. Chem. B* **2000**, 104, 5213
- <sup>25</sup> Ma, D. D. D.; Lee, C. S.; Lee, S. T., *Appl. Phys. Lett.* **2001**, 79, 2468.
- <sup>26</sup> Hamers, R. J.; Beck, J. D.; Eriksson, M. A.; Li, B.; Marcus, M. S.; Shang, L.; Simmons, J.; Streifer, J. A. *Nanotech.* **2006**, 17, S280
- <sup>27</sup> Dong, L.; Bush, J.; Chirayos, V.; Solanki, R.; Jiao, J.; Ono, Y.; Conley, J. F. Jr.; Ulrich, B. D. *Nano. Lett.*, **2005**, 5, 2112
- <sup>28</sup> Huang, Y.; Duan, X.; Wei, Q.; Lieber, C. M. *Science* **2001**, 291, 630
- <sup>29</sup> Cui, Y.; Lieber, C. M. *Science* **2001**, 291, 851
- <sup>30</sup> Huang, Y.; Duan, X.; Cui, Y.; Lauhon, L. J.; Kim, K. H.; Lieber, C. M. *Science* **2001**, 294, 1313
- <sup>31</sup> Cui, Y.; Zhong, Z.; Wang, D.; Wang, W. U.; Lieber, C. M. *Nano. Lett.* **2003**, 3, 149

- 
- <sup>32</sup> Duan, X.; Huang, Y.; Lieber, C. M. *Nano. Lett.* **2002**, 2, 487
- <sup>33</sup> Jin, S.; Whang, D.; McAlpine, M. C.; Friedman, R. S.; Wu, Y.; Lieber, C. M. *Nano. Lett.* **2004**, 4, 915
- <sup>34</sup> Whang, D.; Jin, S.; Lieber, C. M. *Nano. Lett.* **2003**, 3, 951
- <sup>35</sup> Homma, Y.; Finnie, P.; Ogino, T.; Noda, H.; Urisu, T. *J. Appl. Phys.* **1999**, 86, 3083
- <sup>36</sup> Finnie, P.; Homma, Y. *Appl. Phys. Lett.* **1998**, 72, 827
- <sup>37</sup> Ogino, T.; Hibino, H.; Homma, Y. *Appl. Surf. Sci.* **1997**, 642
- <sup>38</sup> Homma, Y.; Finnie, P.; Ogino, T. *Appl. Phys. Lett.* **1999**, 74, 815
- <sup>39</sup> Tabib-Azar, M.; Nassirou, M.; Wang, R.; Sharma, S.; Kamins, T. I.; Islam, M. S.; Williams, R. S. *Appl. Phys. Lett.* **2005**, 87, 113102-1
- <sup>40</sup> Sharma, S.; Kamins, T. I.; Islam, M. S.; Williams, R. S.; Marshall, A. F. *J. Crystal Growth* **2005**, 280, 562
- <sup>41</sup> Islam, M. S.; Sharma, S.; Kamins, T. I.; Williams, R. S. *Appl. Phys. A* **2005**, 80, 1133
- <sup>42</sup> Islam, M. S.; Sharma, S.; Kamins, T. I.; Williams, R. S. *Nanotechnology* **2004**, 15, L5
- <sup>43</sup> Sharma, S.; Kamins, T. I.; Williams, R. S. *Appl. Phys. A* **2005**, 80, 1225
- <sup>44</sup> Wagner, R. S.; Ellis, W. C. *Appl. Phys. Lett.* **1964**, 4(5), 89
- <sup>45</sup> Massalski, Thaddeus B. *Binary alloy phase diagrams* Metals Park, Ohio: American Society for Metals, 1986 (volume 1, pg 313), ISBN 0871702622
- <sup>46</sup> Morales, A. M.; Lieber, C. M. *Science* **1998**, 279, 208

- 
- <sup>47</sup> Massalski, Thaddeus B. *Binary alloy phase diagrams* Metals Park, Ohio: American Society for Metals, 1986, (volume 2, pg 1108), 0871702630
- <sup>48</sup> Wang, N.; Tang, Y. H.; Zhang, Y. F.; Lee, C. S.; Lee, S. T. *Phys. Rev. B* **1998**, 58, R16024
- <sup>49</sup> Zhang, R. Q.; Chu, T. S.; Cheung, H. F.; Wang, N.; Lee, S. T. *Phys. Rev. B* **2001**, 64, 113304
- <sup>50</sup> Zhang, R. Q.; Chu, T. S.; Cheung, H. F.; Wang, N.; Lee, S. T. *Mater. Sci. Eng. C* **2001**, 16, 31
- <sup>51</sup> Bsiesy, A.; Vial, J. C. *Journal of Luminescence* **1996**, 70, 310
- <sup>52</sup> Huo, J.; Solanki, R.; Freeouf, J. L.; Carruthers, J. R. *Nanotechnology* **2004**, 15, 1848
- <sup>53</sup> Audoit, G.; Mhuirheartaigh, É. N.; Lipson, S. M.; Morris, M. A.; Blau, W. J.; Holmes, J. D. *J. Mater. Chem.* **2005**, 15, 4809
- <sup>54</sup> Holmes, J. D.; Johnston, K. P.; Doty, R. C.; Korgel, B. A. *Science* **2000**, 287, 1471
- <sup>55</sup> Gerion, D.; Zaitseva, N.; Fakra, S. *Synchrotron Radiation News* **2003**, 16(3), 25
- <sup>56</sup> Sharma, S.; Kamins, T. I.; Williams, R. S. *J. Cryst. Growth* **2004**, 267, 613
- <sup>57</sup> Wajda, E. S.; Kippenhan, B. W.; White, W. H. *IBM Journal* **1960**, 288
- <sup>58</sup> Wang, Y.; Schmidt, V.; Senz, S.; Gösele, U. *Nature Nanotechnology* **1**, **2006**, 186
- <sup>59</sup> Sharma, S.; Sunkara, M. K. *Nanotechnology* **15**, **2004**, 130
- <sup>60</sup> Kamin, T. I.; Williams, R. S.; Basile, D. P.; Hesjedal, T.; Harris, J. S. *J. Appl. Phys.* **89**, **2001**, 1008
- <sup>61</sup> Westwater, J.; Gosain, D. P.; Tomiya, S.; Usui, S. *J. Vac. Sci. Technol. B.* **1997**, 15(3), 554

- 
- <sup>62</sup> Homma, Y.; Finnie, P.; Ogino, T.; Noda, H.; Uisu, T. *J. Appl. Phys.* **1999**, 86(6), 3083
- <sup>63</sup> Hannon, J. B.; Kodambaka, S.; Ross, F. M.; Tromp, R. M. *Nature Letters* **2006**, 440, 69
- <sup>64</sup> Cui, Y.; Lauhon, L. J.; Gudiksen, M. S.; Wang, J.; Lieber, C. M. *Appl. Phys. Lett.* **2001**, 78, 2214
- <sup>65</sup> Wu, Y.; Cui, Y.; Huynh, L.; Barrelet, C. J.; Bell, D. C.; Lieber, C. M. *Nano. Lett.* **2004**, 4, 433
- <sup>66</sup> Givargizov, E. I. *J. Cryst. Growth* **1975**, 31, 20
- <sup>67</sup> Grove, A. S. *Physics and Technology of Semiconductor devices*, John Wiley, New York 1967, Chapter 1 page 16
- <sup>68</sup> Dubrovski, D.G. *Physical Review E* **2006**, 73, 021603
- <sup>69</sup> Lee, S. W.; Kwok, D. Y.; Laibinis, P. E. *Physical Review E* **2002**, 65, 051602
- <sup>70</sup> Sharma, S.; Kamins, T. I.; Williams, R. S. *J. Cryst. Growth* **2004**, 267, 613
- <sup>71</sup> Kamins, T. I.; Williams, R. S. Basile, D. P.; Hesjedal, T.; Harris, J. S. *J. Appl. Phys.* **2001**, 89(2), 1008
- <sup>72</sup> Sunkara, M. K.; Sharma, S.; Miranda, R.; Lian, G.; Dickey, E. C. *Appl. Phys. Lett.* **2001**, 79(10), 1546
- <sup>73</sup> Sharma, S.; Sunkara, M. K. *Nanotechnology* **2004**, 15, 130
- <sup>74</sup> Wang, Y.; Schmidt, V.; Senz, S.; Gösele, U. *Nature Nanotechnology* **2006**, 1, 186
- <sup>75</sup> Massalski, Thaddeus B. *Binary alloy phase diagrams* Metals Park, Ohio: American Society for Metals, 1986, (volume 2, pg 2056), 0871702630

- 
- <sup>76</sup> Meng, C. Y.; Shih, B. L.; Lee, S. C. *Journal of Nanoparticle Research* **2005**, 7, 615
- <sup>77</sup> Lew, K. K.; Pan, L.; Bogart, T. E.; Dilts, S. M.; Dickey, E. C.; Redwing, J. M.; Wang, Y.; Cabassi, M.; Mayer, T. S.; Novak, S. W. *Appl. Phys. Lett.* **2004**, 85, 3101
- <sup>78</sup> Kimukin, I.; Islam, M. S.; Williams, R. S. *Nanotechnology* **2006**, 17, S240
- <sup>79</sup> Wang, F.; Lew, K. K.; Ho, T. T.; Pan, L.; Novak, S. W.; Dickey, E. C.; Redwing, J. M.; Mayer, T. S. *Nano. Lett.* **2005**, 5, 2139
- <sup>80</sup> Goncher, G.; Solanki, R.; Carruthers, J. R.; Conley, Jr. J.; Ono, Y. *Journal of Electronic Materials* **2006**, 35, 1509
- <sup>81</sup> Ma, D. D. D.; Lee, C. S.; Lee, S. T., *Appl. Phys. Lett.* **2001**, 79, 2468.
- <sup>82</sup> Audoit, G.; Mhuirheartaigh, É. N.; Lipson, S. M.; Morris, M. A.; Blau, W. J.; Holmes, J. D. *J. Mater. Chem.* **2005**, 15, 4809
- <sup>83</sup> Rama Krishna, M. V.; Friesner, R. A. *J. Phys. Chem.* **1992**, 96, 873
- <sup>84</sup> Brus, L. E.; Szajowski, P. F.; Wilson, W. L.; Harris, T. D.; Schuppler, S.; Citrin, P. *H. J. Am. Chem. Soc.* **1995**, 117, 2915
- <sup>85</sup> Wang, Y.; Herron, N. *J. Phys. Chem.* **1991**, 95, 525
- <sup>86</sup> Veinot, J. G. C. *Chem. Commun.* **2006**, 4160
- <sup>87</sup> Phillips, J. C. *Phys. Rev.* **1962**, 125(6), 1931
- <sup>88</sup> Merkulov, V.I.; Lowndes, D. H.; Lowndes, D.H.; Wei, Y. Y.; Wei, Y.Y.; Eres, G.; Voelkl, E. *Appl. Phys. Lett.* **2000**, 76, 3556
- <sup>89</sup> Merkulov, V. I.; Melechko, A. V.; Guillorn, M. A.; Lowndes, D. H.; Simpson, M. L. *Appl. Phys. Lett.* **2001**, 79, 2970

- 
- <sup>90</sup> Merkulov, V. I.; Melechko, A. V.; Guillorn, M. A.; Simpson, M. L.; Lowndes, D. H.; Whealton, J. H.; Raridon, R. J. *Appl. Phys. Lett.* **2002**, 80, 4816
- <sup>91</sup> Jose-Yacaman, M.; Miki-Yoshida, M.; Rendon, L.; Santiesteban, J. G. *Appl. Phys. Lett.* **1993**, 62, 657
- <sup>92</sup> Andr DeHon, **Array-Based Architecture for Molecular Electronics**, First Workshop on Non-Silicon Computation (NSC-1), Feb. 3, 2002
- <sup>93</sup> Gao, C.J.; Hammerstrom, D. "Implementation of Cortical Models on CMOL," submitted to NanoArch 06.
- <sup>94</sup> Likharev, K.K.; D.V. Strukov, CMOL: Devices, circuits, and architectures, in *Introducing Molecular Electronics*, G.C.et. al., Editor. 2004, Springer: Berlin.



## Appendix A. Chemical reagents

AuCl <sub>3</sub> .xHCl	STREM CHEMICALS; CAS No. 13453-07-1, Lot# 141380-S1, Gold(III) chloride, 99%
1,8-Octanediol	98%, Sigma-Aldrich, Cat. No. O-330-3, CAS No. 629-41-4
Cyclohexane	Sigma-Aldrich, Cat. No. 27,062-8, CAS No. 110-82-7, HPLC grade
Dimethylformamide (DMF)	Sigma-Aldrich, Cat. No. 319937, CAS No. 68-12-2, >99.8%
Ferric chloride	97%, Sigma-Aldrich, Cat. No. 157740, CAS No. 7705-08-0
Sodium borohydride (NaBH <sub>4</sub> )	Sigma-Aldrich, Cat. No. 452882, CAS No. 16940-66-2, powder, >98.5%
Alumina	Sigma-Aldrich, Cat. No. 342726, CAS No. 1344-28-1, calcined, 150-325 mesh
Antimony trichloride (SbCl <sub>3</sub> )	Acros Organic, CAS No. 10025-91-9, 99.5%
Diphenylsilane	Sigma-Aldrich, Cat. No. 14,848-2, CAS No. 775-12-2, 97%
Triphenylsilane	Sigma-Aldrich, Cat. No. 148504, CAS No. 789-25-3, 97%
Triphenylborane (TPB)	Sigma-Aldrich, Cat. No. T82201, CAS no. 960-71-4, powder, <2% H <sub>2</sub> O
Diphenyl phosphine (DPP)	Sigma-Aldrich, Cat. No. 252964, CAS No. 829-85-6, 98%
Triphenyl antimony (TPA)	Sigma-Aldrich, Cat. No. T81809, CAS No. 603-36-1, 99%
Ammonium bifluoride (NH <sub>4</sub> F.HF)	Mallinckrodt Chemicals, CAS No. 1341-49-7

## **Appendix B. Synthesis and characterization of gold and iron nanoparticles by templating with bolamphiphiles**

The newly developed synthetic method uses 1,8-octanediol as capping agent in the synthesis of gold nanoparticles. Synthesis studies are performed in 1.) aqueous ( $\text{H}_2\text{O}$ ); 2.) non-aqueous (DMF) medium; and 3.) the flexibility of the method is further established by synthesizing alternative nano-metallic (Fe) particles.

### **B.1. Preparation of stock solutions**

#### **Preparation of gold(III) chloride with 1,8-octanediol in aqueous medium**

A stock solution (0.03 M) of  $\text{Au}^{3+}(\text{aq})$  was prepared by dissolving  $\text{AuCl}_3 \cdot x\text{HCl}(\text{concentrated})$  in deionized water. 0.11 M 1,8-octanediol in  $\text{H}_2\text{O}$  was prepared. The  $\text{Au}^{3+}(\text{aq})$  solution was added to 1,8-octanediol (0.11 M) solution (amount per each study outline in the following sections) followed by vortex mixing for few minutes. The resulting solution had a transparent yellow color.

#### **Preparation of gold(III) chloride with 1,8-octanediol in non-aqueous medium**

0.34 M 1,8-octanediol in DMF was prepared. The  $\text{Au}^{3+}(\text{aq})$  solution was added to 1,8-octanediol (0.34 M) solution (amount per each study in the following sections) followed by vortex mixing for few minutes.

#### **Preparation of ferric chloride solution with 1,8-octanediol in aqueous medium**

Ferric chloride was dissolved in distilled water with a final concentration of 0.031 M. 40  $\mu\text{L}$  of aqueous ferric chloride (0.031 M) was pipetted into 2.0 mL of 1,8-octanediol (0.11 M) solution prepared as before.

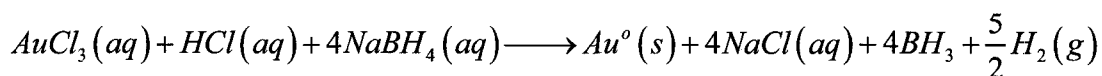
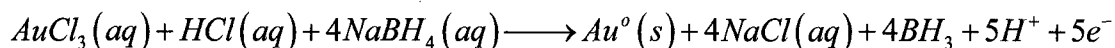
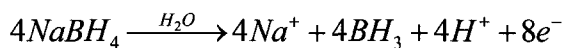
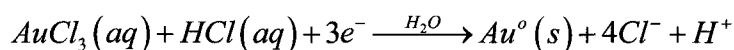
### Preparation of NaBH<sub>4</sub> solution

A 0.27 M solution of NaBH<sub>4</sub> was prepared by dissolving  $0.3317 \pm 0.0002$  g of NaBH<sub>4</sub> solid into  $33.2 \pm 0.2$  mL of water. Hydrogen gas evolution observed upon dissolving. The shelf life of NaBH<sub>4</sub> solution was determined to be 2 days from the date of preparation. After 2 days the rate of reduction by NaBH<sub>4</sub> was extremely slow.

### B.2. Synthesis of gold nanoparticles by stabilizing in 1,8-octanediol in aqueous medium

1,8-octanediol was used to provide steric barrier against flocculation of nanoparticles. It has two terminal hydroxyl (-OH) groups that can potentially have high affinity for oxide and metallic surfaces providing sufficient binding strength to the respective surfaces. And yet it is easily removable from gold nanoparticles than the long chain thiols. White crystals of 1,8-octanediol were slightly (0.11 M) soluble in water at room temperature forming clear and colorless solutions.

A freshly prepared 40  $\mu$ l of NaBH<sub>4</sub> solution was pipetted into the 2.5 ml of the 1,8-octanediol/Au<sup>3+</sup> solution. Upon adding NaBH<sub>4</sub> the solution turned clear purple immediately. The solution was stable and exhibited no large scale aggregation with time. The redox reaction:



To investigate maximum amount of stabilized gold, a series of gold solutions with increasing concentration were prepared. UV absorbance measurements of the octanediol-Au<sup>0</sup> solution were collected (Shimadzu UV-260 spectrophotometer) (see Figure B1).



Figure B1. Diol-Au<sup>0</sup> solution in aqueous medium.

A 900  $\mu$ M octanediol-Au<sup>0</sup> solution was used for AFM and SEM studies. A few drops of solution were deposited on a copper TEM grid and a microscope coverslip and then these samples were dried by baking them at 100 °C for 30 minutes.

## Results

All the octanediol-Au<sup>0</sup> mixtures remain translucent with decreasing intensity of purple color with the lowest concentration gold having a faint pink color. Only the solution prepared above the saturation limit ( $\sim$ 1.0 mM), that was 3.1 mM octanediol-Au<sup>0</sup>, had black aggregate depositing at the bottom of the tube. The control remained clear and colorless.

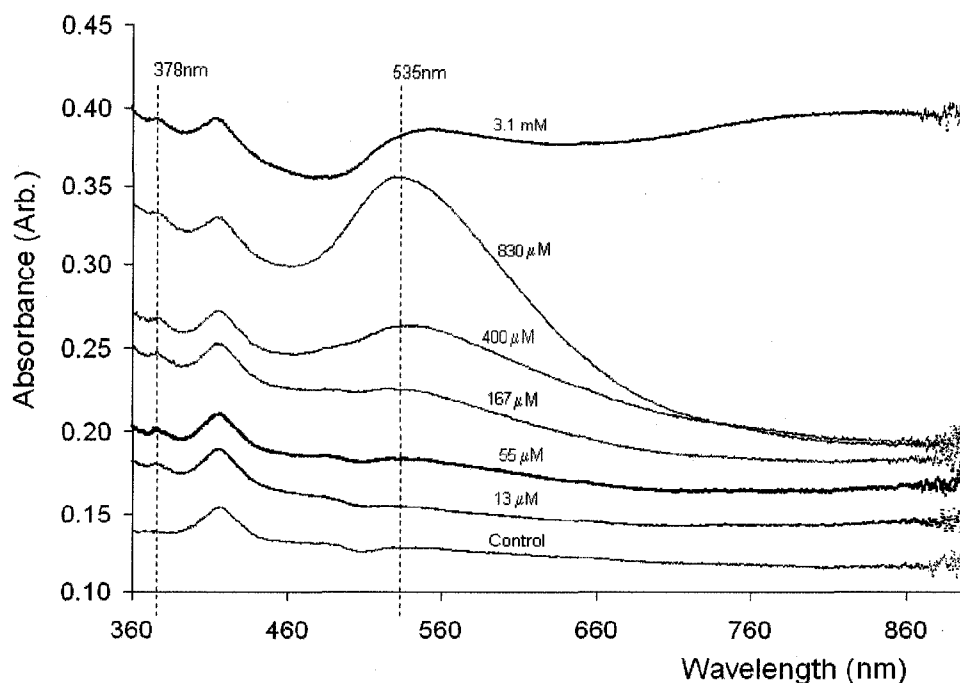


Figure B2. UV absorbance spectra of different concentration of octanediol-Au<sup>0</sup> in water [Gold concentration: 3.1mM, 400  $\mu$ M, 167  $\mu$ M, 55  $\mu$ M, and 13  $\mu$ M. The control consist of 1,8-octanediol and NaBH<sub>4</sub>].

The octanediol-Au<sup>0</sup> solution have maximum absorption peak at 535 nm shown in Figure B2. The peak intensity increases with concentration.

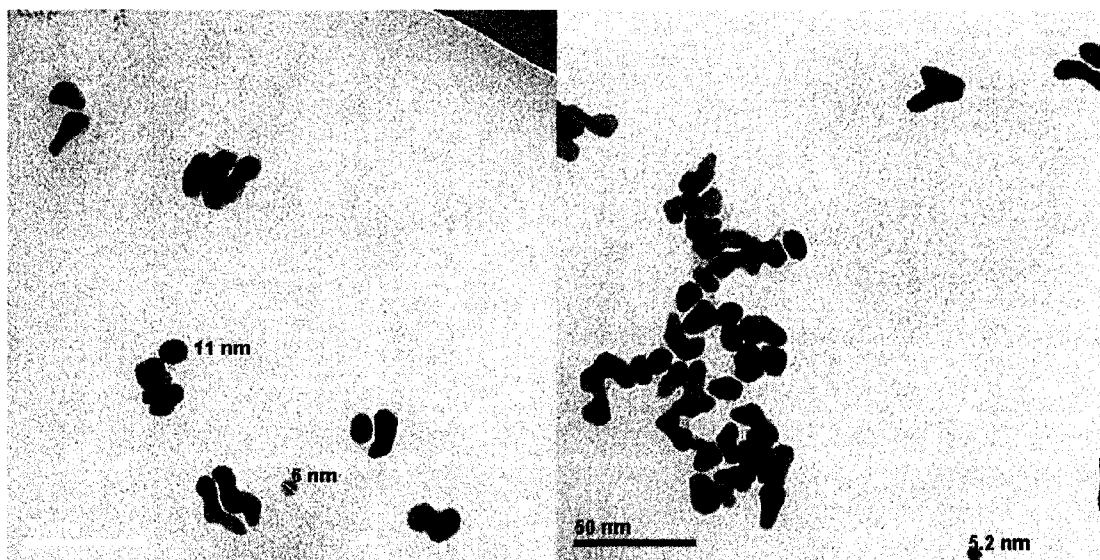


Figure B3. TEM images of 900  $\mu$ M octanediol-Au<sup>0</sup> solution in water.

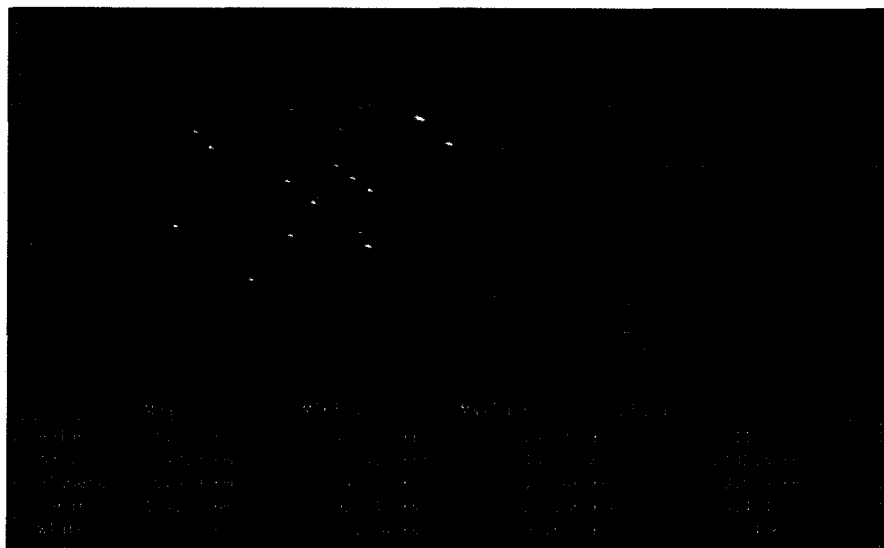


Figure B4. AFM image of 900  $\mu\text{M}$  octanediol- $\text{Au}^0$  solution deposited on Si substrate.

From the AFM images (Figure B4), the mean height of the gold particles was approximately 4.8 nm and the mean diameter was approximately 7.1 nm. Gold particles as small as 5 nm were observed with TEM (Figure B3). The dimension of the gold particles obtained from TEM was comparable to the AFM analysis as shown in Table B1.

Region 1				Region 2			
No.	Length (L) (nm)	Width (W) (nm)	Diameter (D) (nm)	No.	Length (L) (nm)	Width (W) (nm)	Diameter (D) (nm)
1	21.5	6.5	11.8	1	11.3	9.7	10.5
2	12.9	10.1	11.4	2	18.3	9.1	12.9
3	25.8	5.4	11.8	3	14.0	11.3	12.6
4	20.4	7.5	12.4	4	24.7	5.4	11.5
5	25.8	7.5	13.9	5	18.8	6.5	11.1
6	11.8	8.6	10.1	6	30.1	14	20.5
7	12.4	9.1	10.6	7	20.4	9.7	14.1
8	21.5	6.5	11.8	8	25.8	7.5	13.9
9	15.1	7.5	10.6	9	23.7	6.5	12.4
10	28.0	4.3	11.0	10	17.2	9.7	12.9
11	16.1	9.7	12.5	11	16.1	6.5	10.2
12	17.2	7.0	11.0	12	12.9	8.6	10.5
13	16.7	7.5	11.2	13	22.0	8.6	13.8
14	24.7	5.4	11.5	14	19.4	4.3	9.1
15	15.1	8.6	11.4	15	22.6	4.3	9.9
16	19.4	10.2	14.1	16	21.5	8.1	13.2
17	18.3	10.8	14.1	17	13.4	9.1	11.0
18	17.2	9.1	12.5	18	17.2	11.8	14.2
19	14.0	7.5	10.2	19	21.5	6.5	11.8
20	19.9	7.5	12.2	20	19.4	5.4	10.2
21	21.5	11.8	15.9	21	14.0	8.6	11.0
22	19.9	11.8	15.3	22	15.1	9.1	11.7
23	17.2	5.4	9.6	23	15.6	12.4	13.9
24	12.9	8.6	10.5	24	14.5	7.0	10.1
25	17.2	7.5	11.4	25	20.4	10.2	14.4
Average	18.5	8.1	12.0	Average	18.8	8.4	12.3
Std. Dev	4.4	2.0	1.6	Std. Dev	4.6	2.5	2.3

Table B1. Particle size analysis for 900  $\mu\text{M}$  octanediol-Au<sup>0</sup> in water sample from TEM imaging.

### B.3. Synthesis of iron nanoparticles by stabilizing in 1,8-octanediol (aqueous medium)

It has been reported that silicon nanowires can be grown from any nanoparticulate metal catalyst. An alloy of iron-gold at 85% Au:15% Fe has an

eutectic temperature at 228 °C<sup>95</sup>. An addition of a third component, Si, might produce a ternary phase with an eutectic temperature even lower than 228 °C.

Before attempting to synthesize Au-Fe alloy nanoparticles, iron nanoparticles was synthesized by stabilizing using 1,8-octanediol following the procedure as described for gold. Freshly prepared 0.27 M NaBH<sub>4</sub> was pipetted (30 µL) in to the Fe<sup>3+</sup>-octanediol solution. The solution had a very faint yellow color prior to addition of NaBH<sub>4</sub>. After addition of NaBH<sub>4</sub>, the yellow color intensified and the solution remained clear. The final concentration of Fe<sup>0</sup> was  $6.0(10^{-4})$  M. Over a period of 24 hours, yellow precipitates was formed at the bottom of the solution. This suggests that 0.11 M 1,8-octanediol solution was not able to stabilize the iron resulting in aggregation to larger particles. The synthesis was repeated at a lower concentration of Fe<sup>3+</sup>/Fe<sup>0</sup> until no precipitation was observed. The successful solution:  $2.5(10^{-4})$  M Fe<sup>3+</sup>/Fe<sup>0</sup> in 1,8-octanediol was prepared with no precipitate or aggregate formed. The solubility limit of ferric chloride in 0.11 M 1,8-octanediol is approximately  $3.0(10^{-4})$  M, which is three times lower than gold(III) chloride (~1.0 mM).

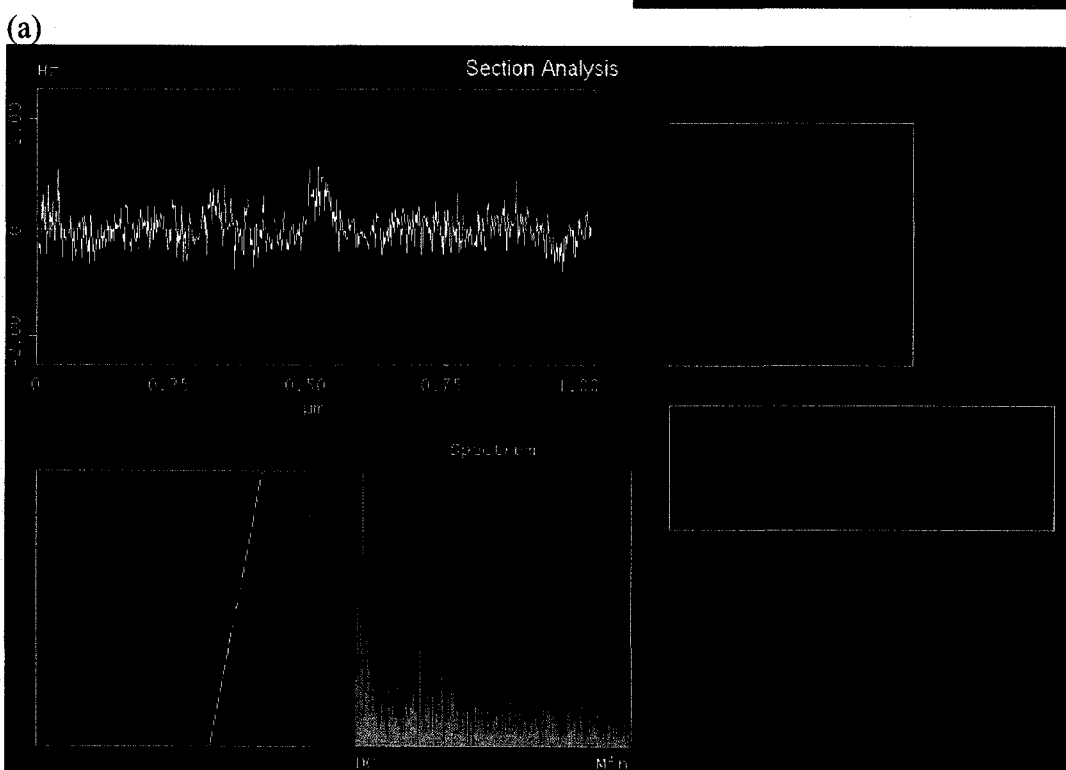
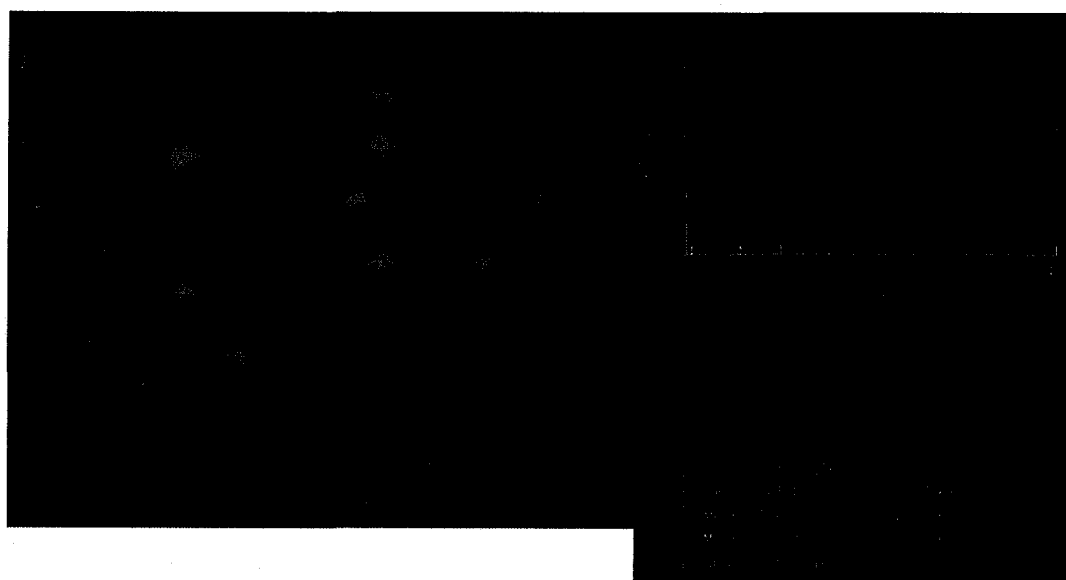
The 1,8-octanediol-Fe<sup>0</sup> ( $2.5(10^{-4})$  M) solution was pipetted on to a fresh microscope grade coverslip then evaporated to dry by heating on a hot plate. MFM imaging was used to study the 1,8-octanediol stabilized Fe<sup>0</sup> particles.

---

<sup>95</sup> Moffatt, William G. *Moffatt's handbook of binary phase diagrams* (General Electric Company, Corporate Research and Development, 1976)



## Results



(b) Figure B5. MFM (a) 3-D tilted topography and (b) cross-sectional analysis of frequency modulation spectra of octanediol-Fe<sup>0</sup>.

The iron particles had an average grain height of 6.2 nm observed in the height topography (Figure B5a) and an average frequency modulation of 1.1 Hz (Figure B5b) near the resolution limit for MFM.

#### **B.4. Synthesis of Au-Fe nanoparticles by stabilizing in 1,8-Octanediol.**

Gold coated iron particles in a core-shell structure, has been reported by Kauzlarich et. al.<sup>96,97</sup>. In their study iron was initially reduced in reverse micelle with NaBH<sub>4</sub> followed by addition of HAuCl<sub>4</sub> (prepared as micelle solution).

Gold-iron particles stabilized in 1,8-octanediol were synthesized by chemical reduction with NaBH<sub>4</sub>. Two different Au-Fe nanoparticles syntheses were attempted. The first method consisted of Fe core/Au shell that involved reduction of ferric chloride before gold(III) chloride in 1,8-octanediol solution, and the second method consist of co-reduction of iron and gold chloride. For Fe core/Au shell, 40  $\mu$ L of 0.032 M FeCl<sub>3</sub> was pipetted into 10.0 mL of 1,8-octanediol followed by addition of NaBH<sub>4</sub>. AuCl<sub>3</sub> (0.03 M) was then pipetted (160  $\mu$ L) into the final solution. The resultant solution consisted of 0.127 mM Fe<sup>0</sup> and 0.48mM Au<sup>0</sup>, with a mole ratio of 1:4 (Fe: Au). The solution was a transparent dark purple with no precipitate. A drop of the Fe/Au-octanediol solution was pipetted on to a holey carbon TEM grid and dried overnight. The sample was imaged using TEM (Figure B7).

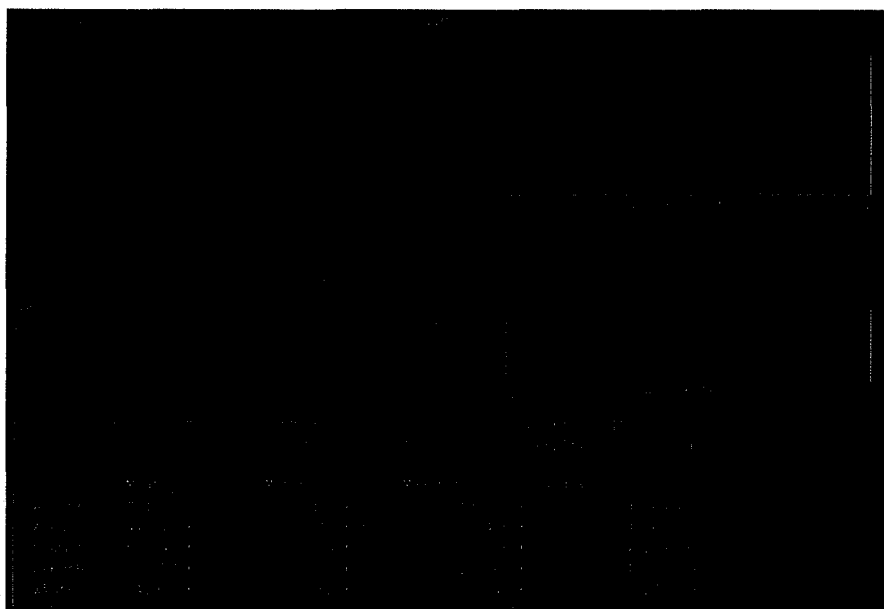
---

<sup>96</sup> Cho, S. J.; Idrobo, J. C.; Olamit, J.; Liu, K.; Browning, N. D.; Kauzlarich, S. M. *Chem. Mater.* **2005**, 17, 3186

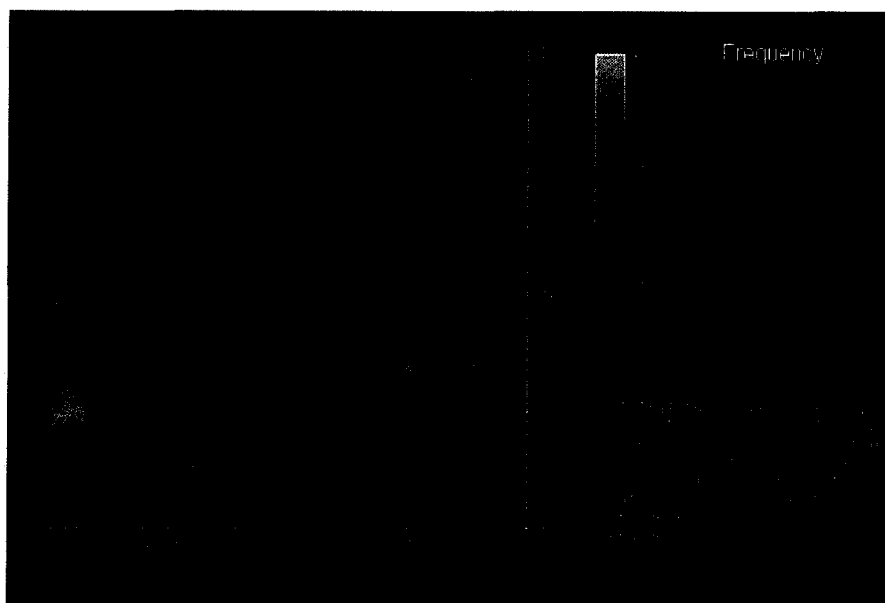
<sup>97</sup> Cho, S. J.; Kauzlarich, S. M.; Olamit, J.; Liu, K.; Grandjean, F.; Rebbouh, L.; Long, G. J. *J. Appl. Phys.* **2004**, 95(11), 6804

In the co-reduction of Fe/Au, same amounts of  $\text{FeCl}_3$  and  $\text{AuCl}_3$  were pipetted into 9.5 mL of 1,8-octanediol solution first before the addition of  $\text{NaBH}_4$ . The solution was clear and dark purple in color with no precipitate. The solution was pipetted on to a microscope grade glass slide and baked at 100 °C to dry then heated on a hot plate to further removed excess diol. The sample was imaged using MFM with frequency modulation detection as described in Fe particles studies.

## Results



(a)



(b)  
Figure B6. MFM (a) height image and (b) frequency modulation image of Au-Fe particles (by co-reduction in diol).

The particles have a mean height of 7.5 nm and mean diameter  $\sim 70$  nm (Figure B6a). The maximum frequency deflection was approximately 3 Hz (Figure B6b).

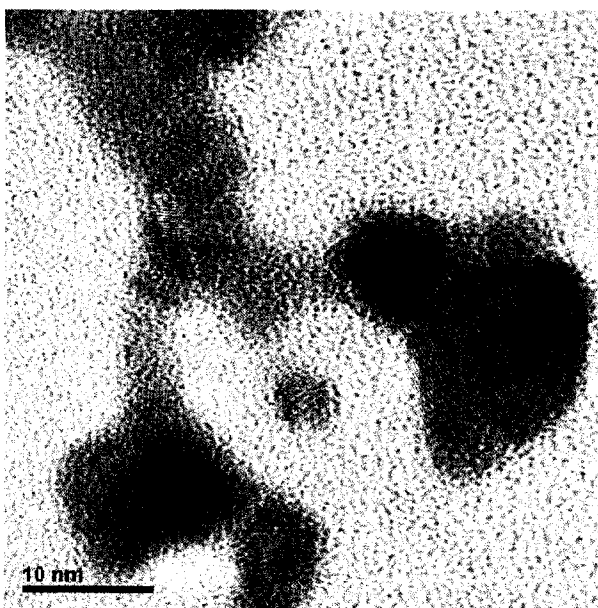


Figure B7. TEM image of Au-Fe particles (Fe core/Au shell)

Lattice planes were observed in TEM (Figure B7) for the Fe core/Au shell samples but the TEM results were inconclusive for a true existence of a Fe core/Au shell structure.

#### **B.5. Chemical reduction of gold in N,N-dimethylformamide (DMF)**

The 1,8-octanediol stabilized gold and iron nanoparticles synthesized in water medium suffers from limited salt solubility. The solubility limit of ferric chloride was approximately 0.3 mM and that of gold(III) chloride was approximately 1.0 mM. The reason for such a low solubility was because 1,8-octanediol itself has a low solubility in water (0.11 M). In order to prepare higher concentration of gold and iron, higher concentration of 1,8-octanediol in the solvent medium was needed, hence DMF was chosen to replace water.

Diol-Au<sup>3+</sup> (in DMF) solution was reduced with NaBH<sub>4</sub>. The diol-Au<sup>0</sup> solution was pipetted on to a fresh microscope glass slide then dried by baking at 100 °C for 2 hours. The sample was then heated on hot plate to evaporate away the remain 1,8-octanediol. The sample plate was imaged using AFM (Figure B8).

A series of gold solutions in DMF with increasing concentration were prepared. The UV-Visible absorbance of the solutions was analyzed.

#### **Results**

The AFM image was first obtained for 1,8-octanediol (dissolved in DMF) spin coated on glass substrate. 1,8-octanediol in DMF acts as a template for the formation of gold or iron nanoparticles.



Figure B8. 0.34 M 1,8-Octanediol in DMF spin coated on glass substrate. (a) 3-D topography (left) and (b) Dimension analysis (right).

The diol deposits had diameter of  $\sim 25$  nm and a height of  $\sim 2.6$  nm (Figure B8). The corresponding AFM image of gold nanoparticles synthesized in DMF is shown in Figure B9.

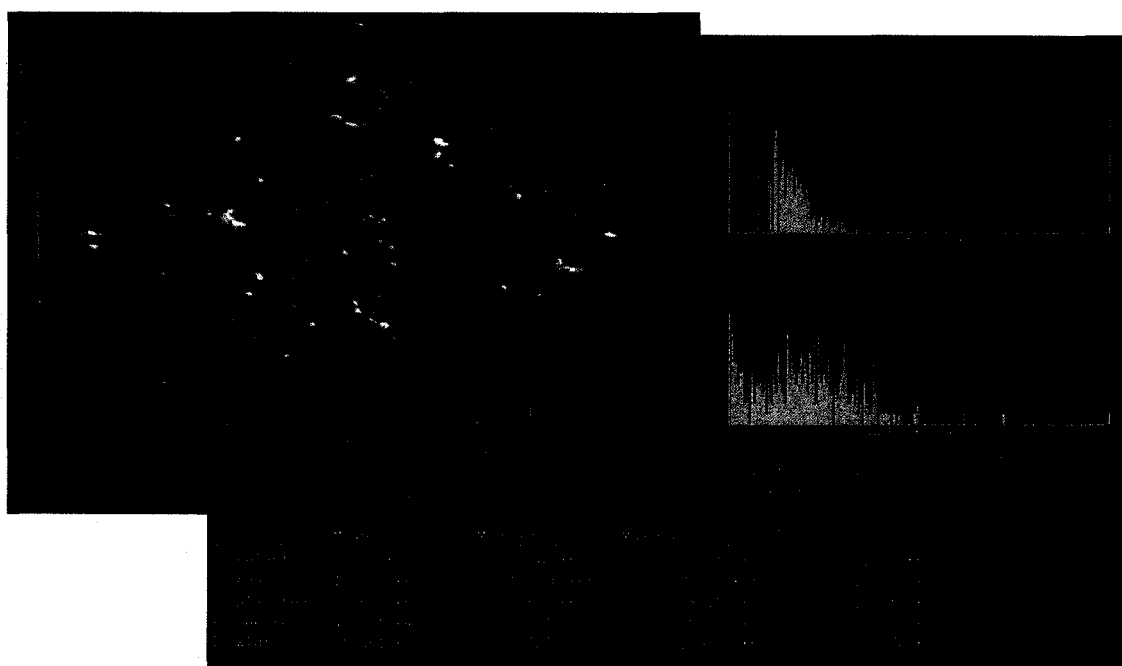


Figure B9. AFM images of  $218 \mu\text{M}$  1,8-octanediol- $\text{Au}^0$  in DMF.

The gold particles had a mean height of 4-6 nm and mean diameter of 15-30 nm. The entire composition of octanediol- $\text{Au}^0$  mixtures remained clear with increasing

intensity of pink color with increasing gold concentration. The UV absorption spectra (Figure B10), showed an absorption peak at 529 nm for concentration below 200  $\mu\text{M}$ . Above this concentration the peak shifted to 540 nm and at the highest concentration (800  $\mu\text{M}$ ) of gold sols prepared a second peak at 591 nm was observed. The absorption peak at 591 nm could be attributed to the anisotropic gold particles (peanut structure). The absorption peak at 529 nm was attributed to the surface plasmon of gold nanoparticles and the peak at 591 nm was to the anisotropic gold particle.

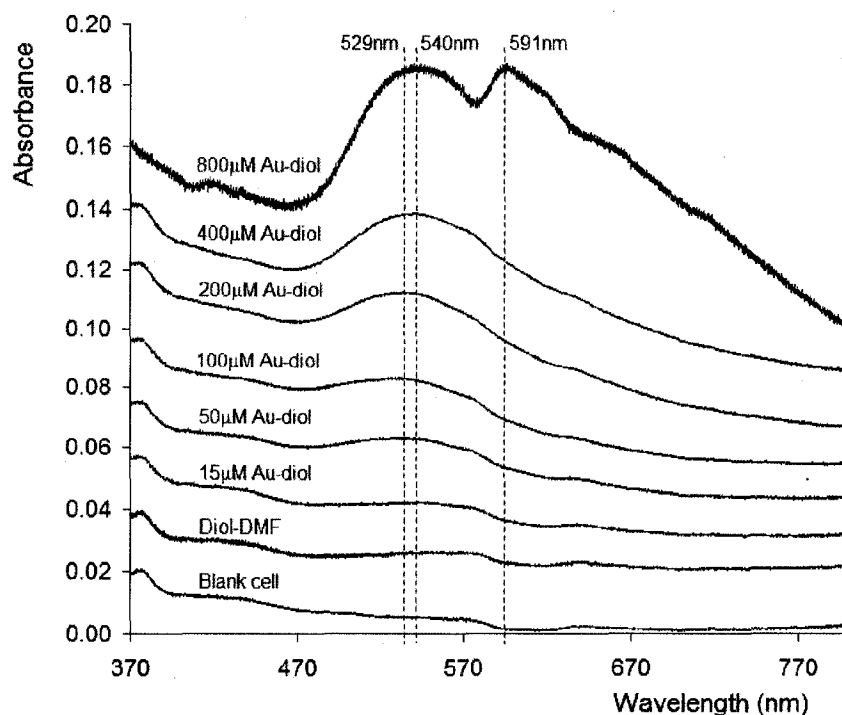


Figure B10. UV absorbance spectra of different concentration of octanediol-Au<sup>0</sup> in DMF. [Gold concentration: 800  $\mu\text{M}$ , 400  $\mu\text{M}$ , 200  $\mu\text{M}$ , 50  $\mu\text{M}$ , and 15  $\mu\text{M}$ , in 0.34 M 1,8-octanediol in DMF. The control consist of 0.34 M 1,8-octanediol in DMF].

#### B.6. Chemical reduction of iron in N,N-dimethylformamide (DMF)

Synthesis of Fe nanoparticle was performed in non-aqueous medium DMF. The results were illustrated in Figure B11. Fe nanoparticles as small as 5 nm and large as 15 nm were observed without agglomeration as illustrated in Figure B11a.

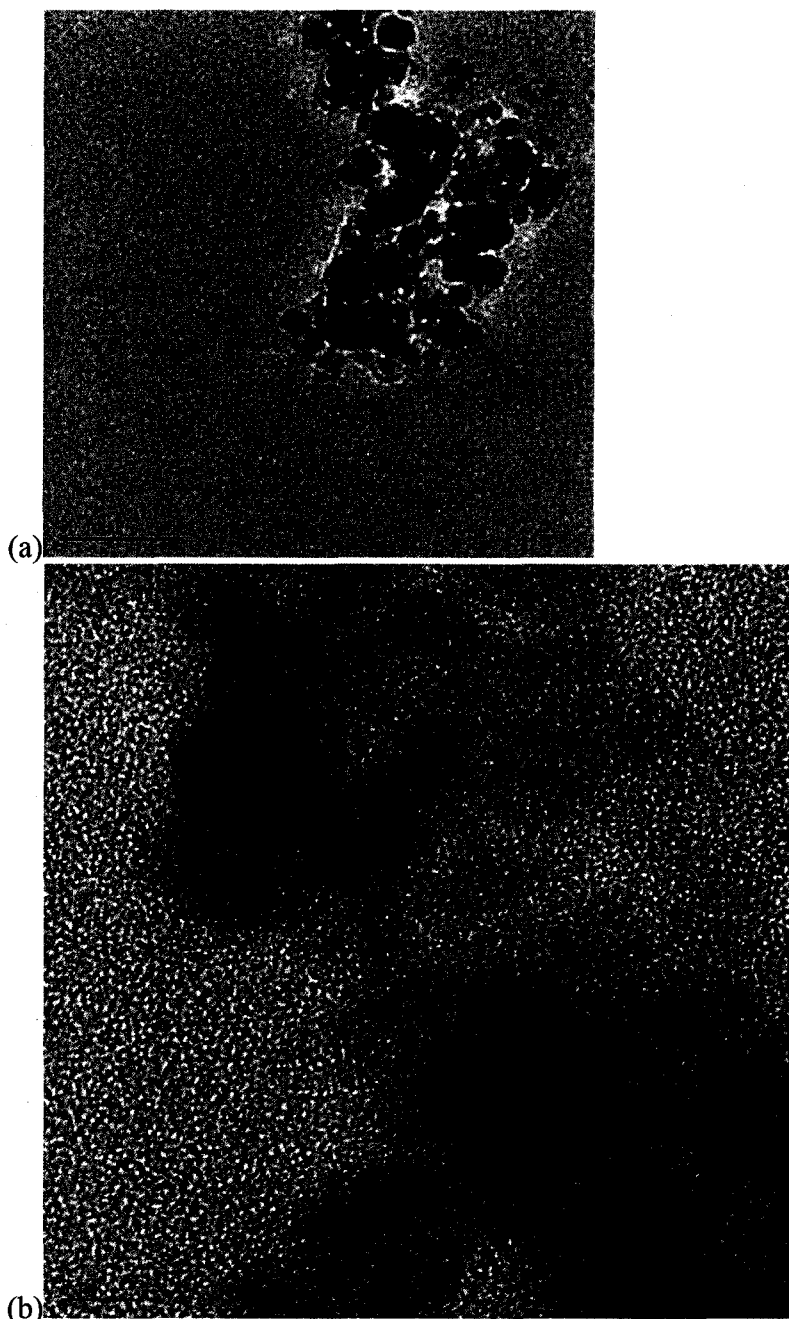


Figure B11. (a) Low and (b) high resolution TEM images of Fe nanoparticles.

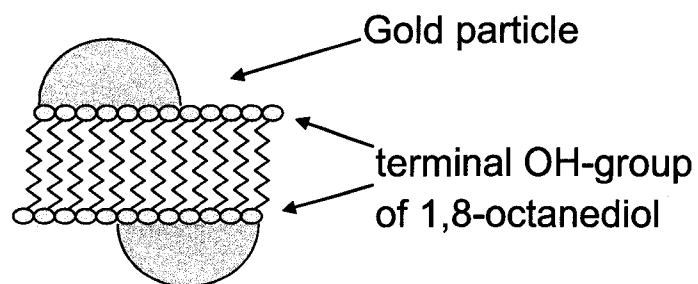


### B.6. Summary of particle size analysis

AFM Analysis					
System	Mean Height (H) (nm)	Diameter (D) (nm)	Length (L) (nm)	Width (W) (nm)	L / W
Au (700 $\mu$ M)/Water (sample 1)	13 $\pm$ 5	63 $\pm$ 21	84 $\pm$ 29	49 $\pm$ 17	1.7 $\pm$ 0.5
Au (700 $\mu$ M)/Water (sample 2)	14 $\pm$ 5	82 $\pm$ 28	118 $\pm$ 47	63 $\pm$ 20	1.9 $\pm$ 0.5
Au (DMF)	6 $\pm$ 3	32 $\pm$ 17	44 $\pm$ 26	25 $\pm$ 13	1.7 $\pm$ 0.8
	4 $\pm$ 4	15 $\pm$ 14	19 $\pm$ 16	12 $\pm$ 13	1.6 $\pm$ 1.4
Au-Fe (water) Co-ppt	8 $\pm$ 4	80 $\pm$ 45	102 $\pm$ 55	69 $\pm$ 41	1.5 $\pm$ 0.8
TEM Analysis					
Au (900 $\mu$ M)/Water (Region 1)		12 $\pm$ 2	19 $\pm$ 4	8 $\pm$ 2	2.4 $\pm$ 0.3
Au (900 $\mu$ M)/Water (Region 2)		12 $\pm$ 2	19 $\pm$ 5	8 $\pm$ 3	2.4 $\pm$ 0.5

Table B2. Particle size analysis for sample from AFM and TEM imaging.

Several conclusions were drawn from the data presented in Table B2. AFM measurements of particle length and width suffered from the tip broadening effect, but the mean height was not impacted. The latter showed larger size gold nanoparticles in aqueous medium in comparison with non-aqueous medium. TEM measurement of length and width of these nanoparticles indicated a significant shape anisotropy,  $l/w > 2$ . This effect may arise from nucleation of Au and Fe nanoparticles on disc shaped diol aggregates. Nucleation on either faces is possible leading to the observed shape anisotropy.



## **Appendix C. DSC studies of thermal properties of reactant used in SiNW synthesis**

In this studies DSC was used to investigate the phase transition as well as chemical decomposition of the three components, diol, DPS, and gold-diol/DPS mixtures.

### **Sample preparation**

A.) 1,8-octanediol (solid) was weighed using a Mettler M3 scale then placed in a aluminium pan (Mettler, with pin at base of Al pan). The pans with sample were hermetically sealed by cold welding with the crucible sealing press.

B.) 1.0  $\mu\text{L}$  of DPS was pipetted into an Al pan and sealed. A total of four samples were prepared.

C.) Diol-Au<sup>0</sup> (218  $\mu\text{M}$  in DMF, as prepared in the previous section) was pipetted into the Al pan followed by heating to evaporate off the DMF. DPS was then pipetted on to the Diol-Au<sup>0</sup>. The ratio of Diol-Au<sup>0</sup> solution to DPS added was 1:3 (Diol-Au<sup>0</sup>:DPS w/w). The Al pan was sealed with a press. A total of four samples were prepared.

A reference pan was prepared by sealing an empty Al pan.

### **DSC experiments**

DSC was setup to heat the 1,8-octanediol samples from 40-370 °C and the heat exchange during phase change or reaction was measured with respect to the reference. For the DPS samples, the DSC was setup to heat from 90-450 °C. A cooling run was performed on one DPS sample from 450-90 °C immediately after the heating run.

Finally, the Diol-Au<sup>0</sup>/DPS samples were heated from 40-450 °C, and one sample was cooled from 420-40 °C immediately after the heating run.

## Results

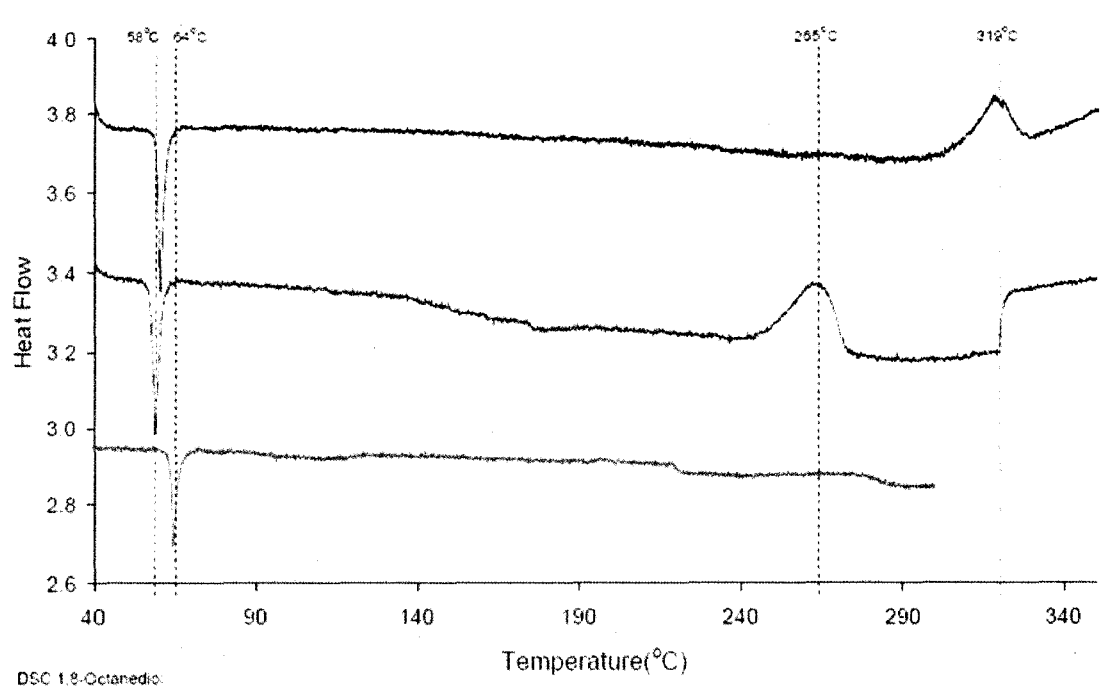


Figure C1. DSC thermogram of 1,8-octanediol

1,8-octanediol has melting point of ~60-62 °C which was observed as an exothermic peak between 58-64 °C (Figure C1). An endothermic peak was observed further at 265-319 °C most probably due to boiling of diol. The range in the 2<sup>nd</sup> peaks can be attributed to different in the gaseous pressure within the Al pan.

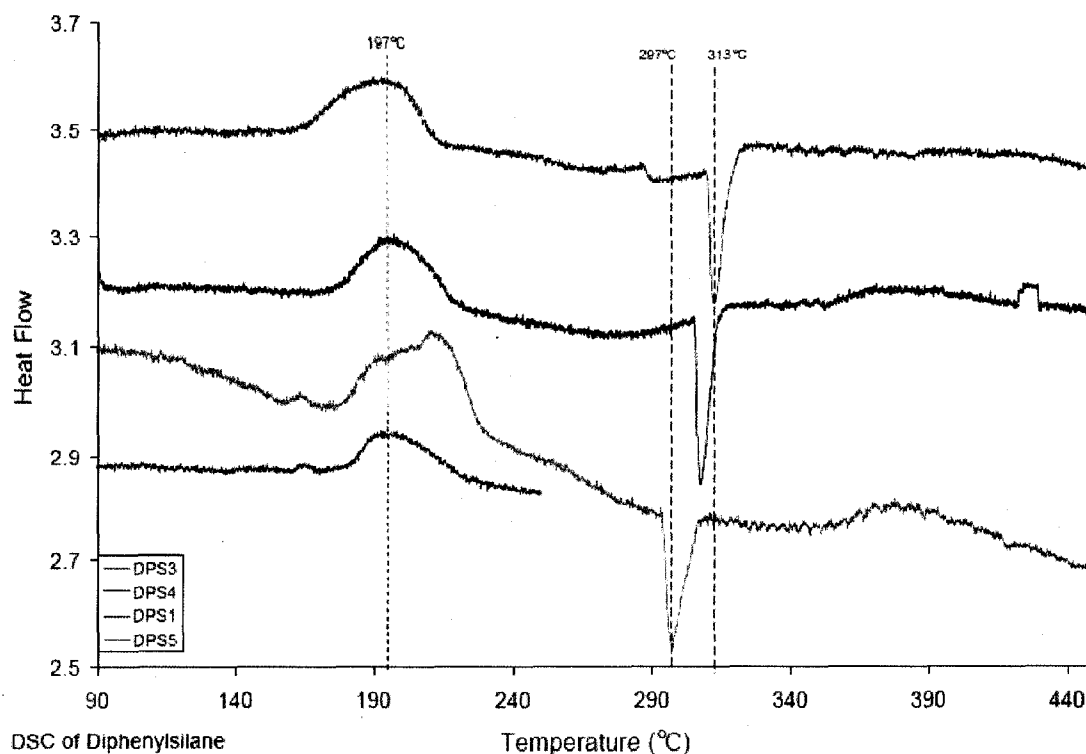


Figure C2. DSC thermogram of diphenylsilane

DPS showed two transition peaks, an endothermic peak at  $\sim 197^{\circ}\text{C}$  and an exothermic peak at  $\sim 300^{\circ}\text{C}$  observed from the thermograph in Figure C2. The peak at  $197^{\circ}\text{C}$  might be due to the boiling of DPS at atmospheric pressure (which has a boiling point at  $95\text{--}97^{\circ}\text{C}$  at  $13\text{ mmHg}$  according to literature) and that at  $300^{\circ}\text{C}$  due to decomposition of DPS. This was verified by the cooling run. Results were illustrated in Figure C3.

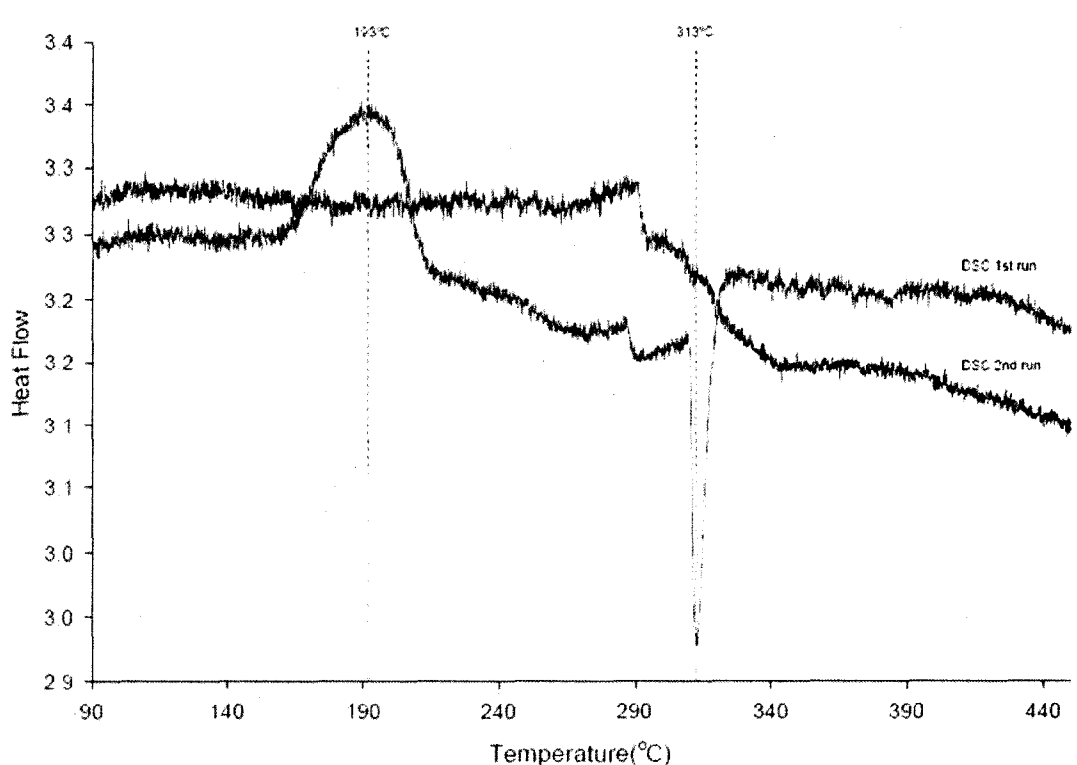


Figure C3. DSC thermograms for heating (1<sup>st</sup> run) and consecutive cooling (2<sup>nd</sup> run) of DPS.

In the cooling run, no reproducible peaks were observed at 197 °C and 300 °C. This suggests that DPS has irreversibly decomposed to SiO<sub>x</sub> around 313 °C.

The DSC thermographs for diol-Au<sup>0</sup>/DPS samples were more complex due to multicomponents that were non-reactive with one another. The only distinctive peaks were observed between 277-311 °C. However, there was a smaller peak exist between 370-393 °C. This might be due to the eutectic point of Au-Si alloy.

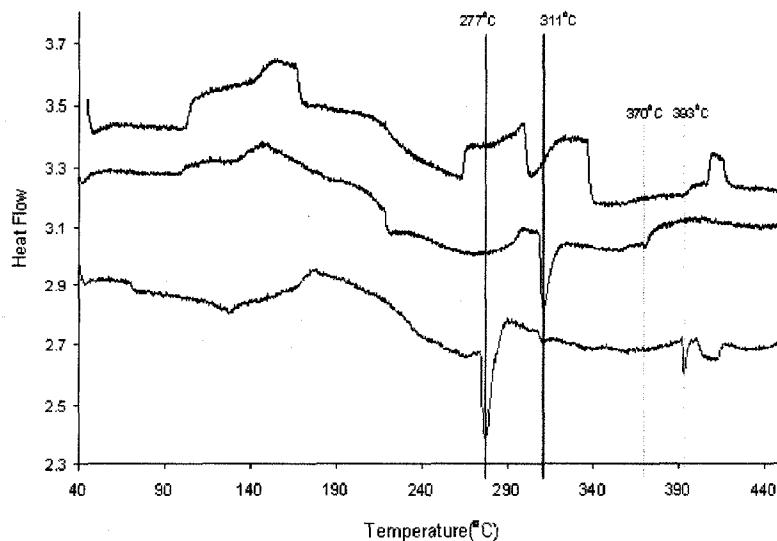


Figure C4. DSC thermogram of diol-Au<sup>0</sup>/DPS mixtures, heating runs.

In the cooling run (Figure C4), the peaks at 277 °C disappeared perhaps due to crystallization of Si from gold-silicon alloy. SiNWs could be formed at temperature greater than 393 °C thus no Au-Si alloy peak at 393 °C was observed.

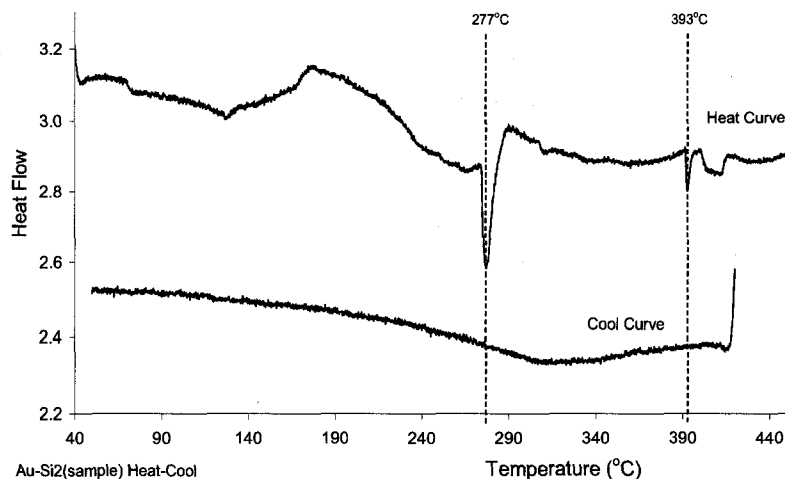


Figure C5. DSC heating (1<sup>st</sup> run) and consecutive cooling (2<sup>nd</sup> run) of diol-Au<sup>0</sup>/DPS.

From the DSC experiments, it seemed that the minimum temperature required for SiNW synthesis should be above 400 °C.

## Appendix D. Construction of supercritical flow reactor system

The titanium reactor (Part no. 211343) was purchased from High Pressure Equipment Company, HiP (Erie, PA) [engineer design illustrated below]. The titanium reactor body was 3.69 inches in length, with O.D 1.63 inches and I.D. 0.44 inches. It has a nominal capacity of 5mL. The two ends of the reactor body were fitted with two sets of titanium adaptors (adaptor 1: HiP part no. 15-21AF2LM9-Ti5, Male 9/16" Medium pressure (LM9) to 1/8" female taper seal (AF2) adaptor; and adaptor 2: HiP part no. 15-21HF2AM2-Ti5, Male 1/8" taper seal (AM2) to 1/8" female (HF2) High pressure adapter) to reduced the outlet from 9/16" to 1/8" (Figure D1).

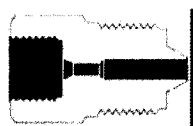


Figure D1. 15-21AF2LM9-Ti5 and 15-21HF2AM2-Ti5 adaptor.

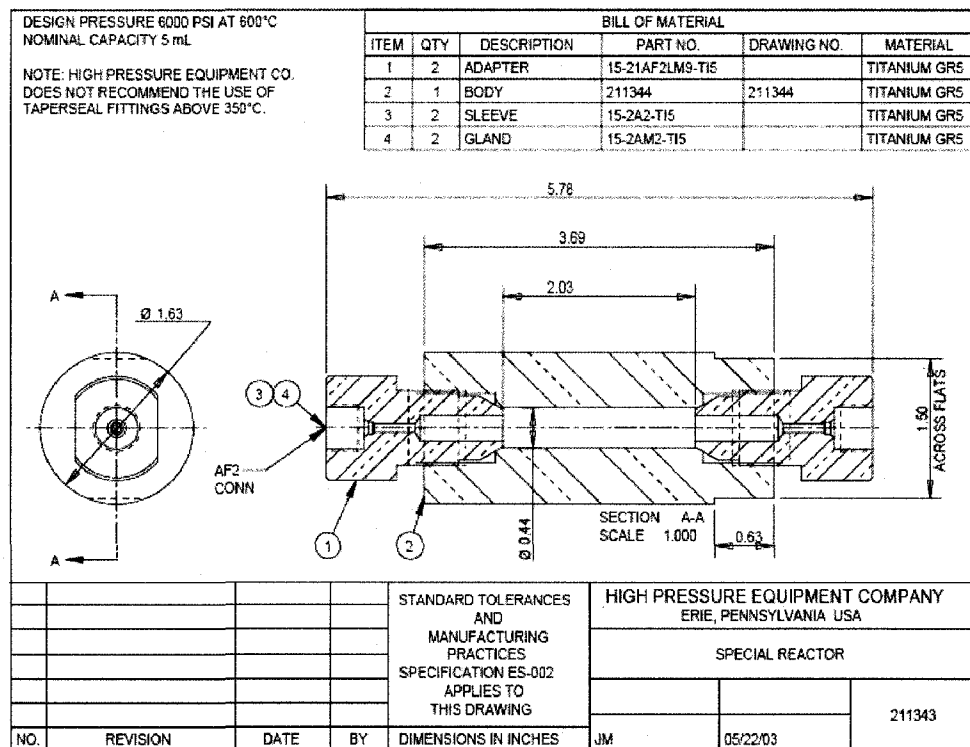


Figure D2. Engineer design of the titanium reactor.



The outlet of the two ends of the titanium adaptors was piped with a 316 stainless steel 6" long high pressure coned and threaded nipple tubing (Figure D3; HiP part no. 30-HM2-6; rated for 30,000 psi, O.D. 1/8", I.D. 0.040").

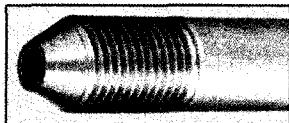


Figure D3. HiP Coned and threaded nipple tubing.

Finally, the end of the nipple was attached to a 316 stainless coupling (HiP part no. 15-21AF1HF2, female 1/8" high pressure (HF2) to female 1/16" taper seal (AF1), 15,000 psi rating; length 1 1/8") to reduce the outlet from 1/8" to 1/16" (O.D.).



Figure D4. HiP Female to female coupling (reducer for 1/8" to 1/16" O.D.)

The entire system was connected using 1/16" 316 stainless tubing (HiP part no. 15-9A1-030; 1/16" O.D. and 0.030" I.D.). The junctions and flow was managed by taper seal tees (HiP part no. 15-23AF1, 1/16" O.D. 316s.s, pressure rating 15,000 psi), taper seal crosses (HiP part no. 15-24AF1, 1/16" O.D. 316s.s, pressure rating 15,000 psi) manifold and two way straight valves (HiP part no. 15-11AF1, 1/16" O.D. 316s.s, pressure rating 15,000 psi) purchased from HiP. The pressure in the reactor was monitored by a digital pressure gauge (Omega, part no. DPG5000L-5KG-Z-PK, pressure range from 0 to 5000psi, equipped with zero knob and peak hold function, 0-2 V dc analog output) at the outlet end of the Ti reactor. The Ti reactor was heated with an ultra-high temperature heating tape (Omega, part no. STH051-020,

temperature up to 760 °C, size ½" x 2', 13 Watt/in<sup>2</sup> (total wattage of 156), 120 V, 1.3 A), with integrally molded separable plug on both ends of the tape. The heating tape temperature was controlled and monitored with a 1/16 DIN MICROMEGA® autotune PID temperature/process controller (Omega, part no. CN77343, NEMA-12 face for 1/16 DIN cutout and bezel, pulse 10 V dc and 5 A relay; unit equipped with RS-232) and a k-type thermocouple (Omega, part no. TJC36-CASS-062G-12-SMPW-M; CHROMEGA® ALOMEGA 304 SS sheath; grounded; 12 inches, with a miniature connector installed). The internal pressure of the system was pressured by pumping cyclohexane via a solvent delivery HPLC pump (Beckman, module 110 A). The pressure was regulated by a pressure relief valves (Swagelok, part no. SS-4R3A) with spring kit (Swagelok, part no. 177-R3A-K1-F, set pressure range from 205 to 275 bar) installed and adjusted to relief at 3000 psi, at the outlet end of the reactor. Gold and silicon precursor were delivery into the system by injecting through a manual sample injector (Rheodyne, model 7725i) with a 200 µL sample loop (Rheodyne, part no. 7755-025, stainless steel).

## Appendix E. Calibration of furnaces

### E.1. Calibration of Lindberg furnace

The core temperature of the copper pipe was calibrated by inserting a k-type thermocouple into the center of the  $\frac{3}{4}$  inch copper tubing in the Lindberg furnace. The thermocouple was connected to the digital multimeter (Mastach® MAS-345) with a RS-232 port. The RS-232 was connected to the pc with MasView software installed for recording the temperature with respect to time. Calibration was performed by setting the temperature on the front digital control to 150 °C first then monitoring the stabilization temperature of the core. The front digital control temperature setting was adjusted to different set points and the stabilization was monitored. The set points were 200 °C, 300 °C, 350 °C, 375 °C, 400 °C, 425 °C and 450 °C. The calibration plot is illustrated in Figure E1.

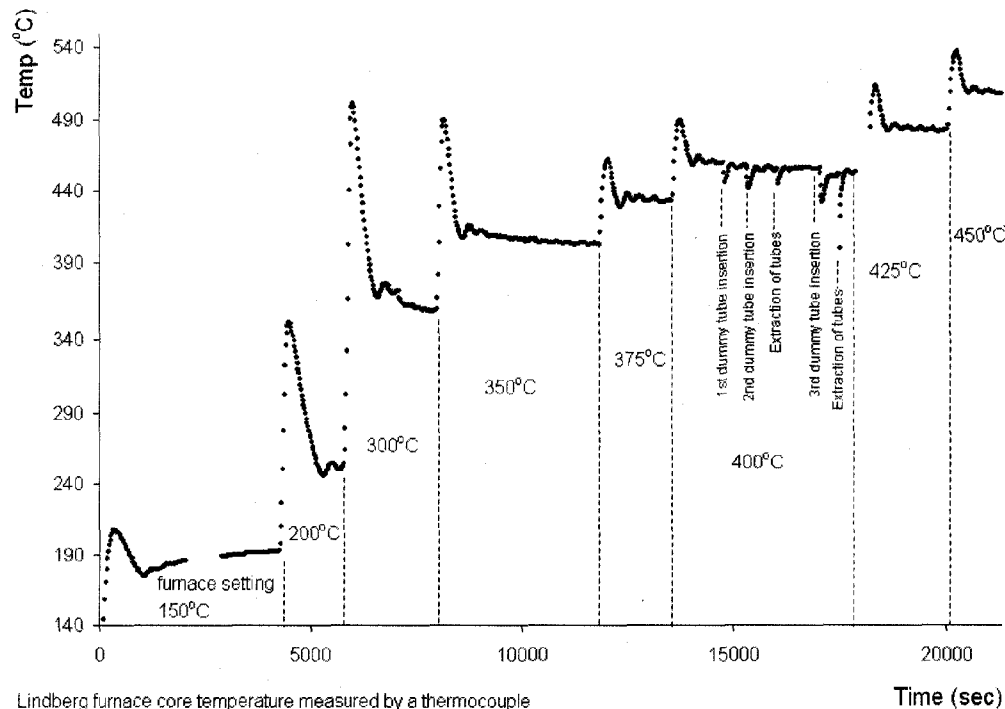


Figure E1. Calibration plot of Lindberg furnace

From the calibration plot, the temperature stabilizes at 460 °C at the Lindberg furnace control setting of 400 °C. Once the furnace stabilized at 460 °C three dummie tubes were inserted at different times and the average drop in temperature and time to recover after the drop was recorded. An 18 inch long by ½ inch diameter copper tubing was used to extract the dummie tubes by inserting into the ¾ inch diameter copper tubing in the furnace. The dummy tube gently slid into the ½ inch copper tubing thus extracting it from the furnace with ease. The average temperature drops by 16 °C and average time to recovers was 140 seconds.

## **E.2. Calibration of glass furnace**

A 1.9 cm ID x 31 cm long glass tube was heated by coiling with an ultra-high temperature heating tape [Omega, part no. STH051-020, temperature up to 760 °C, size ½" x 2', 13 Watt/in<sup>2</sup> (total wattage of 156), 120 V, 1.3 A], with integrally molded separable plug on both ends of the tape. The heating tape temperature was controlled and monitored with a 1/16 DIN MICROMEGA® autotune PID temperature/process controller (Omega, part no. CN77343, NEMA-12 face for 1/16 DIN cutout and bezel, pulse 10 V dc and 5 A relay; unit equipped with RS-232) and a k-type thermocouple (Omega, part no. TJC36-CASS-062G-12-SMPW-M; CHROMEGA® ALOMEGA 304 SS sheath; grounded; 12 inches, with a miniature connector installed). The glass furnace was calibrated first with respect to the furnace core temperature versus the controller temperature, and second to the time required for the glass tube to reach a desire reaction temperature.

A 1 cm OD x 13 cm long glass tube was inserted into the glass furnace, with the close-end head in first, to the center position of the heating tape coil. A second k-type thermocouple was inserted into the glass tube monitoring the internal tube temperature via a digital multimeter (MASTECH, MAS-345). The glass tube core temperature versus the heating tape controller temperature was monitored simultaneously.

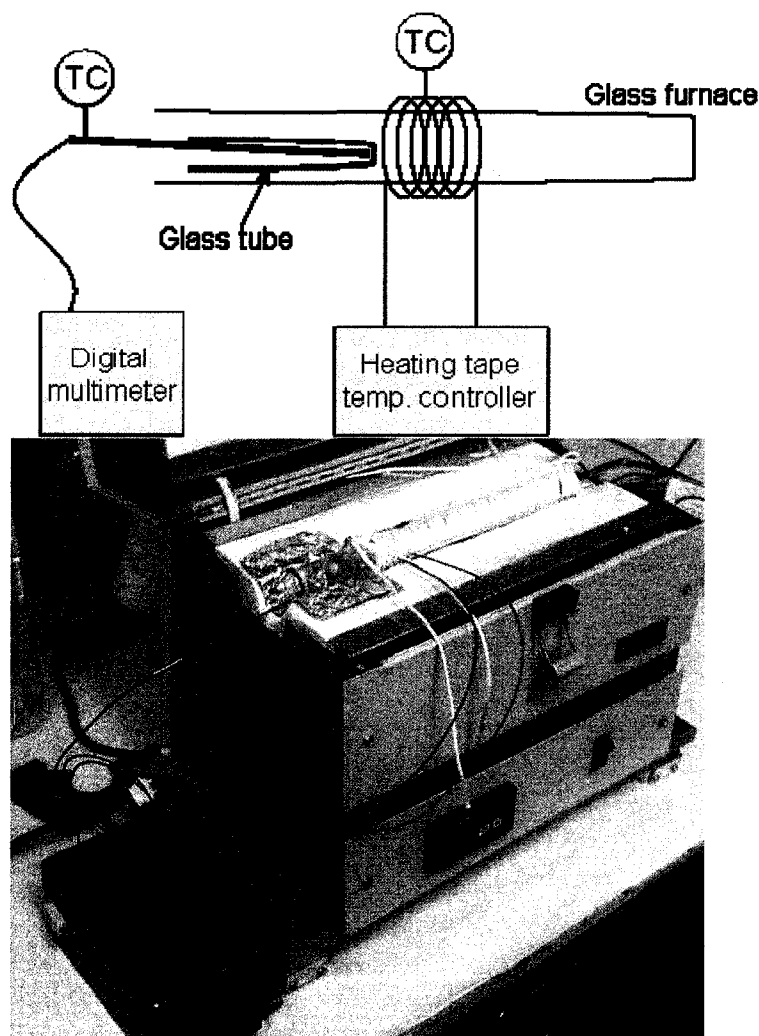


Figure E2. Glass furnace setup and calibration

For the second calibration, the glass furnace was preheated to 500 °C. Once the furnace temperature stabilizes a glass tube, with the thermocouple inserted, was inserted into the furnace to the center position of the heating coil. The time for the glass tube to reach 500 °C was monitored.

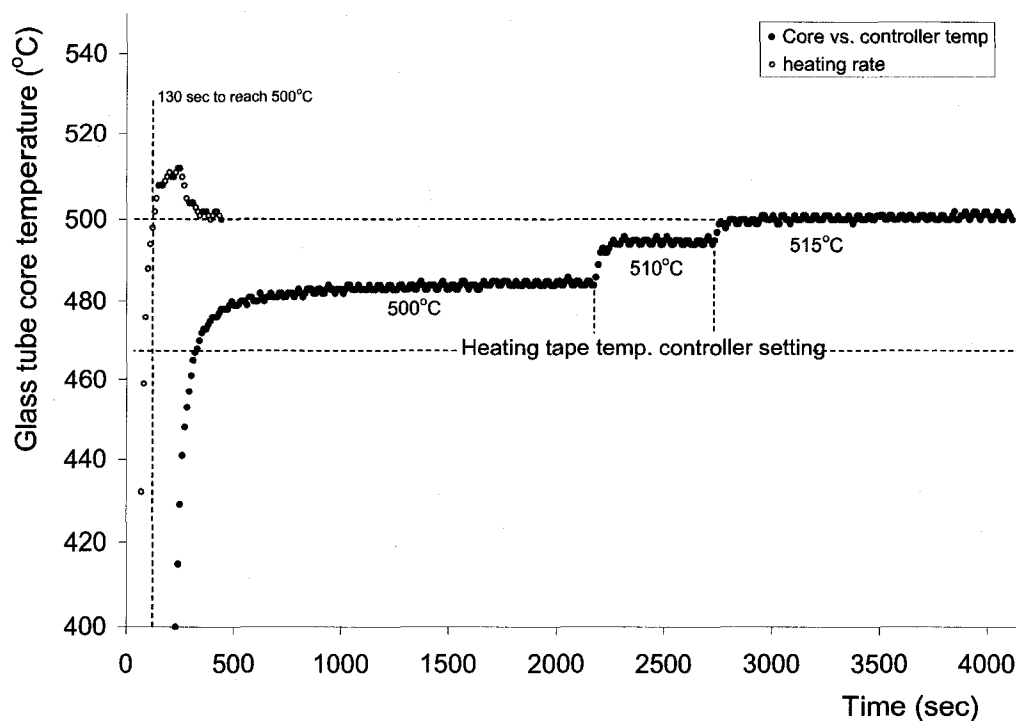


Figure E3. Calibration of glass furnace: a.) solid dots - glass tube core temperature versus the heating tape controller temperature; and b.) hollow dots - heating rate calibration.

The glass tube core temperature lags by -15 °C of the glass furnace temperature. Furthermore, it takes 130 sec for a glass tube to reach a temperature of 500 °C.

## Appendix F. TEM HR lattice plane imaging, selected area diffraction pattern and lattice plane analysis

### F1. Determination of growth direction of SiNW from HRTEM lattice imaging

In many crystals, multiple lattice planes can exist due to the orientation of the atoms in the unit cell. Si has a simple cubic unit cell. High resolution TEM images that have been obtained usually show lattice fringes as a result of diffraction from a one lattice plane of a single crystalline SiNW. To determine the Miller index of the lattice plane the  $d$ -spacing between the parallel planes is measured. The  $d$ -spacing is given as<sup>98</sup>,

$$d = \frac{a}{\sqrt{(h^2 + k^2 + l^2)}}$$

Where  $a$  is the lattice constant (5.43 Å for Si). The corresponding Miller indices with its  $d$ -spacing is calculated and tabulated in Table F1.

---

<sup>98</sup> Jenkins, R. and Snyder, R. L. Introduction to X-ray Powder Diffractometry, John Wiley & Son, Inc. New York, 1996, Volume 138

$h$	$k$	$l$	$d$ (Å)
1	0	0	5.43
1	1	0	3.84
1	1	1	3.14
1	1	3	1.64
2	0	0	2.72
2	1	0	2.43
2	1	1	2.22
2	2	0	1.92
2	2	2	1.57
3	0	0	1.81
3	1	0	1.72
3	1	1	1.64
3	1	2	1.45
3	2	0	1.51
3	3	0	1.28
3	3	1	1.25
3	3	2	1.16
3	3	3	1.05
4	0	0	1.36
2	2	4	1.11

Table F1. Corresponding Miller indices with its  $d$ -spacing for silicon. (highlight are the most commonly observed planes for Si)

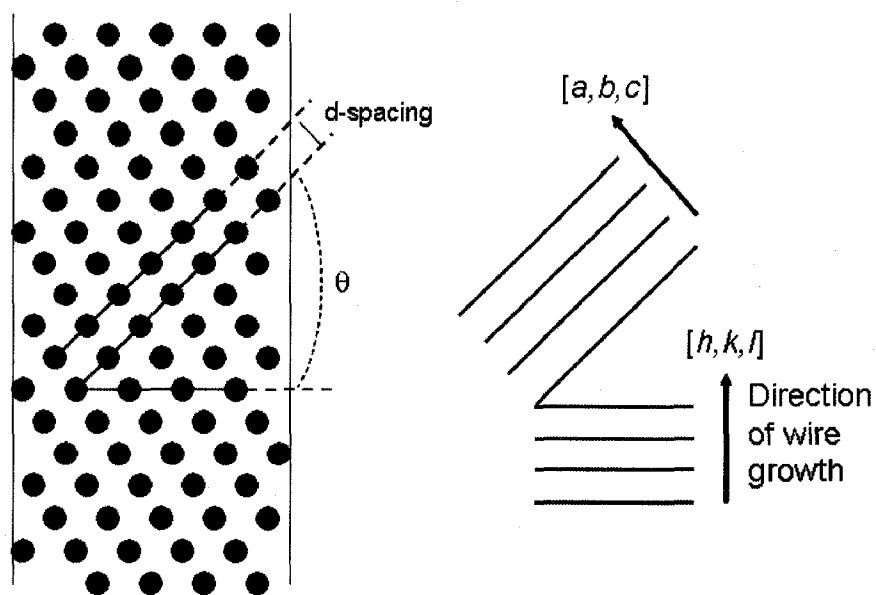


Figure F1. Pictorial representation of multiple lattice planes in a single crystal.



A majority of the time the lattice plane in the direction of wire growth is not prominent or observed under TEM. To determine the lattice plane in the direction of growth, the angle between the planes, i.e. the adjacent angle between the observed plane and plane normal to the sidewall of the SiNW, is calculated (refer to Figure F1).

$\begin{matrix} a,b,c \\ h,k,l \end{matrix}$	100	010	001	110	011	101	111	112	113	210	310	311	312	320	331	332
100	0	90	90	45	90	45	55	66	73	27	18	25	37	34	47	50
010	90	0	90	45	45	90	55	66	73	63	72	73	75	56	47	50
001	90	90	0	90	45	45	55	35	25	90	90	73	58	90	77	65
110	45	45	90	0	60	60	35	55	65	18	27	32	41	11	13	25
011	90	45	45	60	0	60	35	30	32	72	77	65	56	67	50	41
101	45	90	45	60	60	0	35	30	32	51	48	32	19	54	50	41
111	55	55	55	35	35	35	0	20	30	39	43	30	22	37	22	10
112	66	66	35	55	30	30	20	0	10	57	59	42	29	56	42	30
113	73	73	25	65	32	32	30	10	0	66	68	51	36	65	52	40
210	27	63	90	18	72	51	39	57	66	0	8	19	33	7	23	31
310	18	72	90	27	77	48	43	59	68	8	0	18	32	15	30	36
311	25	73	72	31	65	32	30	42	51	19	18	0	15	23	26	26
312	37	75	58	41	56	19	22	29	36	33	32	15	0	35	31	24
320	34	56	90	11	67	54	37	56	65	7	15	23	35	0	17	28
331	47	47	77	13	50	50	22	42	52	23	30	26	31	17	0	12
332	50	50	65	25	41	41	10	30	40	31	36	26	24	28	12	0

Table F2. Angles between planes<sup>99</sup>

By matching the angle between the planes with one known plane [a,b,c] the other plane could be identified (Table F2). The validity of this method was supported by the HRTEM image of SiNW catalyzed by Al result in Figure 40 of Chapter 3. In that case, the individual atoms in the lattice were well resolved that both adjacent lattice planes could be identified by determining the *d*-spacing in both directions. The measured

<sup>99</sup> Free “Angle Between Planes” calculator from Brigham Young University, Department of Electrical and Computer Engineering website ([http://www.ee.byu.edu/cleanroom/EW\\_orientation.phtml](http://www.ee.byu.edu/cleanroom/EW_orientation.phtml)), accessed on 06/11/2008

angle between the planes  $[1,0,0]$  and the  $[1,1,1]$  growth direction was  $55^\circ$ , as predicted from calculated Table F2.

## **F2. High resolution TEM images**

The following are HRTEM images of undoped SiNWs synthesized directly on from Copper TEM grid. Perfectly intact cross-junctions of SiNWs are observed throughout the grid by direct synthesis on the TEM grid. Direct synthesis of SiNWs on the TEM grid minimizes the chance of physical damage by scraping during sample preparation. Each figure caption illustrates different SiNWs on the sample.

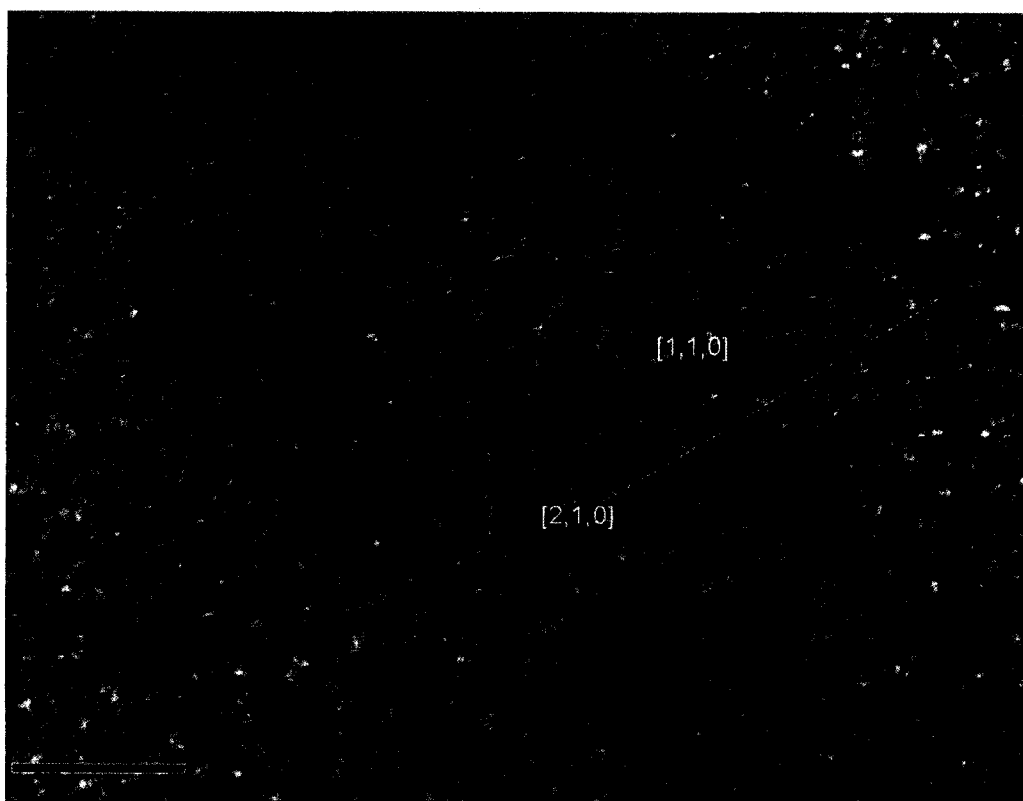


Figure F2. HRTEM of undoped SiNW

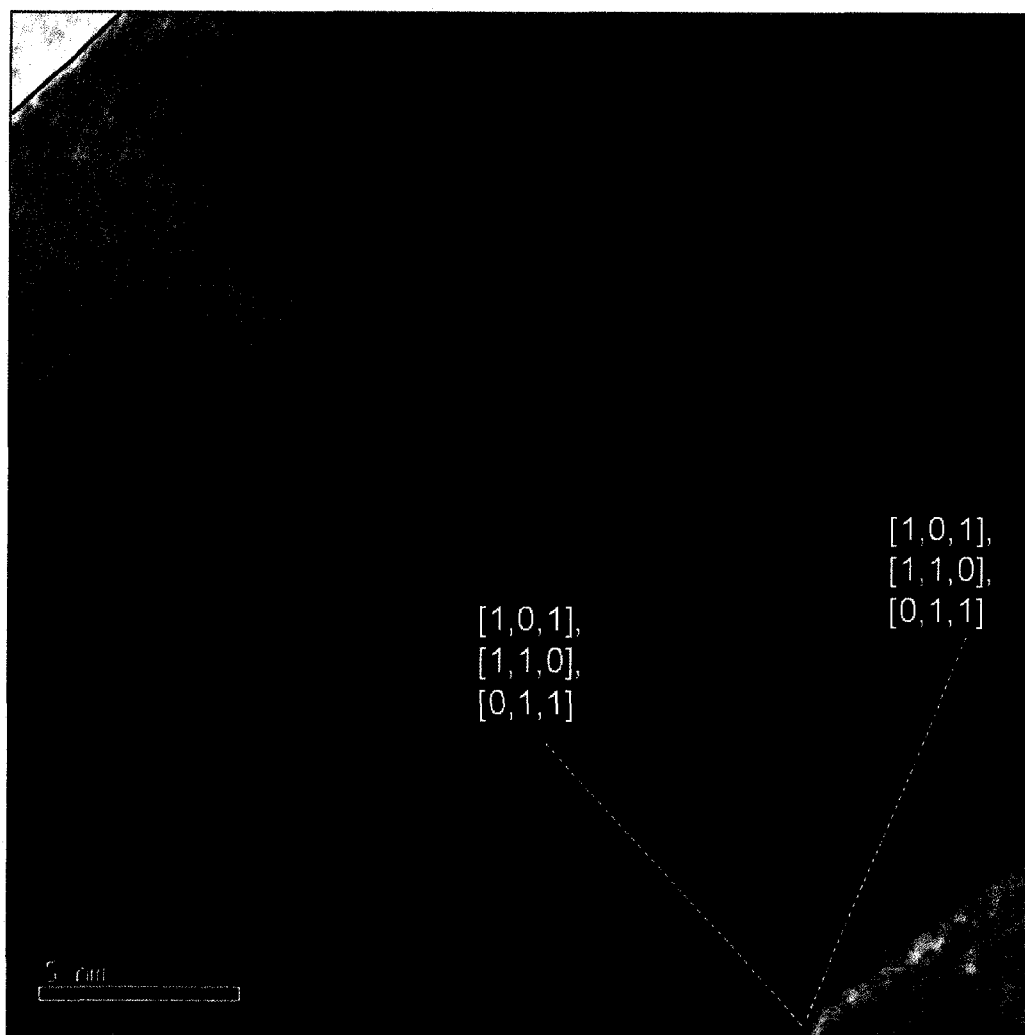


Figure F3. HRTEM of undoped SiNW

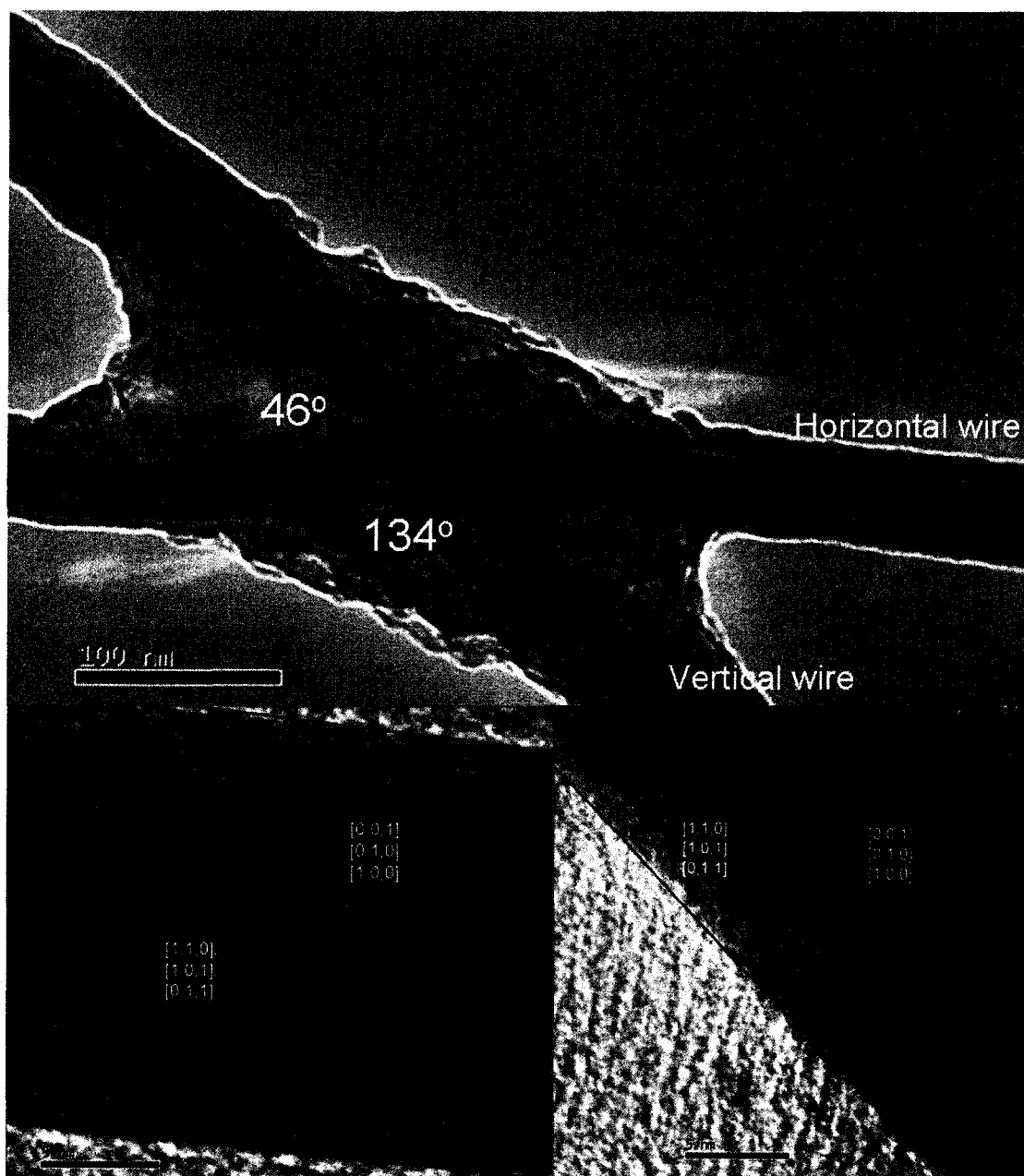


Figure F4. HRTEM of undoped SiNW. [Top: SiNW junction; Bottom left: HR of horizontal SiNW; Bottom right: HR of vertical SiNW]

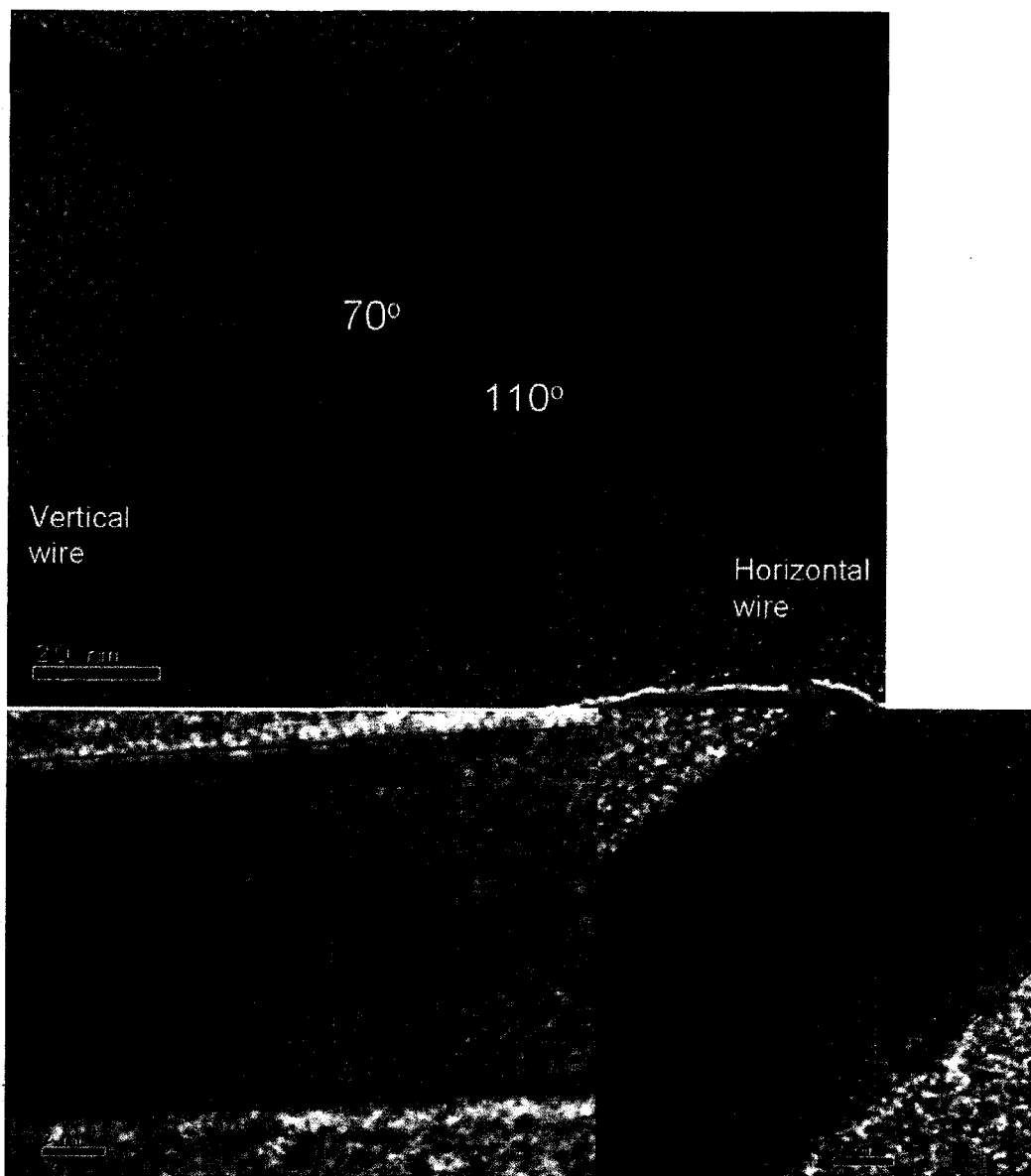


Figure F5. HRTEM of undoped SiNW. [Top: SiNW junction; Bottom left: HR of horizontal SiNW; Bottom right: HR of vertical SiNW]

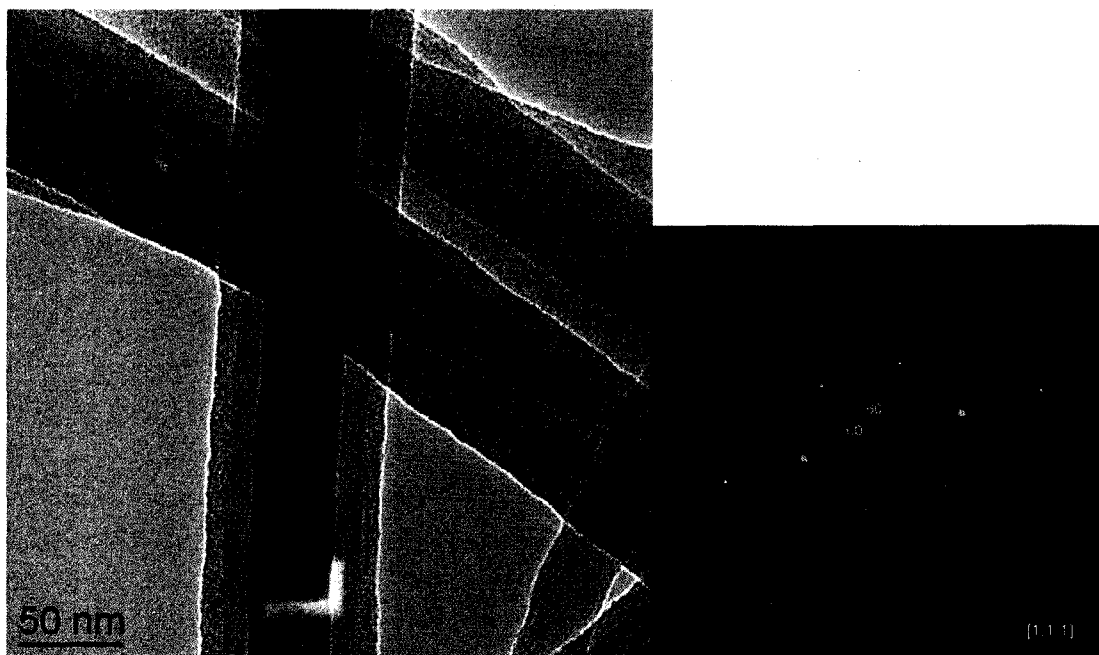


Figure F6. TEM image of SiWN (left) with corresponding diffraction pattern.

**Appendix G. Fluorescence spectroscopy of undoped SiNW, doped SiNW and Si sphere**

Undoped SiNWs		
Excitation wavelength		
250 nm	271 nm	300 nm
Emission energy (eV)		
3.5	3.4	3.0
3.5	3.4	3.0
3.5	3.4	3.0
3.5	3.4	2.9
3.2	3.1	2.7
3.1	3.5	2.9
3.0	3.4	
3.5	3.4	
3.2	3.4	
3.1		
3.5		
3.0		
3.6		
3.6		
Average		
3.35±0.22	3.37±0.10	2.92±0.14

Table G1. Average fluorescence data for undoped SiNWs

Doped SiNW		
Excitation wavelength		
250 nm	271 nm	300 nm
Emission energy (eV)		
2.9	2.9	2.8
3.1	3.0	2.7
3.1	3.0	2.8
3.0	2.8	2.8
3.0	3.0	
3.0	3.0	
3.1	3.0	
3.0	3.0	
3.0	2.9	
3.0	3.0	
Average		
3.04±0.10	2.95±0.10	2.77±0.10

Table G2. Average fluorescence data for doped SiNWs

Si spheres		
Excitation wavelength		
250 nm	271 nm	300 nm
Emission energy (eV)		
2.9	2.8	2.5
2.8	2.8	2.6
2.8	2.8	2.6
		2.7
Average		
2.84±0.10	2.79±0.10	2.61±0.10

Table G3. Average fluorescence data for Si spheres.



No.	Samples	Mole DPS ( $\mu\text{mol}$ )	Internal pressure (atm)	Reaction temp. ( $^{\circ}\text{C}$ )	Reaction time (min)	SiNW diameter (nm)	Excitation $\lambda$ (nm)	Emission $\lambda$ (nm)	Energy (eV)
1	SiNW on Si	8	0.07	450	25	127 $\pm$ 38	250 271 300	350 364 414	3.5 3.4 3.0
2	SiNW on Si	16	0.15	450	25	41 $\pm$ 8	250 271 300	350 364 408	3.5 3.4 3.0
3	SiNW on Si	--		450	7	--	250 271 300	358 364 408	3.5 3.4 3.0
4	SiNW on Si	8	0.09	600	25	312 $\pm$ 37	250 271 300	354 364 428	3.5 3.4 2.9
5	SiNW on Si	38	0.37	500	60	--	250 271 300	386 400 428	3.2 3.1 2.9
6	SiNW on Si	8	0.08	500	35	23 $\pm$ 6	250	396	3.1
7	SiNW on Si	sprayed	--	500	25	34 $\pm$ 12	250	410	3.0
8	SiNW on Si	--	--	--	--	--	300	462	2.7
9	SiNW on Si	--	--	--	--	--	250 271	352 358	3.5 3.5
10	SiNW on Si	108	0.37	450	30	47 $\pm$ 7	250 300	388 452	3.2 2.7
		108	0.37	450	20	25 $\pm$ 3	250	400	3.1
11	SiNW on Al	27	0.09	450	7	--	250 271 300 350	358 366 430 482	3.5 3.4 2.9 2.6
12	SiNW on Al	43	0.15	500	70	36 $\pm$ 7	250 271	408 366 406 434	3.0 3.4 3.1 2.9
13	SiNW on Al	81	0.74	450	25	67 $\pm$ 23	250 271	348 366	3.6 3.4

Table G4. Compiled fluorescence data for undoped SiNWs.